Spring 1-1-2012

Multiple Exciton Generation in Quantum Dot Solar Cells

Octavi Escala Semonin
University of Colorado at Boulder, octavi@gmail.com

Multiple Exciton Generation in Quantum Dot Solar Cells

by

O. E. Semonin

B.A., Harvey Mudd College, 2006

M.S., University of Colorado, 2011

A thesis submitted to the

Faculty of the Graduate School of the

University of Colorado in partial fulfillment

of the requirements for the degree of

Doctor of Philosophy

Department of Physics

2012

This thesis entitled:
Multiple Exciton Generation in Quantum Dot Solar Cells
written by O. E. Semonin
has been approved for the Department of Physics

_____

Prof. Arthur J. Nozik

_____

Prof. Daniel S. Dessau

Date _____

The final copy of this thesis has been examined by the signatories, and we find that both the content and the form meet acceptable presentation standards of scholarly work in the above mentioned discipline.

Semonin, O. E. (Ph.D., Physics)

Multiple Exciton Generation in Quantum Dot Solar Cells

Thesis directed by Prof. Arthur J. Nozik

Photovoltaics are limited in their power conversion efficiency (PCE) by very rapid relaxation of energetic carriers to the band edge. Therefore, photons from the visible and ultraviolet parts of the spectrum typically are not efficiently converted into electrical energy. One approach that can address this is multiple exciton generation (MEG), where a single photon of sufficient energy can generate multiple excited electron-hole pairs. This process has been shown to be more efficient in quantum dots than bulk semiconductors, but it has never been demonstrated in the photocurrent of a solar cell.

In order to demonstrate that multiple exciton generation can address fundamental limits for conventional photovoltaics, I have developed prototype devices from colloidal PbS and PbSe quantum dot inks. I have characterized both the colloidal suspensions and films of quantum dots with the goal of understanding what properties determine the efficiency of the solar cell and of the MEG process. I have found surface chemistry effects on solar cells, photoluminescence, and MEG, and I have found some chemical treatments that lead to solar cells showing MEG. These devices show external quantum efficiency (EQE) greater than 100% for certain parts of the solar spectrum, and I extract internal quantum efficiency (IQE) consistent with previous measurements of colloidal suspensions of quantum dots.

These findings are a small first step toward breaking the single junction Shockley-Queisser limit of present-day first and second generation solar cells, thus moving photovoltaic cells toward a new regime of efficiency.

Dedication

To Dr. Mom and Dr. Dad.

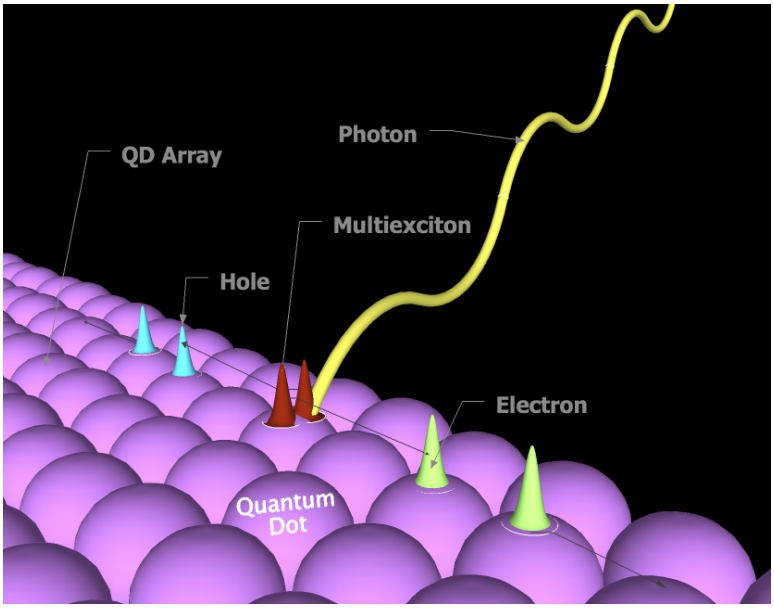

Figure 1: An "MEG" in the wild.

Acknowledgements

Thanks to my classmates who got me through grad school, to my labmates who got me through long days in lab, to my advisors who go me through both the good and the bad ideas, and to Bill Glover for not kicking me out of NREL.

Contents

Chapter

Tables

Table

Figures

Figure

Chapter 1

Introduction

Solar energy is widely considered an integral part of any renewable, non-CO_2 emitting energy portfolio. No other energy source can match it's scale (170,000 TW) or access (everywhere there is sunlight). For comparison, global human consumption[1] of energy is estimated to be approaching 20 TW now, reaching 30 TW in the next couple decades [58]. Even in northern European nations, at a latitude of 55°, the annually-averaged insolation is 100 MW/km^2, accounting for the seasons, rotation of the earth, and cloud cover. Usefully, developing countries tend to have a significantly larger solar resource (as high as 300 MW/km^2, annually averaged) because they are more often located between the Tropics of Cancer and Capricorn [101].

The problem, of course, is that solar energy is a low density medium, and the photovoltaics used to convert this energy have not been very efficient ($\eta < 20\%$) and relatively expensive ($C \sim \$500/\text{m}^2$). The figure of merit for assessing the economic competitiveness of solar cells has traditionally been the cost/peak power output:

$$\$/W_P = \frac{C}{\eta P_{sun}}, \tag{1.1}$$

where $P_{sun} = 1000$ W/m^2 is the solar insolation for a clear day on the Earth's mid-latitudes. This relation suggests a natural tradeoff between efficiency and the cost of making the solar cell, which is the basis behind Fig. 1.1.

[1] Consumption in the form of food is not included here, but is likely on the order of 1 TW.

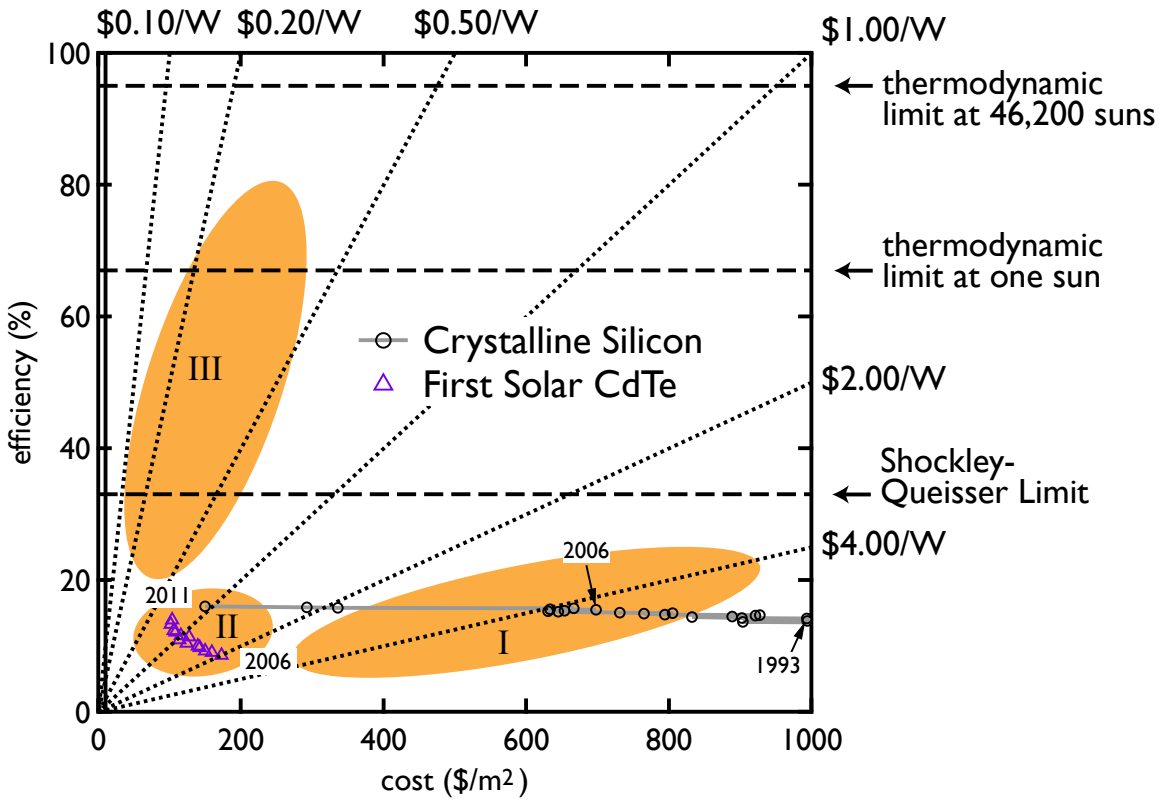

Figure 1.1: Cost lines versus power conversion efficiency and cost per square area. The vertical line represents the cost of roofing shingles, and some theoretical limits are drawn in horizontal dashed lines. Actual data points are from First Solar CdTe solar cells and the crystalline silicon "tier 1" market rates [5].

Initially, the tradeoff between cost and efficiency put solar cells like Silicon, CdTe, and multi-junction solar cells at fairly similar $\$/W_P$ values, even though they had different efficiencies and so were at different points on the line defined by Eq. 1.1. These cells are often termed "first generation" solar cells. Progress in the cost of photovoltaics (PV) can be thought of as moving up and across the plot from low-slope regions (I) to high-slope regions (II and III). Initially, this was mostly driven by approaches like thin-film CdTe solar cells (represented on Fig. 1.1 with First Solar data points in hollow triangles). These are systems that use less material and more inexpensive manufacturing techniques to lower costs without significantly losing in efficiency. Similar progress has occurred in crystalline silicon systems, where costs have fallen dramatically without any significant improvement in efficiency.

The past few years have seen a dramatic drop in PV module prices, due to a range of factors including the end of feed-in tariffs to support higher prices in many countries, improvements in efficiency and manufacturing, benefits from economies of scale, and the entrance of Chinese manufactured crystalline silicon solar cells. In fact, module prices have decreased to the point that the "balance of systems" (BOS) costs now make up more than half the cost of an installed solar panel system. The BOS cost includes things like inverters, batteries, installation, labor, and "rodent counter-measures." Global growth in production has been around 50% or more per year over the last 3-4 years, with a tenfold increase for 2011 from deployment in 2007 [5].

At some point, however, progress will be limited by the simple fact that solar cells are fairly complex systems, and there are fundamental limits on price imposed by the cost of the raw materials and the manufacturing processes necessary to assemble them properly (to provide a sense of scale, the price per square meter of roofing shingles is plotted as a vertical black line). At some point, improvements in efficiency will be necessary to progress into region III, where PV can reach a price where solar cells could become as ubiquitous as sunlight. Doing this will require approaching or exceeding limits set by early thermodynamic calculations, while working with a material that is both abundant and easily extracted.

This dissertation is a small part of an exploration of one idea that could challenge some of these thermodynamic calculations. In the following sections I will discuss quantum dots, their synthesis and characteristics, and why we think that multiple exciton generation (MEG) could make them particularly interesting. Then, I will introduce some basic physics of solar cells, and estimate how much MEG can do for us. In Chapter 2 I will present some work I have done to characterize the photoluminescence of colloidal quantum dots, a tool that we increasingly use, and I think will be important for optimization of engineered devices. Chapter 3 will introduce the solar cell structure that has worked best for our group, and some successful stability results. Chapter 4 will be a demonstration of MEG in the photocurrent of a solar cell, and Chapter 5 will have some speculation about the secondary chemical treatment that I developed to enable the MEG solar cell. Chapter 6 has some conclusions, perspective, and hopes for future research.

In order to provide some perspective on the broader field of solar cells, I include Fig. 1.2, a plot of record cell efficiencies measured at certified laboratories at the National Renewable Energy Laboratory, Golden; the Fraunhofer Institute for Solar Energy Systems, Germany; and the National Institute of Advanced Industrial Science and Technology (AIST), Japan. Quantum dot solar cells are one of the newest entrants to this plot, in the bottom right-hand corner.

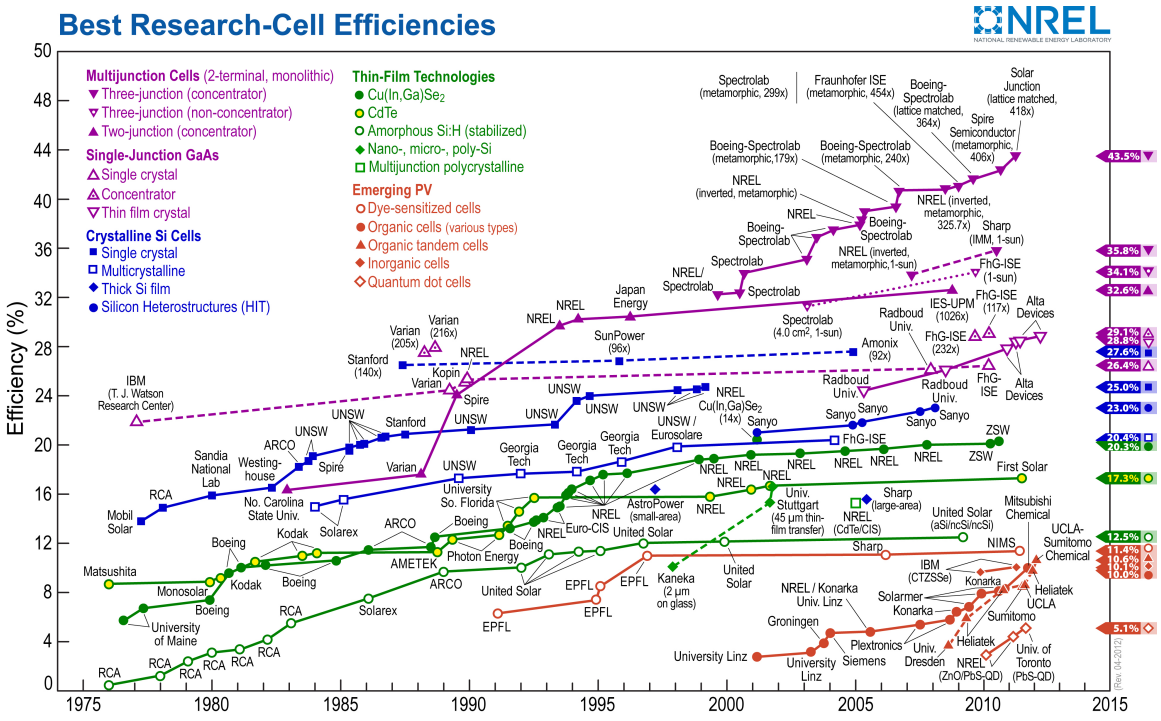

Figure 1.2: Certified record cell efficiencies for the past several decades of a range of PV platforms. Reproduced from [32].

Selected publications from my PhD work:

[**9**] Matthew C Beard, Aaron G Midgett, Matt Law, Octavi E Semonin, Randy J Ellingson, and Arthur J Nozik. Variations in the quantum efficiency of multiple exciton generation for a series of chemically treated PbSe nanocrystal films. **Nano Lett.**, 9(2):836–845, Jan 2009

[**93**] Octavi E Semonin, Justin C Johnson, Joseph M Luther, Aaron G Midgett, Arthur J Nozik, and Matthew C Beard. Absolute photoluminescence quantum yields of IR-26 dye, PbS, and PbSe quantum dots. **J. Phys. Chem. Lett.**, 1(16):2445–2450, Aug 2010

[**64**] Joseph M Luther, Jianbo Gao, Matthew T Lloyd, Octavi E Semonin, Matthew C Beard, and Arthur J Nozik. Stability assessment on a 3% bilayer PbS/ZnO quantum dot heterojunction solar cell. **Adv. Mater.**, 22(33):3704, Jan 2010

[**31**] Jianbo Gao, Craig L Perkins, Joseph M Luther, Mark C Hanna, Hsiang-Yu Chen, Octavi E Semonin, Arthur J Nozik, Randy J Ellingson, and Matthew C Beard. *n*-type transition metal oxide as a hole extraction layer in PbS quantum dot solar cells. **Nano Lett.**, 11(8):3263–3266, Jan 2011

[**94**] Octavi E Semonin, Joseph M Luther, Sukgeun Choi, Hsiang-Yu Chen, Jianbo Gao, Arthur J Nozik, and Matthew C Beard. Peak external photocurrent quantum efficiency exceeding 100% via MEG in a quantum dot solar cell. **Science**, 334(6062):1530–1533, Jan 2011

[**30**] Jianbo Gao, Joseph M Luther, Octavi E Semonin, Randy J Ellingson, Arthur J Nozik, and Matthew C Beard. Quantum dot size dependent J-V characteristics in heterojunction ZnO/PbS quantum dot solar cells. **Nano Lett.**, 11(3):1002–1008, Jan 2011

1.1 Colloidal Quantum Dots

This section will be a summary of the chemical, electronic, and optical properties of quantum dots, with some arguments about how quantum confinement, ligands, surfaces, etc. affect these. The interested reader should refer to excellent reviews of synthesis [41], electronic and optical properties [81], and MEG characteristics [8] of quantum dots.

1.1.1 Chemical and Physical Structure

A typical quantum dot used in this dissertation is made in a "one-pot injection," where the anion precursor is injected (under air-free conditions) into a solution of the cation precursor and ligand [39, 41]. In making lead selenide quantum dots the anion precursor is typically trioctylphosphine-Se (TOP-Se) or bis(trimethylsilyl)selenide (TMS2-Se), where the selenium can be swapped out for sulfur or tellurium to produce PbS and PbTe quantum dots. The TMS2-based compounds tend to be more reactive and are therefore useful for making tunable alloys [100]. The cation precursor is usually lead oleate, although preparations with oleylamine also exist [72]. The lead oleate precursor also will incorporate itself into the surface of the quantum dot as a solubilizing ligand, giving the stoichiometry of the quantum dot a size-dependent excess of lead [22, 72, 100]. This size dependence appears to be due to excess lead-oleate ligands coating the surface of the quantum dot at a ratio of one excess lead atom per oleate, with a surface configuration of two lead atoms sharing a single oleate ligand [73, 40]. A simplified cartoon of this lead chalcogenide quantum dot is shown in Figure 1.3.

In films of QDs, the atomic stoichiometry leads to interesting doping behavior. Thiol ligands, such as ethanedithiol (EDT), are commonly used to replace the oleate ligands in order to bring the films of QDs closer together in order to enable conductivity. When this occurs, the QD film becomes anion rich, since every surface lead is attached to the sulfur atom in the thiol ligand [40]. Since the anion is electron withdrawing, this dopes the film *p*-type [62]. Conversely, when other ligands (such as amines) are used to remove the oleate,

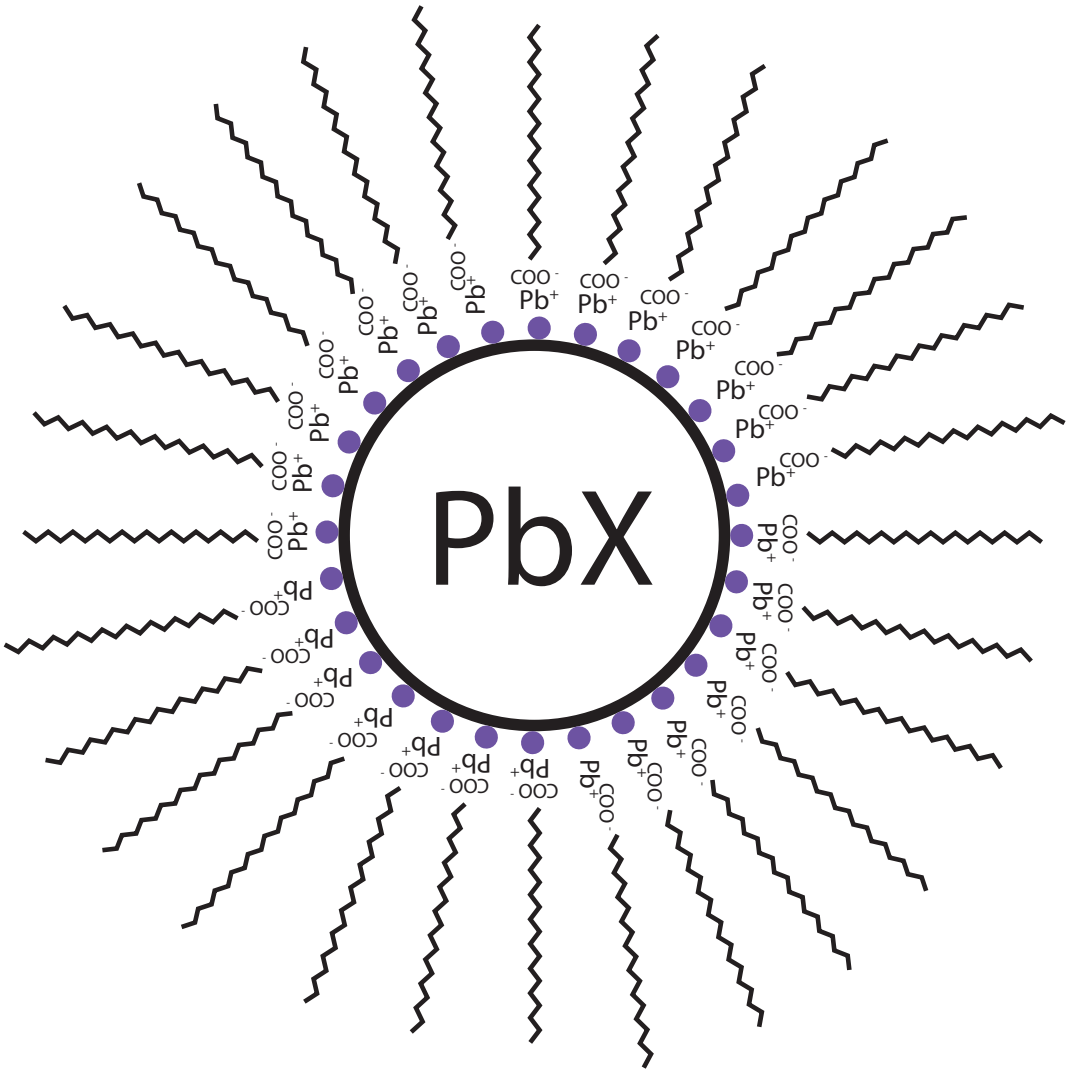

Figure 1.3: A cartoon diagram of a typical PbX (X = S, Se, Te) colloidal quantum dot. The purple dots are lead atoms, the COO^- represent carboxylate head groups, the zig-zags represent the long aliphatic chain of the oleate, and the PbX is a stoichiometric core. Note that the aliphatic chain actually contains one double-bond in oleic acid, and so should have a "kink."

either no binding occurs and the cation-rich film is doped n-type, or the amine itself dopes the film n-type [111].

Ligands and non-stoichiometries are predicted to introduce midgap surface states that could act as carrier traps in a solar cell [29]. This suggests that perhaps QD lead chalcogenide films should be tailored close to stoichiometric, as they are predicted to be defect free [26], or at least that better control over doping and stoichiometry would be useful for engineering devices from QD films. Clearly, the surfaces of these quantum dots will be important in their optoelectronic properties, and things like the chemistry of ligands, defect passivation, stoichiometry, oxidation, and surface reconstruction will play a role in this dissertation.

1.1.2 Electronic Structure

The bandgap of a quantum dot is expected to increase with confinement. What follows is a very basic estimate of what the bandgap increase, or confinement energy, should be for spherical quantum dots. A more thorough explanation can be found in many other resources [116, 4]. This problem can be understood by considering a very simple "particle-in-a-box" treatment. By solving the one-dimensional Schrödinger equation for a square well potential of diameter d and potential V_0 at the boundaries, we can extract the bound-state energies. We solve

$$\hat{H}\psi(x) = E\psi(x), \text{ for } \hat{H} = \frac{\hbar^2}{2m}\nabla^2 + V(x), \tag{1.2}$$

where the potential, $V(x)$ is

$$V(x) = \begin{cases} 0, & \text{if } 0 < x < d \\ V_0, & \text{if } x < d \text{ or } d < x \end{cases} \tag{1.3}$$

In the simplest case, we will take the limit $V_0 \to \infty$. This problem has been solved by virtually every aspiring physicist, yielding the solution inside the potential well

$$\psi_k(x) = \sqrt{\frac{2}{d}}\sin(kx), \tag{1.4}$$

where k satisfies the boundary conditions such that $k = n\pi/d$ (and n is an integer greater than 0). This gives the energy levels

$$E_n = \frac{\hbar^2 \pi^2 n^2}{2md^2}. \tag{1.5}$$

We can generalize this result to three dimensions by invoking a spherically symmetric potential of infinite depth and radius R, and solve the spherical Schrödinger equation with a set of Bessel functions (j_l) and spherical harmonics ($Y_{l,m}$). See references [116, 4] for a complete derivation:

$$\psi_\circ(r, \theta, \phi) = j_l(\kappa_{n,l} r) Y_{l,m}(\theta, \phi). \tag{1.6}$$

This yields an energy level dependence:

$$E_{nlm} = \frac{\hbar^2 \kappa_{n,l}^2}{2m}, \tag{1.7}$$

where $\kappa_{n,l}$ is determined by the boundary condition $j_l(\kappa R) = 0$. The indices n, l, and m determine the number of radial, angular, and azimuthal nodes of the wavefunction, respectively. The solutions do not have the same constraints on allowable modes as in the hydrogen atom – all combinations of n and l are allowed in combination (e.g. the $1p$ state is allowed). In fact, the $1p$ level is lower in energy than the $2s$ level, and there is no accidental degeneracy as in the hydrogen atom. These levels are typically named by the corresponding hydrogen atom nomenclature, and will make up the quantized energy levels of our ideal quantum dot.

We can analytically satisfy the boundary condition for the first Bessel function

$$j_0(\kappa_{n,l} r) = \frac{\sin \kappa_{n,l} r}{\kappa_{n,l} r} \tag{1.8}$$

with $\kappa_{n,l} R = n\pi$, where $n = 1, 2, 3, \ldots$ This means that the ground state has an energy of

$$E_{1s} = \frac{\hbar^2 \pi^2}{2mR^2}. \tag{1.9}$$

This confinement energy can become significant for semiconductor materials such as the lead chalcogenides used in this work, particularly for diameters below 10 nm. For example,

PbSe has an effective mass close to $0.04m_{electron}$ for both the electron and hole, so a quantum dot of radius 3 nm should have a confinement energy of about 1 eV.

Noting that Eq. 1.7 has the same form as the effective mass approximation, one way to think of the confinement energy is as the kinetic energy of particle in a semiconductor with parabolic bands, but where k is fixed by the boundary conditions of the spherical well. In the effective mass approximation, the energy of the conduction and valence band are approximated as

$$E_c(k) = \frac{\hbar^2 k^2}{2m_e} + E_g \tag{1.10}$$

$$E_v(k) = -\frac{\hbar^2 k^2}{2m_h}, \tag{1.11}$$

where m_e is the effective mass of the electron in the conduction band, and m_h is the effective mass in the valence band. In this picture, for completeness, we have to include the lattice potential, which is only satisfied by Bloch states, $u_{nk}(\mathbf{r})e^{ik\mathbf{r}}$. However, we can use a superposition of Bloch states to recreate an envelope function,

$$f_{sp}(\mathbf{r}) = \sum_k u_{nk}(\mathbf{r})e^{ik\mathbf{r}}, \tag{1.12}$$

and solving the spherical well problem with a lattice potential is reduced to that of the original spherical well problem. In order for this simplification to occur, we must assume that the periodic Bloch function $u_{nk}(\mathbf{r})$ does not vary much with k. All this results in that the single-particle wavefunction in our nanocrystal is

$$\Psi_{sp}(\mathbf{r}) = u_{n0}(\mathbf{r})\psi_\circ(\mathbf{r}), \tag{1.13}$$

where $\psi_\circ(\mathbf{r})$ is defined in Eq. 1.6. With this, we can estimate the energy of a hole or electron in the quantum dot. In order to estimate the energy of the exciton, however, we also need to include the attraction between the electron and hole. For small QD sizes, we expect the confinement energy to dominate over the Coulomb interaction because the former scales as $1/a^2$ while the latter scales only as $1/a$. In this regime, we treat the solution as two

independent wavefunctions f_{sp}, and calculate the exciton energy with a first order correction for their attraction

$$E_{exc}(\kappa_e, \kappa_h) = E_g + \frac{\hbar^2 \kappa_e^2}{2m_e} + \frac{\hbar^2 \kappa_h^2}{2m_h} - \frac{1.8e^2}{\epsilon R} \tag{1.14}$$

The first exciton is where $\kappa_h = \kappa_e = \pi/R$, giving

$$E_{exc}(\kappa_e, \kappa_h) = E_g + \frac{\hbar^2 \pi^2}{2m_r R^2} - \frac{1.8e^2}{\epsilon R}, \tag{1.15}$$

where m_r is the reduced electron-hole mass

$$\frac{1}{m_r} = \frac{1}{m_e} + \frac{1}{m_h}. \tag{1.16}$$

The interested reader should refer to ref. [81] for a more thorough derivation and explanation of these ideas.

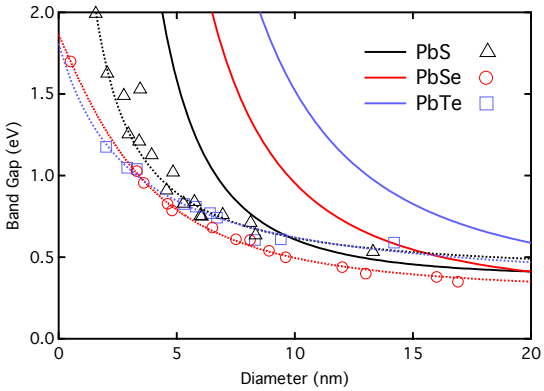

Figure 1.4: Comparing bandgap as a function of size for PbS, PbSe, and PbTe quantum dots. The solid curves are the calculated bandgap from Eq. 1.15, while the measured values are from our measurements as well as [77, 75]. The dashed curves are fits as per [75], Eq. 1.17.

While this qualitatively agrees with general trends observed for colloidal quantum dot solutions, shown in Figure 1.4 for PbS, PbSe and PbTe, and the energies are approximately of the right magnitudes, this is clearly incomplete. A better, purely empirical, fit is

$$E_g^{QD} = E_g^{Bulk} + \frac{1}{c_2 d^2 + c_1 d + c_0}, \tag{1.17}$$

where c_0, c_1, and c_2 are allowed to vary freely [75]. A least squares fit yields the better curves in Figure 1.4, although it does not provide much physical meaning. The difference between these two curves is a reduced dependence of confinement energy with QD diameter, and is partly due to the fact that the barrier at the quantum dot edge has finite height, among many other issues.

It is useful to compare the confinement energy to the Rydberg exciton binding energy

$$E_R = \frac{m_r e^4}{2\left(4\pi\epsilon\hbar\right)^2}. \tag{1.18}$$

In a material with dielectric constant ϵ, the Bohr exciton radius, a_B, is

$$a_B = \frac{4\pi\epsilon\hbar^2}{m_r e^2}. \tag{1.19}$$

Here we require that the electric field between the electron and hole be slowly varying on the scale of the crystal lattice. Using values gathered from the CRC Handbook of Chemistry and Physics [37] and the Physics of Semiconductor Devices [108], in Table 1.1 I have calculated the binding energy and exciton radius for the lead chalcogenides used in this work. Using the individual effective masses of the electron and hole, we can also calculate Bohr radii for each, a_e and a_h. Note that E_R is the same Rydberg energy of the hydrogen atom problem, with the only differences being the dielectric constant and that the reduced mass is no longer approximately the rest mass of the electron.

Table 1.1: Exciton Properties in Semiconductors

Material	E_g	ϵ_s/ϵ_0	$\epsilon_\infty/\epsilon_0$	m_e	m_h	m_r	E_R (meV)	a_B (nm)	a_e	a_h
PbS	0.41	169	17.2	0.08	0.075	0.039	1.8	23	11	12
PbSe	0.278	210	22.9	0.04	0.034	0.018	0.48	66	30	36
PbTe $\parallel$	0.31	414	33	0.24	0.31	0.140	1.7	13	7.3	5.6
PbTe $\perp$	0.31	414	33	0.024	0.022	0.011	0.14	150	73	80

In calculating the exciton binding energy and Bohr radius, special consideration must be given to the mechanism of screening. Transverse optical (TO) phonons will be responsible

for ionic shielding in a polar crystal lattice (i.e. shielding here means that all the positive lattice ions move towards the electron, while the negative lattice ions move away, as in the case of TO phonons). In order to experience the higher static dielectric constant, ϵ_s, the characteristic frequency of the binding energy of the exciton must be high enough to activate these modes, otherwise, the lower screening of ϵ_∞ is in effect. For the case of ionic materials with a large difference between anion and cation mass, such as the lead chalcogenides in this work, ϵ_∞ is most appropriate [90].

Since the confinement energy scales as $1/R^2$, we expect it to dominate over band gap and coulomb energies for small quantum dots. In bulk PbSe, for example, the large ϵ and the small m_r leads to a large Bohr exciton radius (66 nm) and a small binding energy (1 meV). It is tempting to assume that because the confinement energy can be large relative to the coulomb interaction, we can perhaps neglect coulombic effects in quantum dots, but this turns out to be incorrect for a variety of reasons (not least of which is MEG!).

1.1.3 Optical Properties

The optical and near-infrared absorption of colloidal quantum dots results from a modification of the bulk properties of the semiconductor by quantum confinement. Some sample normalized absorbance curves are plotted in Figure 1.5, for PbSe QDs with a range of sizes. Clearly, adjusting the size of the quantum dot has a significant effect on the first exciton peak energy and the onset of absorption. We typically use the peak of the $1s$ absorption peak ("first exciton") as the bandgap for the quantum dot. Above 2 eV, however, the absorption spectra of all of the quantum dots begin to merge (i.e. they have identical high-energy absorption spectra), with the possible exception of highly confined quantum dots such as the smallest shown here (with a first exciton of approximately 1.8 eV). This high-energy regime of the absorption spectrum has been shown to be very similar to bulk PbSe, with a correction for the volume of the quantum dot [75] and for local field screening [126], suggesting that the electronic structure becomes bulk-like well above the bandgap of

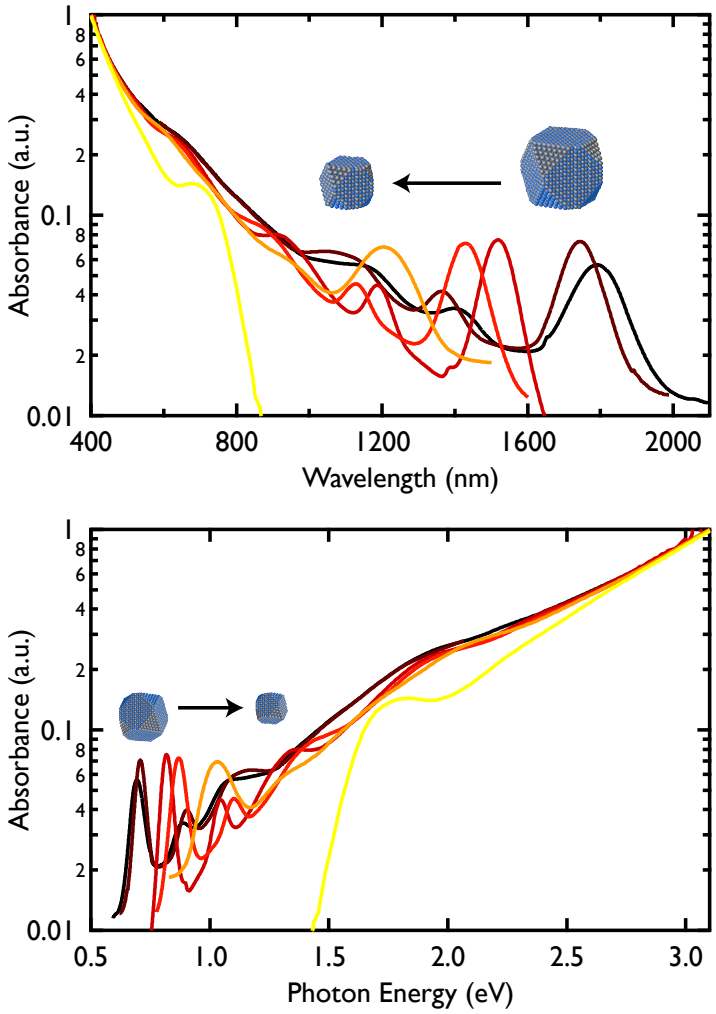

Figure 1.5: Normalized absorbances of a range of PbSe QDs, plotted on both photon energy and wavelength basis.

the quantum dot. This is somewhat intuitive, given that the wavefunction of highly energetic excitons is much smaller than the quantum dot volume, and so they would not experience the confinement effects of the boundary potential. This idea has potential implications for the efficiency of MEG, discussed below.

1.1.4 Multiple Exciton Generation in Quantum Dots

Bulk semiconductor materials have long been known to generate multiple excited electrons from high energy ultraviolet photons in a process termed Impact Ionization (II) [98, 118, 114, 99, 10, 125]. However, for lower-energy photons, the quantum yield (electrons generated at the band edge per absorbed photon) is unity, or less. This is because in bulk materials the thermalization rate k_{cool} is fast relative to the multiplication rate k_{mult} (see Fig. 1.6). To first order, we can estimate the quantum yield as a function of photon energy

$$\Phi(E) = 1 + \frac{k_{mult}(E)}{k_{cool}(E) + k_{mult}(E)}, \tag{1.20}$$

where above the MEG threshold k_{mult} tends to increase as E^2, while k_{cool} only scales weakly with E, if at all [8].

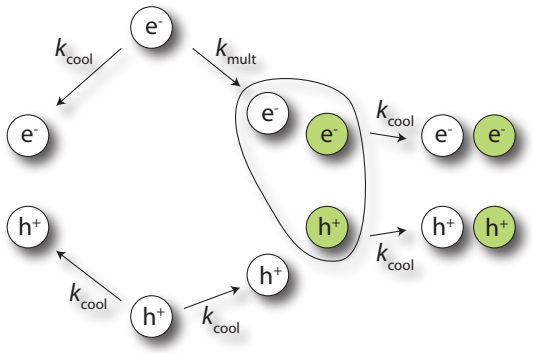

Figure 1.6: Diagram of the MEG process and the corresponding rates.

Thermalization, the process whereby electrons and holes cool to the band edge via emission of phonons, is rapid in bulk because the bands are quasi-continuous and phonons

can easily be emitted to facilitate cooling. Conversely, generation of multiple excited electrons requires higher energy photons because of momentum conservation and weak coulomb coupling.[2] In a quantum picture, this limits both the matrix element (W_C) between the ith highly energetic exciton state ($\langle X_i|$) and the jth multiply excited electron state ($|XX_j\rangle$), and it limits the **number** of states that are accessible by the energetic exciton. We can use Fermi's golden rule to make this explicit:

$$k_{mult} = T_{X\rightarrow XX} = \sum_{i,j} \frac{2\pi}{\hbar} |\langle X_i|W_C|XX_j\rangle|^2 \rho, \tag{1.21}$$

where ρ is the density of final states (states per unit energy). In bulk materials, W_C is zero for most transitions because of momentum conservation, while when it is nonzero it is small because the coulomb interaction is weak. Conversely, in QDs, W_C is larger and there are many more matrix elements that couple an $\langle X_i|$ to an $|XX_j\rangle$.

All of these characteristics that limit MEG (typically called carrier multiplication or impact ionization in bulk materials), are expected to be relaxed or improved in quantum dots. This was originally proposed in 2002 [82], spurring a burst of efforts to demonstrate this improved efficiency in colloidal quantum dots and in devices made from films of quantum dots. The arguments for enhanced efficiency of MEG in a quantum dot can be addressed from the basis of Eqs. 1.20 and 1.21, keeping in mind the competition between the rates k_{cool} and k_{mult}, as well as how they vary with photon energy.

"Phonon Bottleneck" Since the states in a quantum dot are quantized, simultaneous multiphonon emission is necessary to relax from an excited state to lower energy states, and eventually the $1s$ state. This suggests that k_{cool} could be slowed in quantum dots, leading to higher quantum yields. Recall that a slow cooling rate and high multiplication rate are desired for efficient MEG (Eq. 1.20). Unfortunately, the bulk-like band structure of QDs at high energies tends to limit the possible impact of a phonon bottleneck, and even

[2] For example, in a symmetric parabolic bands, the threshold for II is $4E_g$ See Appendix A.

at lower energies it has been shown to be very difficult to demonstrate slowed cooling in a quantum dot [83].

Coulomb coupling The matrix element is determined by the coupling between the X and XX states, and this is mediated by the coulomb interaction. Since quantum dots are small, the coulomb interaction is larger than in bulk materials, and we expect W_C to be larger. This enhancement of the coulomb interaction should be further enhanced when traversing low-dielectric media, such as the solvent surrounding the quantum dot, or the void space between quantum dots (this suggests that quantum rods and arrays of quantum dots **could** have further enhanced MEG efficiency).

Relaxed momentum conservation Since QDs are not infinite relative to the atomic lattice and electron wavefunctions, k is not a good quantum number and so crystal momentum is not necessarily conserved in energetic transitions. This relaxes the requirement that an energetic carrier relaxing in favor of promoting another carrier across the bandgap have exactly opposite crystal momenta. Alternatively, one can think of the excited and relaxed states in a quantum dot as superpositions of Bloch states (Eq. 1.12), in order to provide localization in space. Given this, the relaxed and excited states will have more of an overlap in this representation than they would in a bulk material.

1.1.5 MEG in QDs versus II in bulk

As noted above, the efficiency of impact ionization is fairly weak, and high ratios of photon energy to bandgap (about 4-5 times E_g) are typically necessary to elicit a quantum yield noticeably greater than unity. Such energies are typically outside the solar spectrum. The use of small bandgap bulk semiconductors is not helpful in this case since the photovoltage would be too low to obtain good power conversion efficiency. The efficiency of MEG has been well characterized in quantum dots with transient absorption spectroscopy, and

the photon energy to bandgap ratio at which quantum yields greater than unity is observed is significantly lower (about $3E_g$, see Figure 1.7). Therefore, it appears that in QDs k_{cool} is reduced, k_{mult} is enhanced, or both. Some have argued [89] that since the high-lying states (i.e. $3E_g$) in QDs are bulk-like, MEG should not be enhanced in QDs over their bulk counterparts. This, however, is an incomplete description, because the high-energy states must still couple into the relaxed states, which are significantly modified by quantum confinement.

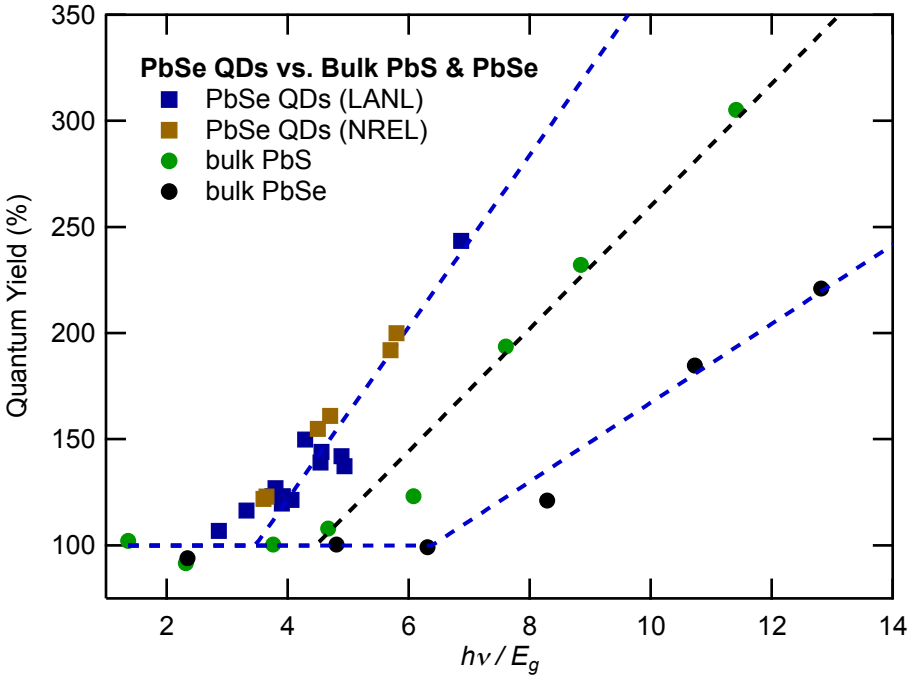

Figure 1.7: Comparison of quantum yield for bulk PbS and PbSe versus QD PbSe. Dashed lines are fits from Eq. 1.23. Adapted from [8].

Relatedly, others have argued [78, 89] that the only effect of quantum confinement is to raise the voltage at which carriers can be extracted, while at best preserving quantum yield on an absolute photon energy basis. While it is true that on an absolute photon energy basis, quantum yields for QDs are lower than their bulk counterparts, this again is incomplete, because the bandgap determines the minimum amount of energy needed to generate a second free carrier. Indeed, typically the number of extra carriers generated is

roughly linear with the bandgap, and the MEG threshold ($h\nu_{th}$) at which quantum yields begin to rise above unity will also determine the slope ($1/\varepsilon_{mult}$) of that linear relationship [8]:

$$h\nu_{th} = E_g + \varepsilon_{mult}. \tag{1.22}$$

One can think of ε_{mult} as the amount of energy necessary to generate an extra carrier. Above the MEG threshold E_g/ε_{mult} can uniquely describe the quantum yield as a function of $h\nu/E_g$ of a material to fairly good agreement:

$$QY = \left(\frac{h\nu}{E_g} - 1\right)\eta_{mult}, \tag{1.23}$$

where $\eta_{mult} = E_g/\varepsilon_{mult}$. This is the basis of the black dashed lines plotted in Figure 1.7. See ref. [8] for a complete derivation.

This slope-to-threshold relationship is the start of a rough model we can use to attempt to quantitatively describe the efficiency of the two processes related to MEG: cooling and generation of multiple excited carriers. Eq. 1.23 is limited because even for $\eta_{mult} = 1$ it can only give a straight line with threshold $2E_g$ and unity slope. While this obeys the energetic limit for MEG, the upper limit for MEG quantum yields is actually a staircase where photons with energy in excess of the bandgap produce as many excited electrons as is possible while still conserving energy (see the black curve in Fig. 1.8).

A model that can account for this was developed by Beard *et. al* in the same reference [8], and some sample curves from it are plotted below in Figure 1.8. Broadly, the model accounts for a competition between k_{cool} and k_{mult} in the form of an efficiency η_{MEG}, which in the limit $\eta_{MEG} \to 1$ gives the staircase energetic limit. A series of curves with labeled η_{MEG} are plotted to show this. The curves have been fit to spectroscopically-determined quantum yields for PbSe in bulk, quantum dot, and quantum rod forms. As we can see, yields are beginning to approach the staircase regime, where MEG could be making significant contributions to power conversion efficiencies. However, attempts to date to show MEG in a solar cell have until now proven difficult. A number of factors, including device

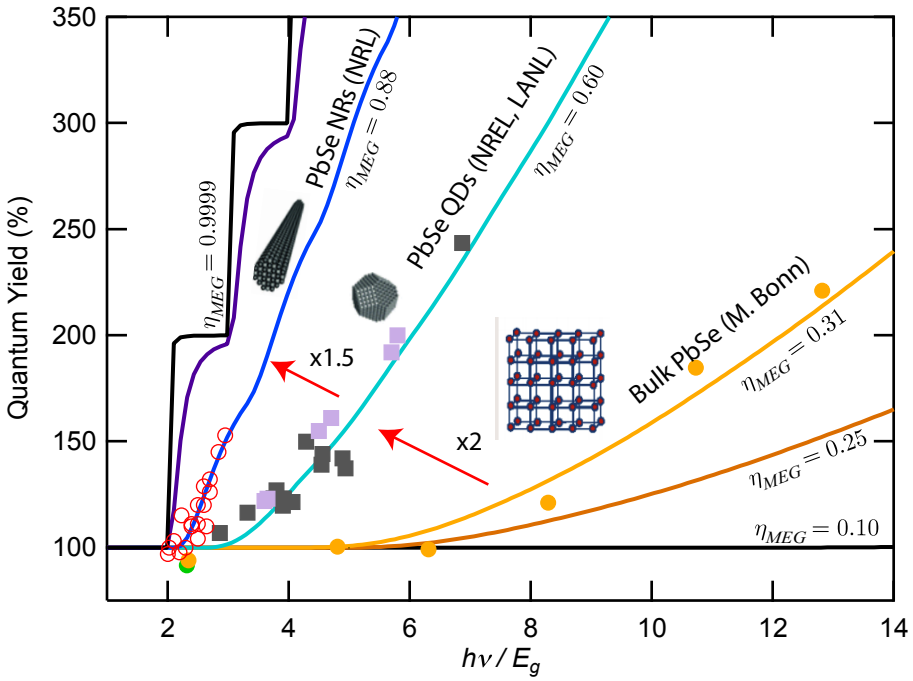

Figure 1.8: Quantum yields for a variety of PbSe structures. Solid curves are generated from their indicated η_{MEG} values, modeled as per [8]. Solid circles are for bulk PbSe (from [89]), solid squares are for PbSe QDs in solution (from [69, 71]), and hollow circles are PbSe nanorods in solution (from [21]). All data points were determined spectroscopically, *not* from actual solar cells.

architecture, surface passivation, and composition have prevented measurement of quantum yields anywhere close to unity.

Due to the fact that these quantum yields have been determined from transient absorption spectroscopy (TAS), there has been some dispute and disagreement about the true quantum yields. The uncertainty primarily arises because the TAS measurements are necessarily not absolute, but rather give the relative yield below and above the threshold for MEG. Some effects, such as pulse-to-pulse ionization of QDs, could lead to an artificially inflated ratio between the below- and above-threshold quantum yields. This led to some irreproducibility and exaggerated high values because the ionization of QDs depends on QD passivation, and whether the solutions were stirred (so as to make every pump pulse be on a new batch of QDs). Additionally, there was some question as to what the effect of electronically coupling QDs would be on the efficiency of MEG. Therefore, it became paramount to measure the quantum efficiency of an MEG QD solar cell, since there an absolute measurement of the number of carriers generated per photon could be performed.

1.2 Solar Cells

Solar cells specialize in converting photons to long-lived excited electrons and delivering them at an electric potential to an external circuit. Each electron carries an amount of energy limited by the bandgap of the material because this determines the energy level at which a large number of excited electrons can be held before relaxing across the bandgap (also termed "recombining" with a hole). In order to extract these electrons, some kind of asymmetry is employed to preferentially collect electrons and holes at opposite electrodes. The asymmetry can arise from differences in doping, electron affinity, or band levels, and generally results in selective contacts that preferentially accept or donate electrons. The power output of a solar cell is simply the product of the number of electrons generated (current) and the energy donated by each electron (voltage).

In this chapter I would like to explain to the reader the significance and interpretation of

JV and QE curves, two measurements that are used extensively in this work to characterize solar cells. We will link the interpretation to the physics and design of solar cells. This will culminate in a description of the "ideal solar cell." I will explain the origins of the "Shockley-Queisser" (SQ) detailed balance limit, and how approaches to boost voltage and current (MEG) are understood. This will include a discussion of previous II and CM work on bulk materials. The interested reader should see ref. [79] for a more complete description and derivation of the physics of photovoltaics.

Given that the surface temperature of the sun is 5778 K, we can estimate the thermodynamic limit for efficiency of an engine using the sun as a high temperature ($T_H = 5778$ K) reservoir and the earth as a cold temperature ($T_C = 300$ K) reservoir. The Carnot efficiency

$$\eta_{Carnot} = 1 - \frac{T_C}{T_H} = 95\% \tag{1.24}$$

of this engine is quite high, especially compared to the limits for solar cells that we are about to calculate. The reasons for this are many, but one of the first is that the sun is very far away, and therefore occupies a very small solid angle from the perspective of a flat-panel solar cell. This is problematic partly because the solar cell, just like the sun, must also radiate energy as any other black body. However, the solar cell will radiate in all directions, while unconcentrated sunlight covers only about 0.002% of the unit sphere. Usefully, this gives the upper limit on concentration of sunlight – regardless of how many lenses and mirrors one uses, the maximum concentration possible is about 50,000 suns.

The canonical solar cell has other losses as well, and these are addressed in a better estimate of practical limits called the "detailed balance limit," first described by Shockley and Queisser [96]. This limit makes a few additional assumptions for a single bandgap solar cell:

(1) Photons with energy less than the bandgap of the semiconductor are not absorbed.

(2) Energetic electrons created by high-energy photons immediately relax to the band

edge (i.e. the fraction of energy of photons with energy greater than the bandgap of the semiconductor is immediately lost to heat).

(3) The solar cell radiates light as a black-body, except below the bandgap, where the cell does not radiate.

In the intervening fifty years since the publication of their detailed balance calculation, no single-junction solar cell has been made a significant challenge to any of these assumptions. Multi-junction solar cells have adapted to these limitations by employing stacked films with bandgaps targeted to certain parts of the solar spectrum, and remain the state of the art for high efficiency solar cells [79]. I have calculated the losses entailed by each assumption for a single-junction device, they are plotted in Fig. 1.9 – assumptions (1), (2), and (3) lead to (respectively) 19%, 33%, and 15% loss in a silicon solar cell. These losses will vary with bandgap, leading to a "sweet spot" for the solar spectrum somewhere between a bandgap of 0.9 eV and 1.6 eV (in this range, power conversion efficiencies of 30-34% are predicted). It is important to note that the loss of energy in excess of the bandgap ("thermalization") is the largest loss by quite a bit.

1.2.1 The External Quantum Efficiency Curve

The probability that an incident photon of a given wavelength will yield an excited electron at the anode of the solar cell is termed the external quantum efficiency (EQE). A probability greater than unity (100%) would indicate that we were in fact generating multiple excited electrons per photon. If we could show quantum efficiencies greater than 100%, this would be a significant challenge to assumption (2) above because we now would be harvesting energy previously lost in the form of extra free carriers. Therefore, a careful measurement of EQE across the solar spectrum is an important tool for anybody making a solar cell, but especially so for those of us looking for signatures of MEG.

While a few variants on the method exist, the most common way to measure EQE is

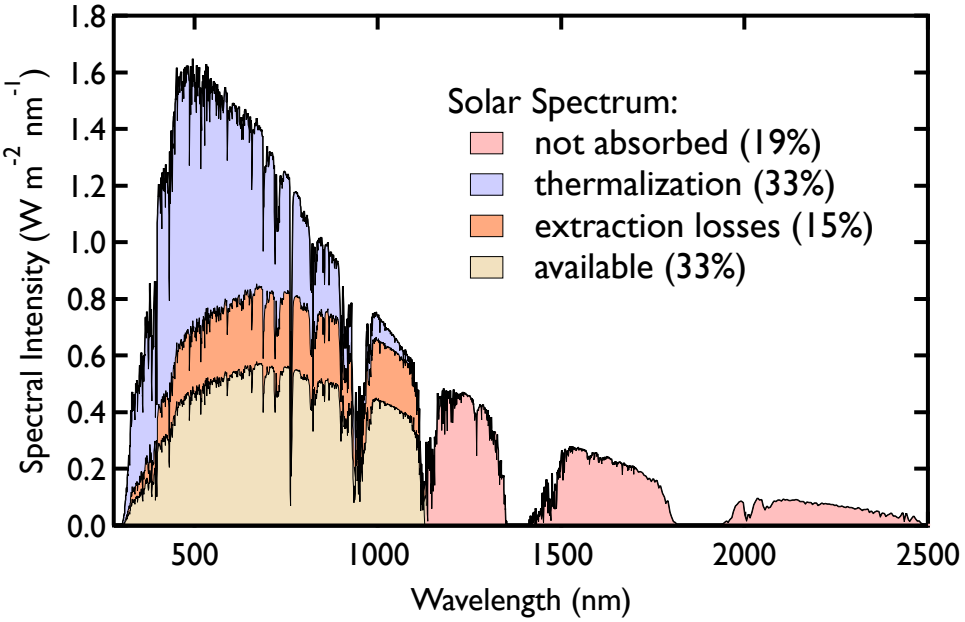

Figure 1.9: A visual representation of the losses inherent in a Shockley-Queisser solar cell. Note that thermalization (due to emission of phonons) is the largest, and increases for increasing photon energy. Extraction losses includes both radiative recombination, as well as "entropic" losses to extract the excited electrons before they recombine.

with a tunable monochromatic light source and a calibrated reference solar cell (or photodiode). Either simultaneously, or consecutively, the reference cell and test cell are illuminated with the desired wavelengths. The monochromatic light can be from a white lamp and grating spectrometer, LED, laser, or any similarly monochromatic light source. Typical spectral widths are about 10 nm. Often chopping or other forms of modulation are used with a lock-in amplifier to improve signal-to-noise. Once the current output (at short circuit) is measured, we calculate EQE_T of the test cell

$$EQE_T(\lambda) = \frac{I_T(\lambda)}{I_R(\lambda)} EQE_R(\lambda), \tag{1.25}$$

where I_T is the current produced by the test cell, I_R is the current produced by the calibrated reference cell, and EQE_R is the given EQE of the reference cell.

While mostly straightforward, this measurement can be complicated by spectral issues (wavelength shifting, higher grating modes, leakage of white light), calibration issues (changes in temperature, responsivity steepness, "cross-talk"), and different response times of the test and reference cells. Response times for solid-state solar cells are typically much faster than the chopping frequency (10-100 Hz), but in photoelectrochemical cells the response time can be too slow to keep up, and slower chopping (or none at all) becomes necessary. Avoiding regions where the reference cell is rapidly changing QE with wavelength is advisable, and in the case of lead chalcogenide devices it is necessary to use a second reference cell for the NIR wavelengths (such as Ge or InGaAs).

Optically, no monochromatic light source is perfect, and a few issues are worth highlighting. First, slight misalignments of the grating in the monochromator can lead to shifts in the peak wavelength selected by the slits. Second, higher modes of the grating will be reflected at the same angle as the fundamental wavelength desired (for example, at the angle corresponding to 800 nm, some 400 nm light will also be passed). These issues can be observed by using commonly-available CCD spectrometers, which we have used to fully characterize our monochromatic light source (see Fig. 1.10). We find minimal wavelength

shifting (< 5 nm), narrow peaks (FWHM ~ 10 nm), and very little leakage ($< 0.1\%$).

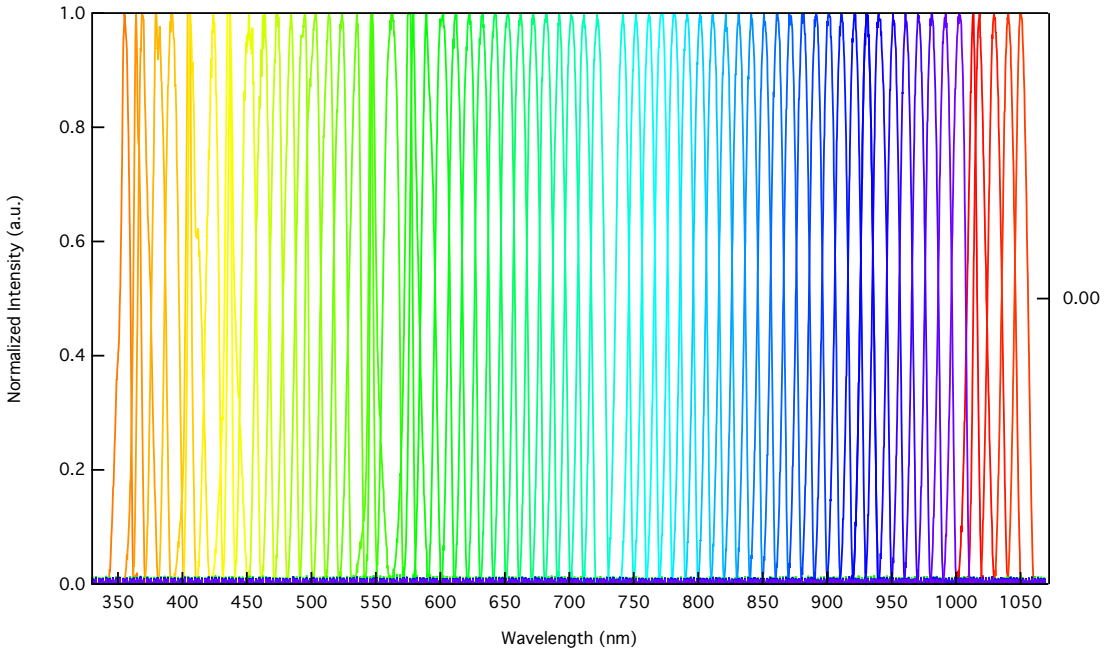

Figure 1.10: Characterization of the monochromatic light source used in measuring EQE. We measure the output of the fiber used to couple the monochromatic light into our glovebox, this time coupled to an Ocean Optics Si CCD spectrometer.

1.2.2 The Current-Voltage Curve

The typical solar cell can be modeled as a current source in parallel with a diode, as in Fig. 1.11. In the dark, the diode will have a current density of

$$J_{dark}(V) = J_0 \left(e^{qV/k_B T} - 1 \right), \tag{1.26}$$

where k_B is the Boltzmann constant, T is the temperature of the cell, and J_0 is a constant describing the amount of recombination in the solar cell. Later, we will show that in an ideal solar cell J_0 is determined by the black-body radiation of the cell, and that other forms of recombination can also contribute.

Under illumination, we can approximate the current density by simply subtracting the

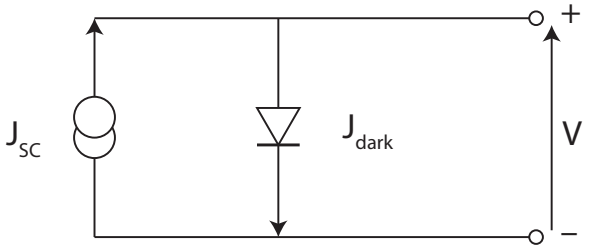

Figure 1.11: Equivalent circuit for an ideal solar cell.

amount of current generated by the current source at short circuit, J_{SC}:

$$J(V) = J_{SC} - J_0 \left(e^{qV/k_BT} - 1\right). \tag{1.27}$$

In an ideal solar cell we will assume that all of the light the cell can absorb is absorbed,

$$J_{SC} = q \int \frac{S(E)}{E} \phi(E) dE, \tag{1.28}$$

where q is the charge of an electron, $S(E)$ is the solar spectral irradiance at a given photon energy E, and $\phi(E)$ is the quantum efficiency of the cell. In the case without MEG, we use $\phi(E) = H(E - E_g)$, where $H(E - E_g)$ is a Heaviside step function with an onset at the bandgap, E_g. In the case with MEG, we use the energetically limited staircase function $\phi(E) = Floor(E/E_g)$. The solar spectral irradiance used is termed the AM1.5G spectrum, where AM1.5 indicates an "air-mass" of 1.5 atmospheres between the sun and the cell, and G indicates a fixed cell tilted at the sun absorbing diffuse light from all directions (i.e. globally). Another standard curve, AM1.5D exists for concentrating solar cells, since they cannot absorb diffuse light, and only absorb light directly from the solar disk. The AM1.5G is the top black curve, plotted as a function of wavelength in Fig. 1.9. If we know both J_{SC} and J_0, we can set $J(V) = 0$ and solve for the open circuit voltage,

$$V_{OC} = k_B T \ln \left(\frac{J_{SC}}{J_0} + 1 \right). \tag{1.29}$$

From the form of Eq. 1.29 we can see why concentration tends to help solar cells. Since J_{SC} and concentrated intensity will scale linearly with each other, one might expect no benefit

from concentration. However, the voltage will also increase logarithmically with intensity, leading to a roughly logarithmic increase of power with intensity.

In the detailed balance calculation, the only source of dark current is radiative recombination of carriers. At a cell temperature of T, we know black-body radiation will give a flux of photons

$$B(E) = \frac{2\pi}{h^3c^2}\left(\frac{E^2}{e^{E/k_BT}-1}\right). \tag{1.30}$$

However, under illumination there will be an additional population of energetic electrons, giving the system a positive chemical potential, $\Delta\mu$. This increases the rate of emission, modifying $B(E)$ by a factor of approximately $e^{\Delta\mu/k_BT}$:

$$B(E,\Delta\mu) = \frac{2\pi}{h^3c^2}\left(\frac{E^2}{e^{(E-\Delta\mu)/k_BT}-1}\right). \tag{1.31}$$

In a solar cell we assume that $\Delta\mu = qV$ across the whole cell. We find the dark current

$$J_{dark} = q\int B(E,qV)\phi(E)dE, \tag{1.32}$$

which gives the same approximate form as Eq. 1.26. The final current-voltage relation is

$$J(V) = \frac{S(E)}{E}\phi(E)dE - q\int B(E,qV)\phi(E). \tag{1.33}$$

Qualitatively, Eq. 1.33 will behave like Eq. 1.27 such that below the V_{OC} the current will be approximately the J_{SC}, but as the voltage approaches this limit the chemical potential will be come so high that radiative recombination will begin to compete with radiative generation and the current will drop to zero and below. The product of the current and voltage gives the power generated by solar cell, and dividing by the intensity of AM1.5G ($P_{sun} = 1000$ W/m^2) gives the power conversion efficiency (PCE):

$$PCE(V) = \frac{J(V)V}{P_{sun}}. \tag{1.34}$$

I have plotted an example of a JV curve calculated from the detailed balance and the resulting power curve in Fig. 1.12. The peak power point gives the load at which this cell will perform best.

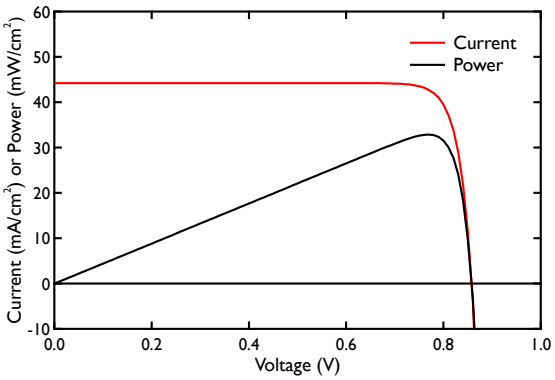

Figure 1.12: Detailed balance current and power versus voltage.

This analysis gives us a few ideas for design of a better solar cell. First, and perhaps most importantly, we find that while radiative recombination is unavoidable, reducing non-radiative recombination will directly improve the voltage of the cell. Note however, that from Eq. 1.29 we can see that voltage will only increase by $\sim k_B T \ln(J_{dark})$, so orders of magnitude changes in J_{dark} are necessary to yield large improvements in the voltage. Second, there is a balance between wanting to have a low bandgap so as to increase current and the need for high bandgap so as to retain high voltage. This balance leads to a variation of PCE with bandgap, which I have calculated in Fig. 1.13. As noted earlier, there is a clear region of ideal bandgaps, peaking around 30-34% for the non-MEG case. Some of this balancing act can be ameliorated by MEG, because now at somewhat smaller bandgaps solar cells will be able to harvest much more from high-energy photons without sacrificing much voltage. This can be seen in the red curve of Fig. 1.13, which peaks near 45% for $0.7 < E_g < 1.0$ eV.

A true solar cell will also have some additional leakage current against its polarity, giving a shunt resistance (R_{sh}), which can be drawn in parallel to the diode and current source. Additionally, there will be some series resistance (R_s) due to conductivities of the various layers in the solar cell that will lead to a loss of voltage at the load. Both of these can be incorporated into the equivalent circuit, giving the new circuit in Fig. 1.14. This

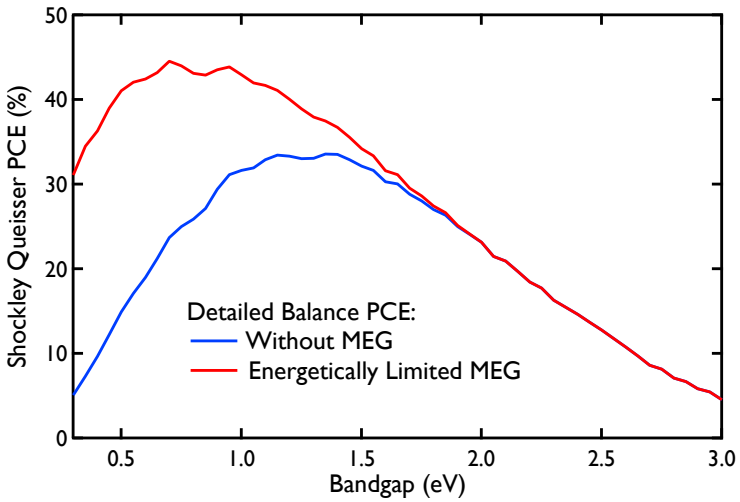

Figure 1.13: Detailed balance limit of PCE vs. bandgap, with and without MEG.

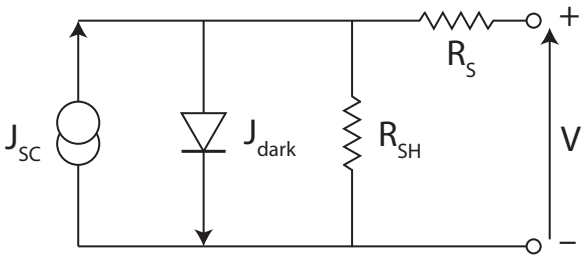

Figure 1.14: Equivalent circuit for a realistic solar cell.

modifies the current density equation,

$$J(V) = J_{SC} - J_0\left(e^{q(V+JAR_S)/k_BT} - 1\right) - \frac{V + JAR_S}{AR_{SH}}, \tag{1.35}$$

where A is the area of the solar cell. I have calculated the effects of R_s and R_{sh} for the semi-ideal Eq. 1.35 in Fig. 1.15. These characteristic resistances can be extracted from the slopes of the curves at large reverse bias (R_{SH}) and large forward bias (R_S), and we can see how the slopes will lead to losses in efficiency. Ideally, a solar cell would operate with its peak power point, P_{max}, as close to the J_{SC} and V_{OC} as possible. However, things like poor shunt and series resistance can pull the peak power point away from the corner of the square defined by the J_{SC} and V_{OC}. The ratio of the peak power point to the product of J_{SC} and V_{OC} defines the fill factor:

$$FF = \frac{P_{max}}{J_{SC}V_{OC}}. \tag{1.36}$$

As seen in Fig. 1.15, large R_S and small R_{SH} will hurt the fill factor of solar cells, separately from the properties that determine J_{SC} and V_{OC}. We also observe a very slight loss in V_{OC} with decreasing R_{SH}, and that only for very large R_S can we see an effect on J_{SC}.

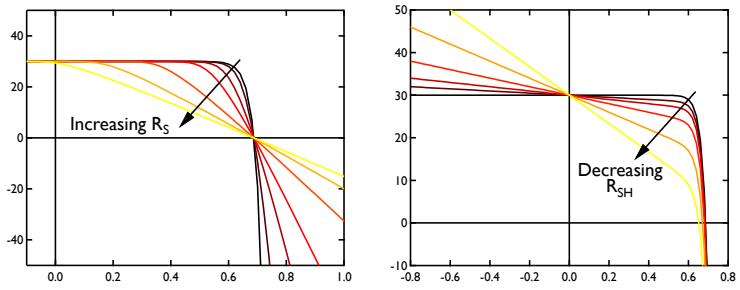

Figure 1.15: Effect of R_S and R_{SH} on current-voltage curves.

Chapter 2

Photoluminescence Characterization of Colloidal PbS and PbSe Quantum Dots

Adapted with permission from:

Semonin *et al.* Absolute Photoluminescence Quantum Yields of IR-26 Dye, PbS, and PbSe Quantum Dots. *J. Phys. Chem. Lett.* **1**, 2445 (2010).

2.1 Photoluminescence and its importance

Photoluminescence (PL) characterization of new quantum dot (QD) materials remains a powerful tool for monitoring material purity, passivation, reproducible synthesis, and overall quality. Upon absorbing a photon of light, an excited state is produced in the absorbing material that relaxes through a combination of radiative and non-radiative processes to return to its ground state. Knowledge of the PL quantum yield (Φ_{PL}) and the PL lifetime can often determine the associated radiative and non-radiative rates and thus establish time-scales for photoelectrochemistry or electron transfer. These time-scales are important to near infrared (NIR) materials because many optoelectronic devices of technological interest involve NIR emitting QDs [109], while still other applications include fluorescent labels for biological applications [2]. The easiest method with which to determine Φ_{PL} involves comparing the emission intensity of a known standard to the emission intensity of the sample of interest, where ideally both samples will have similar absorbances at the excitation wavelength and similar emission spectra. However, unlike the visible portion of the spectrum,

few efficient and reliable emitters are available for the NIR region [102]. One commonly used NIR emitting standard is 4-(7-(2-phenyl-4H-1-benzothiopyran-4-ylidene)-4-chloro-3,5-trimethylene-1,3,5-heptatrienyl)-2-phenyl-1-benzothiopyrylium perchlorate (known as IR-26 dye). IR-26 is reported to be relatively stable[49] and emits in a desirable range centered near 1130 nm, yet suffers from a narrow absorption spectrum and a very low emission yield. These drawbacks have led to poorly characterized optical properties with reported Φ_{PL} of either 0.5%[76, 122] or 0.14%[84]. Perhaps due to the remarkably low Φ_{PL}, estimations have been limited to a method based on the kinetics of the dye[84], rather than directly measuring the emission in an integrating sphere. Nonetheless, researchers use these values for comparison measurements of the Φ_{PL} of newly developed emitters.

Many reports suggest near-unity Φ_{PL} values are not only possible, but easily produced in NIR emitting PbSe QDs [122], yet few direct measurements of Φ_{PL} have been undertaken, as the comparative measurement requires less instrumentation and is easier to perform. Since PbS QDs are subject to the stochastic blinking phenomena[85] seen in visible emitting QDs [80], it is actually surprising that unity quantum yields are considered commonplace, further motivating our investigation of Φ_{PL} with direct methods. Besides the fundamental scientific importance, our interest in measuring Φ_{PL} of PbSe and PbS quantum dots (QDs) is also motivated by our desire to use Φ_{PL} as a tool to monitor sample quality through a variety of syntheses and treatments throughout the processing of these materials for use in photovoltaic devices [65]. In this letter we report the Φ_{PL} of IR-26 to be 0.05% and we find a size-dependent Φ_{PL} for PbSe and PbS QDs that is 60% for the smallest sizes and less than 3% for the largest sizes. This suggests that the Φ_{PL} for PbSe and PbS QDs may have been previously overestimated by approximately a factor of ten.

2.2 Measuring photoluminescence

See Figure 2.1 for a diagram for our setup used to measure absolute photoluminescence quantum yield. The absolute Φ_{PL} was measured in a LabSphere integrating sphere, with

excitation provided either by NIR-LEDs (emitting at 850 nm or 950 nm), or monochromatic light selected from a xenon lamp passed through a monochromator (PTI). Typical excitation bandwidths were 40-50 nm. The emission and excitation spectra were fiber coupled to the emission monochromator of the fluorescence spectrometer and measured with a two-stage thermocouple-cooled InGaAs photodiode. The excitation LEDs were driven by a 15 V square wave at 25 Hz using a Stanford Research Systems (SRS) DS335 function generator, while the xenon lamp-light was mechanically chopped at 22 Hz. The resulting InGaAs signal was amplified using an SRS SR530 lock-in amplifier, and spectra were corrected for grating, fiber, sphere and detector efficiencies using a calibrated lamp.

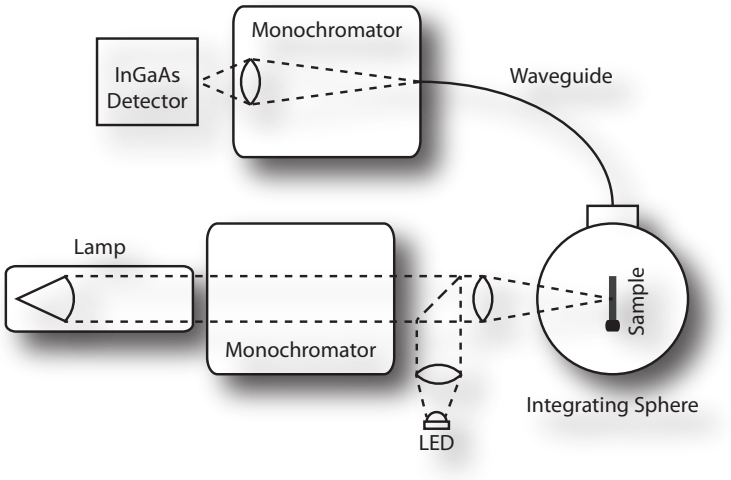

Figure 2.1: Diagram of photoluminescence quantum yield measurement.

Determination of the Φ_{PL} consists of integrating four spectral scans of the sample and of the "reference cuvette" (with solvent but without the fluorophore):

$$\Phi_{PL} = \frac{\int I_{sample}(\lambda) - rI_{ref}(\lambda)\, d\lambda}{\int E_{ref}(\lambda) - E_{sample}(\lambda)\, d\lambda} \tag{2.1}$$

where E_{ref} is the intensity of the excitation light measured with the reference cuvette, E_{sample} is the intensity of the transmitted and reflected excitation light with the test fluorophore, and I_{dye} is the intensity of the emitted light. Optionally, for weak emissions we remove

background effects by normalizing by r and subtracting the background emission spectrum (I_{ref})[1] . This same technique has been employed in QD photoluminescence measurements [12], and we have found that this approach yields reasonable results for Rhodamine 6G.

2.3 The PLQY of PbS, PbSe and IR-26

We measured the Φ_{PL} of IR-26 via the integrating sphere on three different batches of dye (from two different manufacturers – Acros and Exciton), and at a variety of dye concentrations. Our measurements all give a Φ_{PL} of IR-26 that lies approximately between 0.02% and 0.05%, depending primarily on dye concentration. Throughout the course of our experiments we have never measured a Φ_{PL} greater than 0.06%. 2.2a displays the absorbance (brown line, peaking at 1080nm) and emission (black line, peaking at 1130nm) of IR-26 dissolved in 1,2-dichloroethane (DCE); due to the overlap between emission and absorption we note a reabsorption dependence of the Φ_{PL} on the concentration of the dye (as measured by the peak optical density of the sample), shown in 2.2b. Additional effects may come into play at higher concentrations, such as aggregation of dye molecules. However, we do not observe spectral shifting or new spectral features even for the highest concentration tested, therefore we have ruled out aggregation effects. We have also eliminated aging and manufacturer as possible sources of error: month-old batches of IR-26 exhibit unchanged Φ_{PL} values, and samples from both of the primary suppliers of IR-26, Exciton and Acros, produce very similar results.

Considering only reabsorption effects, we can derive an approximate expression for the Φ_{PL} as a function of peak OD, when measured with a square cuvette and with the detector

[1] If the emission is particularly weak, background effects such as the tail of the excitation, or other unknown fluorophors in the system, can modify the observed emission spectrum. To account for this, we also collect a background emission spectrum with our reference. However, this is not our exact background. In fact, this is the light background associated with an excitation of a transparent cuvette, whereas we wish to remove the light background associated with the excitation of the dye or QD. This background will necessarily be lower due to absorption of the dye or QD. To normalize, we multiply the emission background by the ratio of the integrated excitations, $r = E_{dye}/E_{blank}$.

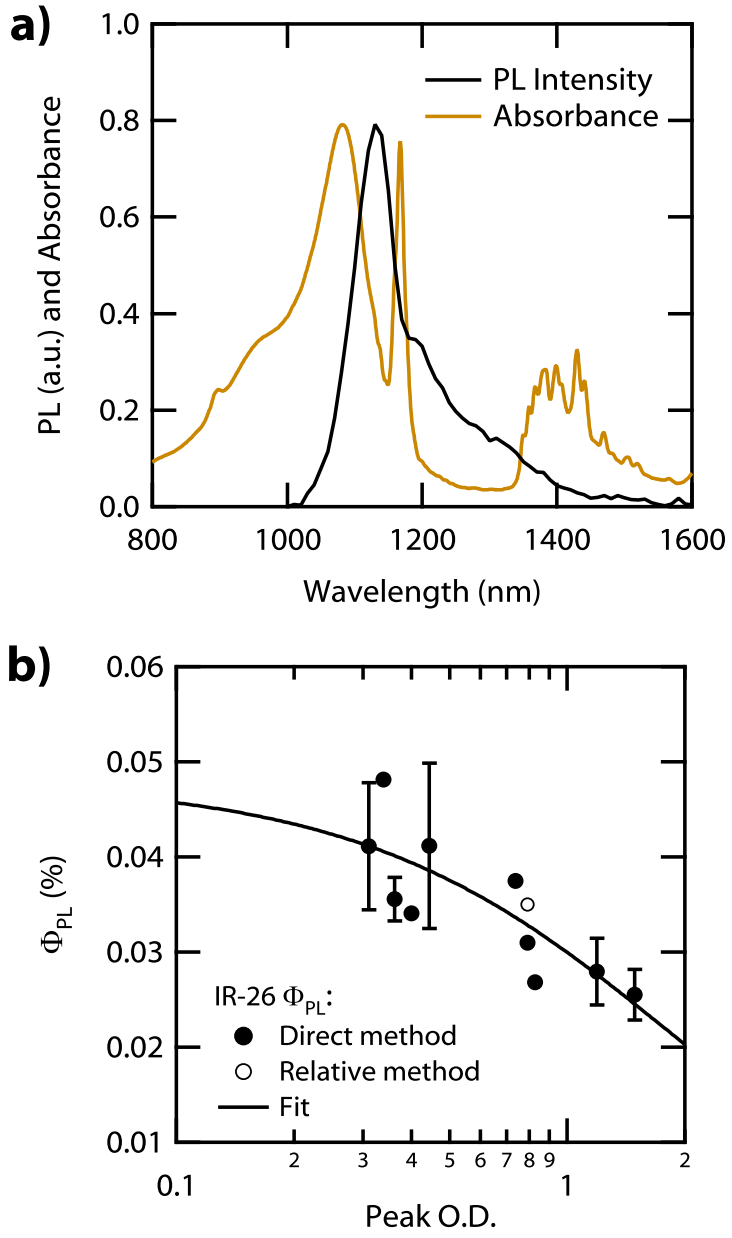

Figure 2.2: **a)** Photoluminescence (black) and absorbance (brown) of IR-26 in 1,2-dichloroethane (DCE). Note that the sharp absorbance features at 1170 nm and 1400 nm are due to DCE. **b)** Concentration dependent Φ_{PL} of IR-26. Some measurements were repeated 2-5 times to give a standard deviation – those points without error bars indicate peak OD's for which we have only one measurement. Filled circles represent direct measurements of Φ_{PL}, while the empty circle indicates a measurement relative to a known PbS quantum dot sample.

at 90 degrees from the incident excitation: [2]

$$\Phi_{PL} = \Phi_{PL_0} \frac{1 - 10^{-O \cdot A_{peak}}}{O \cdot A_{peak} \cdot \ln 10} \tag{2.3}$$

where Φ_{PL_0} is the inherent emission efficiency with zero reabsorption, A_{peak} is the peak optical density, and O is a normalized weighted average of the overlap between the absorbance (A) and emission (f) of IR-26:

$$O = \frac{\int f(\lambda) \cdot A(\lambda)\, d\lambda}{A_{peak} \cdot \int f(\lambda)\, d\lambda} \tag{2.4}$$

We find O to be approximately 0.45, such that the product $O \cdot A_{peak}$ is the average absorbance over the emission spectrum. While 2.4 is strictly valid for the case of 90° excitation and for low optical densities (OD) we expect that a more comprehesive analysis should not change this expression much because of the isotropic nature of emission and the nearly isotropic geometery that we employ (an excellent discussion of Φ_{PL}-measurement techniques, issues, and corrections can be found in Demas and Crosby's review [20]). This reabsorption function is applied to our observed data with Φ_{PL_0} as the only adjustable parameter; a non-linear least squares fitting routine provides a best-fit value of $\Phi_{PL_0} = 0.048 \pm 0.002\%$. Note that the observable Φ_{PL} will be lower due to self-absorption, therefore we recommend using 2.3 to determine the measurable Φ_{PL} when using IR-26 as a known reference dye.

To confirm our measured Φ_{PL}, the absolute Φ_{PL} of a PbSe QD sample was measured and then the Φ_{PL} of IR-26 was determined by the luminescence relative to the QD sample. An example of this is shown in 2.3; we use a PbSe QD sample with a first exciton transition energy at 0.98 eV as the standard and find the absolute Φ_{PL} to be 41%. We find that the integrated spectra of the QD sample is 1180-times larger than that of IR-26, yielding $\Phi_{PL} = 0.035\%$. That particular IR-26 sample had a peak OD of 0.79, and the yield falls

[2] We start with the infinitesimal contribution of a slice of the solution at position x along the emission axis inside the cuvette (the slice is perpendicular to the emission):

$$\Phi_{PL}(x) = \Phi_{PL_0} \frac{dx}{\ell} 10^{-\epsilon x c} \tag{2.2}$$

where ℓ is the side-length of the cuvette, ϵ is the molar extinction coefficient, and c is the molarity. By integrating and substituting the absorbance $A = \epsilon \ell c$, we find 2.3.

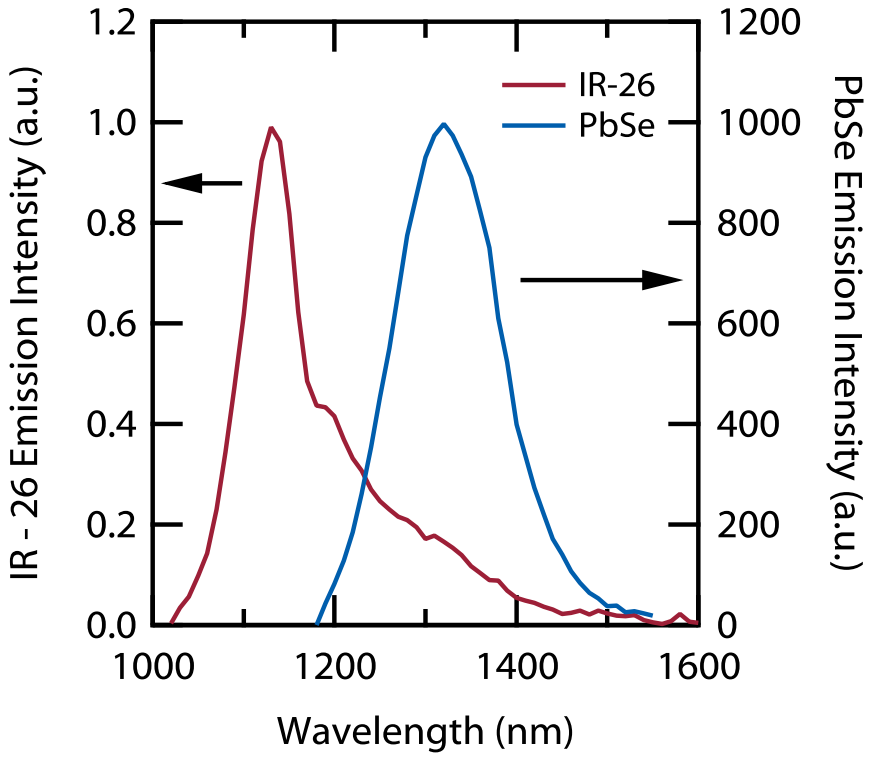

Figure 2.3: Comparison of relative photoluminescence spectra for IR-26 (left axis) and an 0.98 eV PbSe QD sample (right axis, same scale). Samples were prepared such that the absorbances at the excitation wavelength (890 nm) were similar (any difference was corrected for). We measured an absolute Φ_{PL} of 41% for the reference 0.98 eV PbSe QDs, and a corrected relative integrated emission ratio of 1180, giving a Φ_{PL} of 0.035%. The absolute method gave $\Phi_{PL} = 0.031\%$

on the line shown in 2.2b as the open circle. While not an independent measurement of the Φ_{PL} of IR-26, this demonstrates that the relative method can be effective and self-consistent with the direct measurement.

We have characterized the Φ_{PL} for a variety of PbSe and PbS QDs ranging in bandgap from 0.65 eV to over 1.3 eV (corresponding to diameters of $\sim$10 nm and $\sim$2 nm, respectively). The results are plotted in 2.4, including both raw data (orange and blue markers), and our various models of these results (dotted, dashed, and solid lines), described below. 2.4a displays Φ_{PL} and the absorption spectrum of the oleic acid capping ligand and 2.4b shows the measured Stokes shift for the same samples. The most dramatic trend we observe is a decreasing Φ_{PL} with increasing QD size, for both PbS and PbSe, that dominates over any minor differences in sample handling, preparation and treatments associated with solar cell construction. We have measured samples with trace impurites resulting from device fabrication, samples briefly exposed to air, samples with wider bandgap CdS or CdSe shells grown on the exterior, and samples with widely varying age, synthesized in house and obtained commercially (Evident Technologies, Troy, NY). While addition of $Cd(Oleate)_2$ to a solution of QDs does increase the Φ_{PL}[87], we find that this increase can usually be interpreted as a reduction of the PbSe/PbS core size via ion exchange of the surface Pb with Cd since the resulting Φ_{PL} typically falls on the trend line for a smaller QD. In addition to this excellent reproducability, it is remarkable that we find similar trends for both PbS and PbSe, suggesting that the primary source of the PL trend in these two QD materials is bandgap rather than size, surface chemistry, storage conditions, age, or even anion. Other work has shown both similar qualitative trends for PbSe [86, 107] and quantitatively similar values for PbSe/PbS core/shell/alloys [12]. In addition to this overall trend, there is a strong feature at about 1.1 eV, where the Φ_{PL} drops significantly, followed by a large increase to values in excess of 50%.

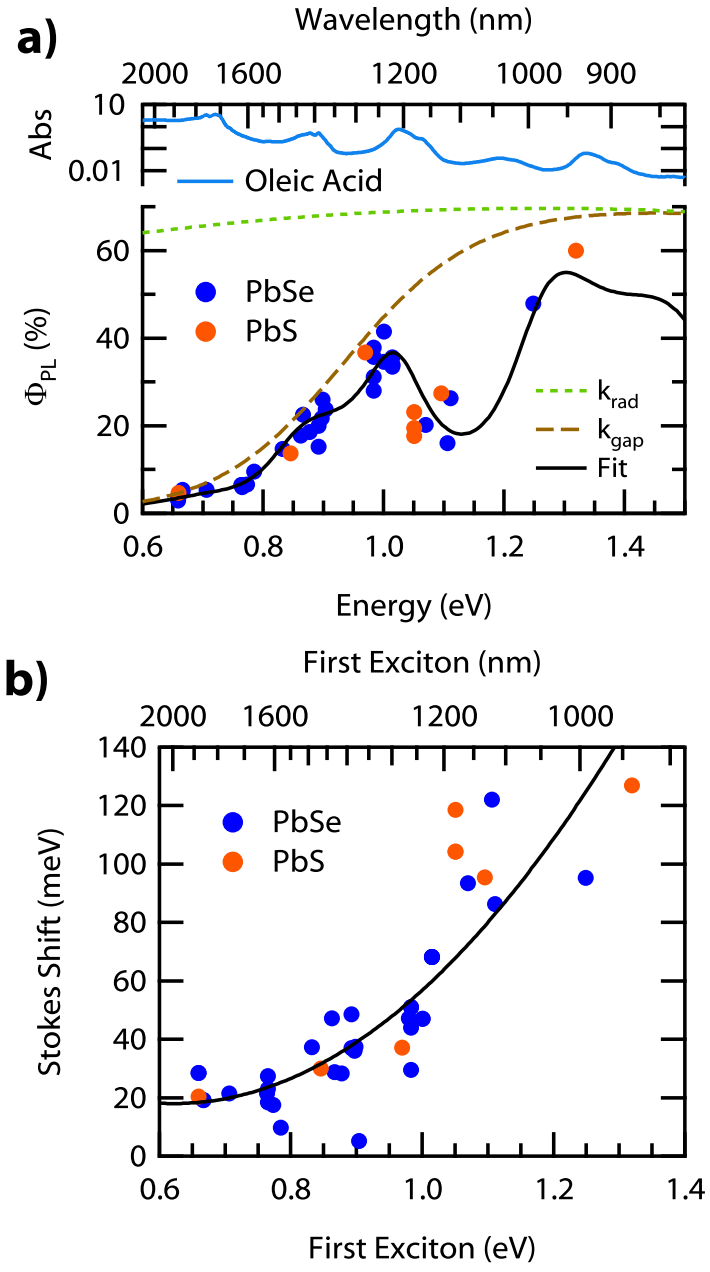

Figure 2.4: **a)** Φ_{PL} for PbS and PbSe quantum dots with various histories, plotted versus a range of bandgaps. For reference, the absorbance of the quantum dot capping ligand oleic acid is shown at the top. The dotted green curve labeled k_{rad} indicates the effect of non-radiative rates in addition to a constant trapping rate independent of size, while the dashed brown curve also includes the energy gap law. The black curve is a combination of the energy gap law and RET. **b)** The stokes shift for the same range of samples. The black curve is a second order polynomial fit, mainly to guide the eye, but also used in the RET model calculation elsewhere in this work.

2.4 A model for PLQY variation

To explain this drop and the overall trend, we modeled the following as sources of a size-dependent Φ_{PL}: (a) size-dependent radiative rates, (b) the "energy-gap" law for multi-phonon non-radiative relaxation to a dark trap state with a size-dependent depth, (c) energy loss via Resonant Energy Transfer (RET) to the vibrational modes of the oleic acid capping ligand, and (d) size-dependent scaling of surface defects. The Φ_{PL} is determined by the ratio of the radiative rate to the sum of all the relaxation rates, as in 2.5:

$$\Phi_{PL} = \frac{k_{rad}}{k_{rad} + k_{gap} + k_{RET} + k_{trap}}, \tag{2.5}$$

where k_{rad} is the radiative rate, k_{trap} is a trapping rate, k_{gap} is the multi-phonon relaxation rate, and k_{RET} is the rate of RET. The size-dependence of these rates is discussed below.

(a) Size dependent radiative rate – Like other QD systems [54], the oscillator strength for PbSe QDs has been shown to vary lineary with the diameter (d) of the QD [74]. The oscillator strength (f) can be related [127, 38] to the radiative rate for this transition through the Einstein coefficient as $k_{rad} = 1/\tau_{rad} = 8\pi e^2 f/4mc\epsilon_0\lambda_g^2$, where τ_{rad} is the radiative lifetime, e is the charge of an electron, m is the mass of an electron, c is the speed of light, ϵ_0 is the permittivity of free space, and λ_g is the wavelength of the first-exciton transition peak (or bandgap). If the oscillator strength varies linearly with size then we find that the radiative rate varies with size as:

$$k_{rad} = k_{rad}^0 \cdot d \cdot E_g^2 \tag{2.6}$$

where k_{rad}^0 is an arbitrary fitting parameter and E_g is the bandgap of the QD. We find that while this does predict a lower Φ_{PL} for larger QDs its dependence is much too weak to explain the large decrease in Φ_{PL} with increasing QD size (we show the predicted size-dependent Φ_{PL} as the dotted green line in 2.4a).

(b) Size dependent scaling of trap depth – The "energy gap law" [51] describes the variation of a multiphonon non-radiative transition rate (k_{gap}) with the energy differ-

ence between the two states involved in the transition, and we apply it to the transfer of an excited carrier into a dark trap state below the conduction band. Shown in 2.7, the exponential dependence on transition energy makes large energy transitions (such as directly from conduction to valence band) dramatically slower than those for smaller energies (such as those to dark states near the conduction band edge):

$$k_{gap} = k_{gap}^{0} \cdot e^{-\alpha(\Delta E_T(d))} \tag{2.7}$$

where k_{gap}^{0} and α are approximate constants, and $\Delta E_T(d)$ is the energy difference of the non-radiative transition. It should be noted that the nature and density of dark states near the conduction band of PbS and PbSe remains uncertain [3]; however, these traps are likely localized defects with energy levels that are mostly independent of bandgap, such that the transition energy from the conduction band into these trap states, $\Delta E_T(d)$, is larger for large bandgap QDs and thereby the trapping rate is much slower for large bandgap QDs than for small bandgaps. Indeed, work on InP [27] and ZnO [129] has shown that this is true for defects, and we expect the same to be true for PbS since the defect is chemical in nature and localized. Therefore, we assumed a transition energy that was linear with the bandgap, starting at 45 meV and ranging as high as 380 meV for the largest bandgaps, which is consistent with a constant trap level. These are the values we use for the $\Delta E_T(d)$ of the energy gap law model in 2.4a (dashed brown curve). This non-radiative pathway sharply limits the emission yields for small-gap QDs.

(c) Resonant Energy Transfer – Shown in 2.8, RET describes energy transfer from an excited QD to vibrational modes of the oleate ligands, where N_{RET}^{0} is a fitting parameter related to the number of absorbers per QD, κ^2 is a dipole orientation factor (we use 2/3 for isotropic orientations), n is the index of refraction of the solvent, $f_D(\omega)$ is the emission spectrum, $\sigma_A(\omega)$ is the cross-section of the absorber, and ω is the angular frequency of the emission [103]:

$$k_{RET} = N_{RET}^{0} \frac{18c^4\kappa^2}{\pi n^4 \tau_{rad} d^4} \int \frac{f_D(\omega) \cdot \sigma_A(\omega)}{\omega^4}\, d\omega \tag{2.8}$$

For any individual emitter/absorber pair there is a d^{-6} dependence, but in the case of QDs coupling to surface ligands there are multiple absorbers and the number of absorbers scales by d^2, so the dependence is reduced to d^{-4}. By assuming an approximated size-dependent Stokes shift (see 2.4b), a Gaussian-shaped emission spectrum, and by using the measured absorption curve of oleic acid we can simulate how RET may affect the Φ_{PL}. By combining with the energy gap law described above, we find a feature in our simulated Φ_{PL} (see 2.4a, solid black curve) that corresponds to one of the vibrational overtones of oleic acid which produces the feature at 1.1 eV in the observed data. The simulation also predicts a region above 1.3 eV that could also exhibit reduced quantum yields due to coupling with ligand vibrations. Similar ligand interaction has been observed in CdSe quantum dots, albeit for a different transition (from the $1P_e$ to $1S_e$ state), where relaxation rates varied by the type of capping ligand used, and a functionally similar energy transfer rate was derived [35]. It is possible that other mechanisms of coupling could be responsible for this reduction in Φ_{PL}. For example, Cooney *et al.* [18] have proposed a size-dependent wavefunction overlap with ligands that could produce a similar effect. However, we find that RET produces a better fit; dynamical measurements with core-shell structures could be used to explore this issue.

(d) Size dependent scaling of number of surface defects – We also considered the possibility of size-dependent surface defect scaling, but the data does not appear to support it as one of the primary effects. If we consider a surface with a constant defect density, then the number of defects per QD should increase with size as $N_D \sim d^2$, leading to a rate that also increases as $k_{trap} \sim d^2$, assuming that the trap depth is constant with size. However, we might expect the trapping rate to decrease with increasing QD size because of a weaker exciton wavefunction overlap with surface defect sites, suggesting that if there is a trapping rate power-law dependence, it will be something like $d^{2-\epsilon}$, where $\epsilon \geq 0$ and accounts for the size dependent overlap between core exciton and surface defect. Additionally, smaller dots should have greater curvature, more high-energy exposed surfaces, and more broken bonds – all of which are indicators for a greater density of defects. Thus, while trapping at surface

defects could qualitatively reproduce a size dependent Φ_{PL}, we rule out surface defect scaling because any size-dependence would vary more gradually than what our data suggest and we have tested many different QD samples that have different synthetic preparation, surface functionalizations and handling, yet the Φ_{PL} seems only to depend on the QD bandgap.

Since the excitation wavelength was typically kept within a small range while bandgaps varied, it is important to consider excitation-dependent photoluminescence. Previous work in CdSe [24] and InP [91] has shown that the Φ_{PL} can vary significantly with excitation wavelength, where the source of this effect has either been attributed to excited state trapping [95] or poor size-distributions[91]. However, we doubt this has much of an impact on our work for three reasons. First, we have taken a number of photoluminescence excitation (PLE) scans for fairly large PbSe QDs, and we see a response that closely matches the absorptance of the QD solution down into the visible wavelengths (this must be performed at low concentrations to avoid geometric effects from exciting the front of the cuvette). Second, the numerous transient absorption data published by us and other groups show very fast cooling to the band edge, and no fast component that would be a hallmark of trapping above the band edge (for example, this *is* seen by Sewall *et al.*). Third, some of the data in 2.4a was actually taken with excitation into the same absorption band (this is primarily because we move the excitation wavelength to avoid overlapping with the emission spectrum), and large changes in Φ_{PL} were still observed.

A non-linear least squares fit was applied to 2.5, where the adjustable parameters were k^0_{gap}, α and N^0_{RET}, allowing us to explore the relative impact of each effect. These various iterations are shown in 2.4a, and are labeled by the particular non-radiative rates used – note that the dotted and dashed curves include a constant trapping rate (i.e. independent of size), although the final fit (black curve) makes use of only the energy gap law and RET.

2.5 Conclusions

In this work, we have measured the Φ_{PL} of IR-26 and a large variety of sizes of PbS and PbSe QDs using an integrating sphere, and we have explored the causes of the variation in Φ_{PL} for these QDs. We find that despite differences in synthesis, the Φ_{PL} is mostly dependent on the QD bandgap, and that non-radiative multiphonon transitions into dark trap states plus energy transfer to oleic acid ligand vibrations appear to be responsible for the bulk of this variation. The fact that synthesis and sample handling has so little impact on PLQY suggests that the quantum dots are surprisingly robust, and that more significant changes in the surface chemistry will be necessary to affect PLQY and, likely, device performance.

In addition to using the integrating sphere to directly measure the Φ_{PL} of IR-26, we have inverted the relative measurement to use PbSe QDs as a standard and thereby have indirectly measured the Φ_{PL} of IR-26. Both methods yield a Φ_{PL} for IR-26 of 0.02-0.05%, substantially lower than 0.5% or 0.14%, commonly used in the literature (additionally, since PbS and PbSe QDs are so much more luminescent than IR-26 we can place an absolute upper limit of 0.1% for IR-26, otherwise the relative measurement would give unphysical Φ_{PL} values in excess of 100% for QDs). Finally, our results indicate that PbSe and PbS QDs are significantly more efficient IR-emitters than an organic dye and could be developed as a PL standard.

Chapter 3

PbS/ZnO Heterojunctions for Stable Quantum Dot Solar Cells

Adapted with permission from:

JM Luther, J Gao, MT Lloyd, OE Semonin, MC Beard, AJ Nozik. Stability Assessment on a 3% Bilayer PbS/ZnO Quantum Dot Heterojunction Solar Cell. *Advanced Materials* **22**, 3704 (2010).

The performance of thin film optoelectronic devices comprised of lead chalcogenide (PbX) quantum dots (QDs) has seen rapid development since 2005. Lead chalcogenides have uniquely large dielectric constants and therefore large exciton Bohr radii that result in a significant degree of quantum confinement [124]. For example, PbX QDs are easily synthesized with band gaps ranging from 0.5 to 2.0 eV [39, 25, 88, 50]. Such large Bohr Radii (18 and 47 nm for PbS and PbSe) and small effective masses for electrons and holes ($\sim 0.09m_e$) promote charge delocalization in QD films giving rise to an increase in charge carrier mobility and thus the conductivity. Field effect transistors in which current flows laterally, controlled by a gate bias, through a PbSe QD film on a Si wafer brought increased attention to PbX QD films. Soaking the film in hydrazine allows for an n-type gated response and control over the majority carrier type was demonstrated by thermal treatment which removes volatile hydrazine molecules resulting in p-type behavior [111]. Subsequently, Wang et al. directly demonstrated carrier type inversion in similar QD films through thermopower measurements [120]. In addition to short-chained amines like hydrazine and also butylamine [48], simple thiol-terminated molecules aggressively remove the native oleate ligand, and allow for strong

electronic coupling in QD arrays [46, 62, 66]. Along these lines, 1,2-ethanedithiol (EDT) has received considerable attention in coupled films of PbS and PbSe QDs. 1,4- and 1,3-benzenedithiol work similarly well and have been reported to increase the air stability of films due to reduced volatility compared to hydrazine or EDT [47, 68]. Additional studies of the structural, optical and electrical properties of coupled arrays of PbSe and PbS using a variety of thiols, amines, and acids have been reported [62, 52, 128].

From a materials standpoint, Wadia et al. has identified PbS as an abundant, inexpensive semiconductor material that is capable of supplying enough annual electricity to meet global demand, however it is limited by having a bulk band gap (0.41 eV) too low for general acceptance as a photovoltaic material [119]. By adding quantum confinement, the band gap can be tuned to 1-1.4 eV, thereby falling in the range that best optimizes electrical conversion of the solar spectrum.

Photovoltaic cells incorporating QDs of PbS, PbSe, and their alloy, PbSSe, were first constructed with a simple back-contact Schottky junction between a p-type QD film and a low work function metal electrode [46, 66, 47, 68]. Depositing the QD film onto ITO forms an ohmic contact and evaporating a metal with a low work function, such as Ca, Mg, or Al, forms the Schottky contact. Often, Schottky-junction PV cells suffer from low built-in voltages, thus limiting their power conversion efficiency. Several reports followed that employ n-type materials which form a heterojunction with the p-type QD film. ZnO, amorphous-Si, and C60 have been paired with PbS and PbSe to form heterojunctions [14, 56, 57, 105, 117]. Choi et al. showed that ZnO nanocrystals (NCs) can be spin coated on top of a PbSe film prior to deposition of the evaporated metal contact [14]. The NC ZnO layer helps to increase the voltage by creating a pseudo $p-n$ junction, since PbSe QD films treated with thiols show p-type behavior under illumination [62], and ZnO is a well-known n-type material. Leschkies et al. has shown ZnO/PbSe heterojunction devices where the ZnO is deposited below the QD film [56, 57]. The size-dependent energetics between PbX QDs and various other materials including ZnO are reported by the groups at Cornell [14, 42].

Placing ZnO under the PbSe film inverts the polarity of the device when a high work function metal is deposited on top of the QD layer. A similar geometry employed in the organic photovoltaic (OPV) community is termed an inverted cell because electrons flow toward the substrate rather than the evaporated metal contact, thus creating an inverted polarity [123]. For PbX QD solar cells, an inverted geometry advantageously locates the depletion region adjacent to the ITO, allowing the use of thicker films necessary for increased light absorption yet without compromising the utilization of high energy photons [53]. Leschkies et al. demonstrated that when ZnO nanowires penetrate into the PbSe QD film, 600 nm thick films could be used because the effective junction is extended throughout the film [57]. The inverted geometry allows for more stable contacts such as Au to be used vs. Ca, Mg or Al, which readily oxidize.

Tang et al. recently developed PbS QDs that exhibit high air stability [112]. When a film of ∼1.1-1.3 eV (3.5-5.2 nm) PbS QDs is deposited in air rather than in a glove box the devices exhibit increased stability in air. The authors employ LiF/Al/Ag as the low work function contact in a Schottky cell and demonstrate devices with enhanced stability compared to those with other contacts such as Ag or Al without LiF [113].

Here we constructed a cell composed of ZnO NCs similar to Choi et al. [14], in an inverted geometry similar to Leschkies et al. [56], using air stable 1.3 eV PbS QDs as described by Tang et al [112]. We used Au as the top contact without additional electron blocking layers. Figure 3.1 shows a schematic of the device architecture along with the energy band diagram at equilibrium.

After three days of storage in air, the device was submitted to the NREL measurements and characterization group for an official measurement of the AM1.5G 1-sun efficiency, η, calculated by

$$\eta = \frac{V_{OC}\, I_{SC}\, FF\, M}{A\, P_{IN}}, \tag{3.1}$$

where V_{OC} is the voltage at open circuit, I_{SC} is the current at short circuit, FF is the

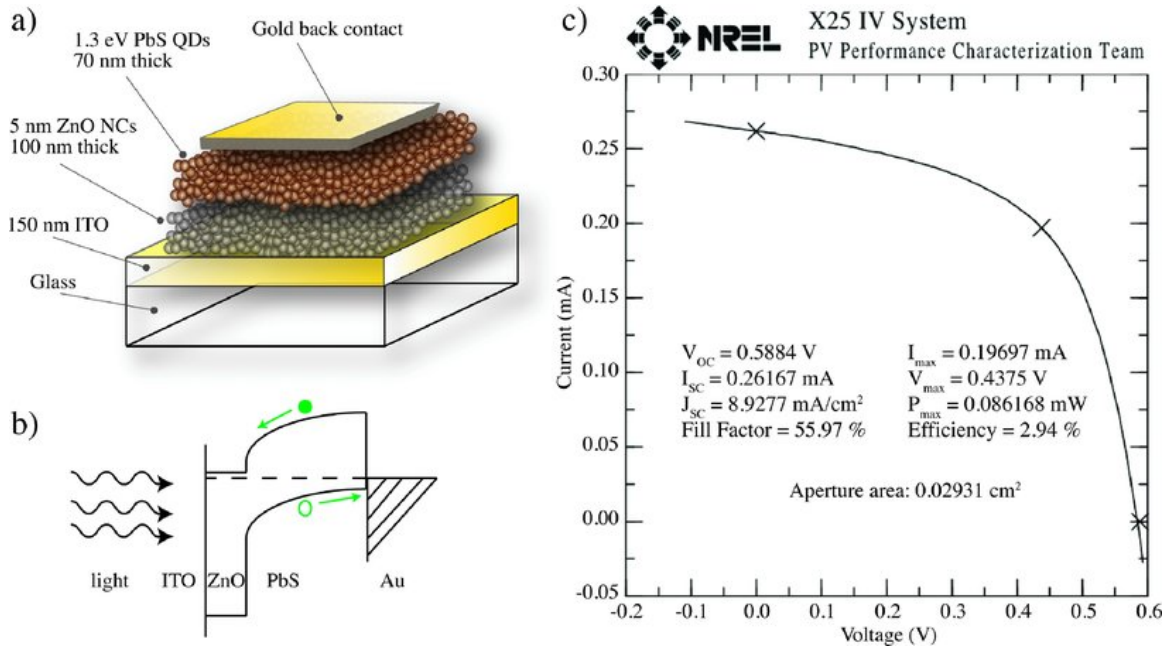

Figure 3.1: a) Depiction of the device structure used in this work. Light is incident through the glass. b) Proposed band diagram for the operation of the solar cell. c) Measured IV characteristics for ZnO/PbS nanocrystal heterojunction device. A copper aperture was placed over a 0.11 cm^2 area device so as to prevent photocurrent generated outside the active area of the cell. Various device parameters are listed in the inset.

maximum power divided by the $V_{OC}I_{SC}$ product, M is the spectral mismatch, A is the illuminated device area, and P_{IN} is the incident optical power density (1000 W m^{-2}). The spectral mismatch depends on the light source, reference solar cell, the spectral response of the device under test and the actual solar spectrum [97].

Figure 3.1c shows the light IV curve for the masked area device using the X25 solar simulator under standard test conditions. An overall efficiency (η) of 2.94% is obtained with V_{OC} of 0.59 V and current density (J_{SC}) of 8.9 mA cm^{-2}.

To assess the stability of the device, we performed a 1000-hour test in air under constant illumination with no encapsulation applied to the device. IV scans were continually recorded every 0.5 h to characterize the V_{OC}, J_{SC}, FF and η. Between scans, the device was subjected to a 500 Ω resistive load. The lifetime testing apparatus is configured for mild aging conditions where a sulfur plasma lamp intensity delivers approximately 65-70 mW cm^{-2} and the substrate temperature is maintained at ∼20 °C under ambient humidity. Figure 3.2 shows normalized values for the photovoltaic parameters. Due to the slightly different spectral output and intensity of the sulfur lamp compared to the AM1.5G spectrum, we refer to Figure 3.1 for the starting values for each metric.

As can be seen in Figure 3.2, the cell experienced minor changes over the 1000-hour light soak. A slight decay in the V_{OC} and FF is observed which are offset by an increase in the ISC. We speculate that the increase in the ISC is likely due to an increase in the conductivity of either the PbS film upon oxygen exposure [62], an increase in the ZnO film from continual illumination [14], or a decrease in the device resistance that may result from repetitive electrical measurement. This leads to a relatively unchanged device efficiency over the test period, which surpasses other PbX QD solar cells including those employing LiF as the electrode which degraded to near 87% of the initial efficiency after 63 h [113]. Upon concluding the 1000-hr test, the device was removed and the external quantum efficiency (EQE) was re-measured. Figure 3.3 displays the spectral response of the solar cell before and after the 1000 hr test in air. Additionally we show the absorption spectrum for solutions

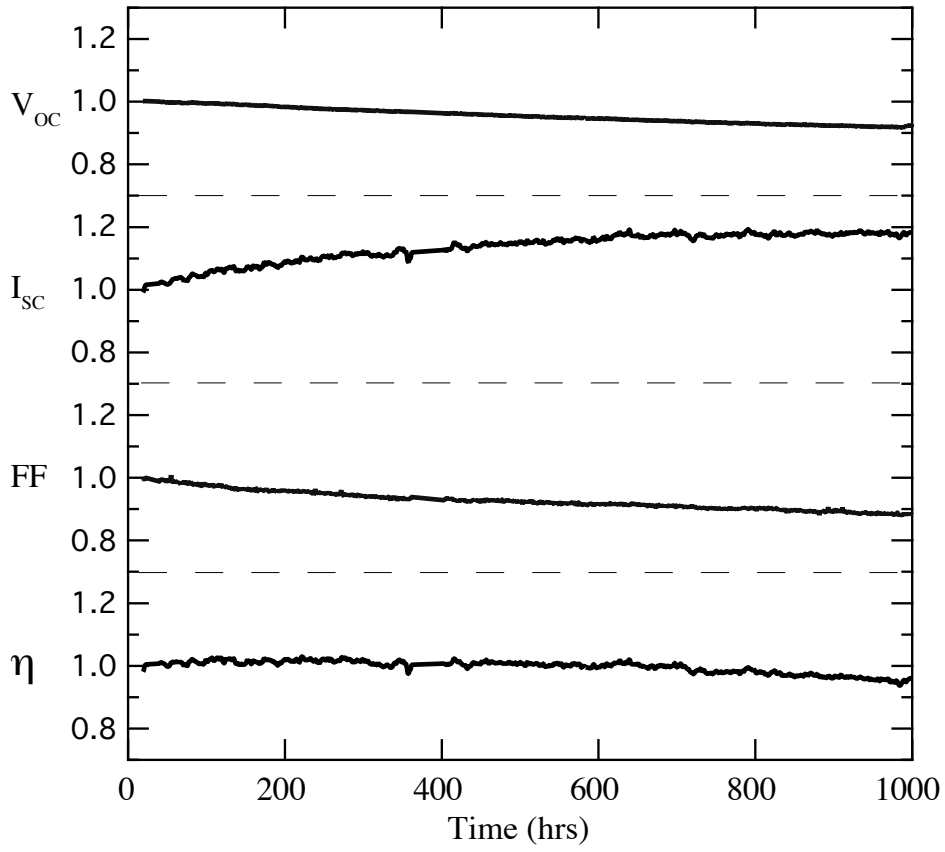

Figure 3.2: Device performance under constant illumination for 1000 h measured in air. IV scans are taken every 30 min for evaluation of each metric. The values are normalized on the unmasked device and we refer to Figure 3.1 for the initial values.

of the starting ZnO and PbS NCs. The onset of absorption for ZnO occurs at 356 nm which is out of the active spectral region for the solar cell. The characteristic first exciton peak of 1.3 eV PbS at 950 nm is present in the extinction as well as the EQE, and did not blue-shift even after the air exposure test. In light of recent reports showing a dramatic shift in the first exciton with exposure to air [128, 106], a stable spectral response further suggests a lack of destructive oxidation occurring throughout this assessment. Our stability result also compares favorably to other solution processed PV technologies such as OPV [130, 55]. Gur reported similar stability results after $\sim$ 200 h using CdSe and CdTe NCs annealed into bulk-like films at 400 °C in selenium rich environments [34], whereas the PbS film described here is not annealed and thus retains the favorable quantum confinement effects, such as a widened band gap. The widened band gap leads to a photovoltage greater than the bulk band gap of PbS, thus demonstrating suppressed recombination within the QD film with sufficient interQD electronic coupling needed for carrier transport in a quantum confined system.

Further gains in efficiency are possible in this architecture by employing larger band gap QDs to yield a higher V_{OC}, thicker PbS films to enhance J_{SC} and perhaps other n-type films below the QD layer. The performance demonstrated here represents a firm basis on which to compare future devices since this is the first QD solar cell with a certified 1-sun conversion efficiency. We demonstrate excellent stability in PbS QD-based solar cell for 1000 hours of continuous illumination in ambient air conditions.

3.1 Methods

3.1.1 Materials:

Zinc acetate (ZnAc2, 99.99%, Sigma-Aldrich), potassium hydroxide (KOH, certified ACS pellets, Fisher Scientific), lead oxide (PbO, Puratronic, 99.9995%, Alfa Aesar), hexamethyldisilathiane (synthesis grade, Sigma-Aldrich), oleic acid (OA, tech. grade 90%, Sigma-

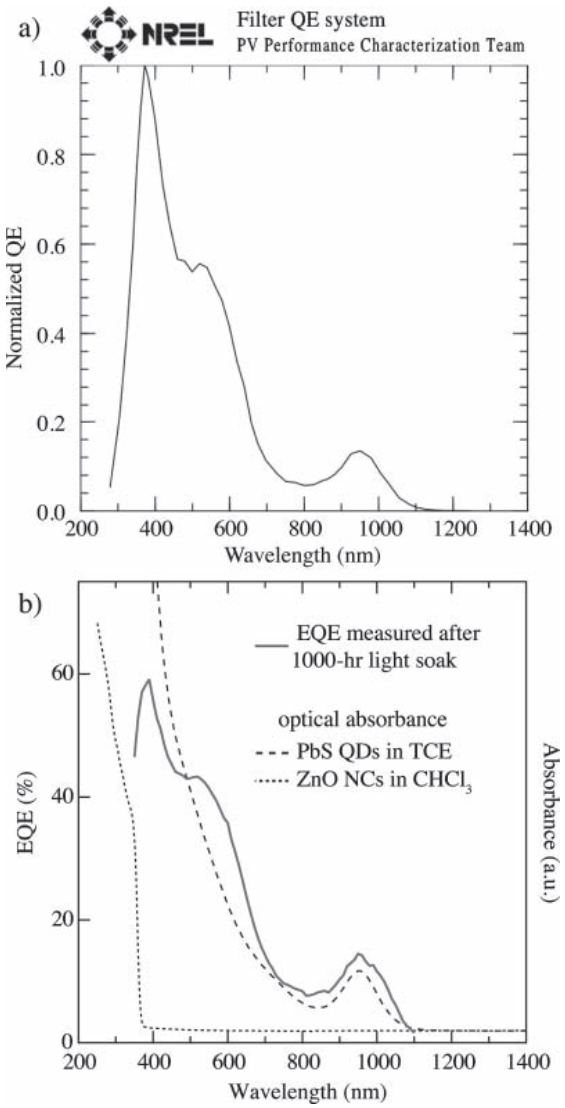

Figure 3.3: a) The normalized QE reported during the official measurement of the solar cell used for the calculation of the spectral mismatch. b) EQE spectrum of the device after the 1000-hour air stability assessment measured in our laboratory. The optical absorption of ZnO in chloroform and PbS in tetrachloroethylene is also shown for comparison. ZnO is transparent to wavelengths longer than 370 nm. The stable first exciton peak at 950 nm of the PbS QDs present in absorbance and the EQE of the device demonstrates the absence of destructive oxidation effects on the PbS film. The shoulder at 500-600 nm present in the EQE but not the optical absorbance is partially due to optical interference in the planar 70 nm PbS QD film.

Aldrich), 1-octadecene (ODE, tech. grade 90%, Sigma-Aldrich), 1,2-ethanedithiol (EDT, purum 98.0%, Fluka), chloroform (anhydrous, 99+%, Sigma-Aldrich), methanol (MeOH, anhydrous, 99.8%, Sigma-Aldrich), hexane (anhydrous, 95%, Sigma-Aldrich), ethanol (anhydrous, 99.5%), and acetonitrile (anhydrous, 99.8%, Sigma-Aldrich) were purchased and used as received.

3.1.2 Nanocrystal synthesis:

Synthesis of ZnO NCs was carried out by adding ZnAc2 (4.4 g) to MeOH (200 mL), heating to 60 °C and dropwise addition of a 0.4M KOH (100 mL) solution in MeOH. The solution was stirred at 60 °C for 2 h. The particles were extracted via centrifuge and resuspended in MeOH. This was repeated three times, and finally the dry ZnO powder was moved into a glove box and dispersed in CHCl3 (40 mL).

We synthesized PbS QDs with a first exciton peak at 950 nm (1.3 eV) by adding PbO (0.47 g), OA (2 g), and ODE (10 g) to a three-neck round bottom flask. This mixture was heated to 120 °C under vacuum for 2 h and then kept under N_2. In a glove box, hexamethyldisilathiane (180 μL) was mixed with ODE (5 mL) and loaded into a syringe. The contents of the syringe were injected into the flask and 1 min later the heating mantle was removed and the QDs were cooled to room temperature. The reaction solution was mixed with hexane (10 mL) and ethanol (20 mL) and centrifuged to extract the QDs. Hexane and ethanol were used again for an additional purification step, and the QDs were then suspended in hexane with oleate molecules capping the QDs and stored in air or a N_2 desiccator until use.

3.1.3 Device fabrication:

The ZnO nanoparticle solution was spin-coated at 2000 RPM for 1 min onto a cleaned glass substrate with prepatterned ITO electrodes (Thin Film Devices, Anaheim). The resulting ZnO film (100 nm thick) was annealed on a hotplate set to 260 °C for 30 min to

remove residual solvent. A PbS QD film was deposited onto the ZnO film via dip coating described previously [62]. In this case, the PbS QD film was deposited by 20 iterations of sequentially immersing the substrate into PbS QDs in hexane (concentration 10 mg $mL^{-}1$) and then 1 mM EDT in acetonitrile in a fume hood. Gold was then evaporated onto the top of the film at a rate of 0.2 nm/sec and base pressure of $10^{-}7$ Torr. A device is formed with an active area of 0.11 cm^2 defined by the overlap of Au and ITO. A copper mask was then adhered onto the glass with a defined aperture of 0.0293 cm^2 to rule out the errors in device area often seen with small area solution deposited devices formed without accurate mesa etches [19].

Chapter 4

Multiple Exciton Generation in a Quantum Dot Solar Cell

Adapted from:

Semonin *et al.* Peak External Photocurrent Quantum Efficiency Exceeding 100% via MEG in a Quantum Dot Solar Cell. *Science* **334**, 1530 (2011). Reprinted with permission from AAAS.

4.1 Introduction and history of QD solar cells

Multiple exciton generation (MEG) is a process that can occur in semiconductor nanocrystals, or quantum dots (QDs), whereby absorption of a photon bearing at least twice the bandgap energy produces two or more electron hole pairs. Here we report photocurrent enhancement arising from MEG in PbSe QD-based solar cells, as manifested by an external quantum efficiency (the spectrally resolved ratio of collected charge carriers to incident photons) that peaked at 114 ± 1% in the best device measured. The associated internal quantum efficiency (corrected for reflection and absorption losses) was 130%. We compare our results with transient absorption measurements of MEG in isolated PbSe QDs and find very reasonable agreement. Our findings demonstrate that MEG charge carriers can be collected in suitably designed QD solar cells, providing ample incentive to better understand MEG within isolated and coupled QDs as a research path to enhancing the efficiency of solar light harvesting technologies.

Third generation solar energy conversion strategies attempt to improve the overall

conversion efficiency by converting excess photon energy normally lost to heat into usable free energy [36]. One approach that has received considerable attention involves using quantum dots to harvest that excess energy as additional charge carriers via MEG [82]. A similar process occurs within bulk semiconductors (impact ionization); however it requires 7 eV (180 nm) photons to produce one extra carrier in silicon [13] and therefore is incapable of impacting solar cell technologies. MEG has been shown to occur in isolated PbSe QDs at about twice the efficiency [1] observed in bulk PbSe, demonstrating that quantum confinement can increase the efficiency of the primary conversion step from a high-energy photon to multiple charge carriers [70, 23, 8]. These studies utilized ultrafast transient absorption spectroscopy (TAS) to infer the number of electron-hole pairs produced per absorbed photon. Because of the indirect nature of the measurements, as well as the high photon fluences needed, there have been conflicting reports regarding the quantum efficiency determined from TAS [78, 69, 71, 6]. Furthermore, disagreements have arisen over the impact that MEG can have on solar energy conversion [8, 78]. Therefore, confirming the TAS results and demonstrating that MEG can occur in a working solar cell without external bias and under 1-sun solar intensities have been important research goals.

Two recent reports have shown progress towards these goals. Sambur et al. reported an internal quantum efficiency (IQE) greater than 100% in a photoelectrochemical cell consisting of a monolayer of PbS QDs strongly coupled to an atomically flat anatase surface [92], although the EQE and power conversion efficiency were small due to the limited absorption of the monolayer of QDs. Similarly, MEG has been invoked as an explanation for increased UV responsivity in PbS QD photoconductors [104] measured under a large external bias. However, showing an EQE greater than 100% without an applied bias has remained an open challenge. The EQE is a spectrally resolved photocurrent measured under zero external bias and represents the ratio of photocarriers collected by an external circuit to the number of

[1] The MEG efficiency, η_{MEG}, is related to the number of additional excitons per additional bandgap of energy carried by an absorbed photon after the threshold photon energy for MEG is passed.

incident photons at a given wavelength. This includes those photons that never reach the active layer due to reflection and absorption by inactive layers, so an EQE greater than 100% implies an IQE (restricted to photons absorbed by the active layer) that is possibly even greater. Here, we demonstrate a peak EQE as high as 114 ± 1% in a PbSe QD solar cell, providing definitive proof that MEG occurs in QDs.

Our approach towards this demonstration has been to form arrays of all-QD absorber layers that can be incorporated into suitable solar cell architectures such as Schottky-barriers and p-n planar heterojunctions (used in this study). The assembly of the QD layer must address a multitude of issues resulting from the synthetic techniques used to produce the colloidal QDs prior to deposition. Long-chain organic ligands, such as oleic acid, are used in the synthesis of PbSe QDs to control growth kinetics, allow for stable colloidal dispersions, and passivate surface states through their metal-ligand chemistry. However, when present in QD films they create a large barrier to electronic transport. Therefore these ligands must be removed while maintaining or improving surface passivation and thereby controlling the electrical properties [110]. Our most successful approach has been to treat the QDs with a short ligand that replaces the oleic acid during film formation. This is typically done in a layer-by-layer fashion [62], producing smooth pin-hole free layers.

The chemistry of QD surfaces has other important effects beyond improved conductivity. For example, we have studied MEG in coupled films of PbSe QDs using four distinct chemical treatments [63, 9]. Measured via ultrafast TAS, the MEG efficiency showed variations that were not simply related to the ligand length. Films treated with 1,2-ethanedithiol (EDT) showed a reduced MEG efficiency – in agreement with IQE measurements of Schottky-junction PbSe QD solar cells constructed using EDT [53] – whereas films treated with hydrazine, methylamine and ethanol preserved to varying degrees the MEG-enhanced QY measured in colloidal dispersions [9]. Early work [111] showed that hydrazine-treated PbSe QD films exhibit superior electron mobility on the order of 1 cm^2 V^{-1} s^{-1}, but no reports have successfully applied a hydrazine treatment to a QD solar cell. Conversely, although

dithiol treatments such as EDT and benzenedithiol produce lightly doped QD films with much lower carrier mobilities of 0.0004 to 0.06 cm^2 V^{-1} s^{-1} [59], they have successfully produced PbSe or PbS QD layers for either Schottky-junction [67] or planar heterojunction [56, 14] solar cells.

4.2 Materials and Methods

We used both hydrazine and EDT in a sequential fashion during deposition of the QD film used in the solar cells studied here. Device fabrication started with a transparent glass/indium tin oxide (ITO) superstrate, and we successively deposited a 40 to 60 nm ZnO layer, a 50 to 250 nm QD layer, and a thermally evaporated gold anode (SEM cross-section in Fig. 4.1A inset). We used layer-by-layer (LbL) EDT treatment [62] to deposit the majority of the QD film, followed by LbL-deposition of approximately 30 nm of QDs, using 1M hydrazine in acetonitrile to treat instead of EDT. The following details materials synthesis; device fabrication, characterization, and modeling; and details of the MEG model used.

4.2.1 Synthesis of PbSe Quantum Dots

All chemicals unless otherwise noted are purchased from Sigma Aldrich and were anhydrous if available. Synthesis follows previous work ([53, 66]. Lead oxide (1 g, 99.9995%, Alfa Aesar), oleic acid (3-5 g, 90%), and 1-octadecene (10 mL, 90%) are added to a 100 mL round bottom 3-neck flask and are heated to 120°C under vacuum on a Schlenk line to complex lead oleate. Under N_2, the flask is heated to the desired injection temperature (normally 150-180°C) and 15 mL of 1 M Se (99.99%) dissolved in tri-n-octylphosphine (97%, Strem) is injected along with 0.15 g diphenylphosphine (98%). Size is controlled mainly by reaction time and injection temperature. The reaction is cooled by placing the flask in room-temperature water after 2-4 minutes of growth and 10 mL of hexane (95%) is injected. The flask is then transferred to a helium-filled glovebox where ethanol (99.5%) is added to

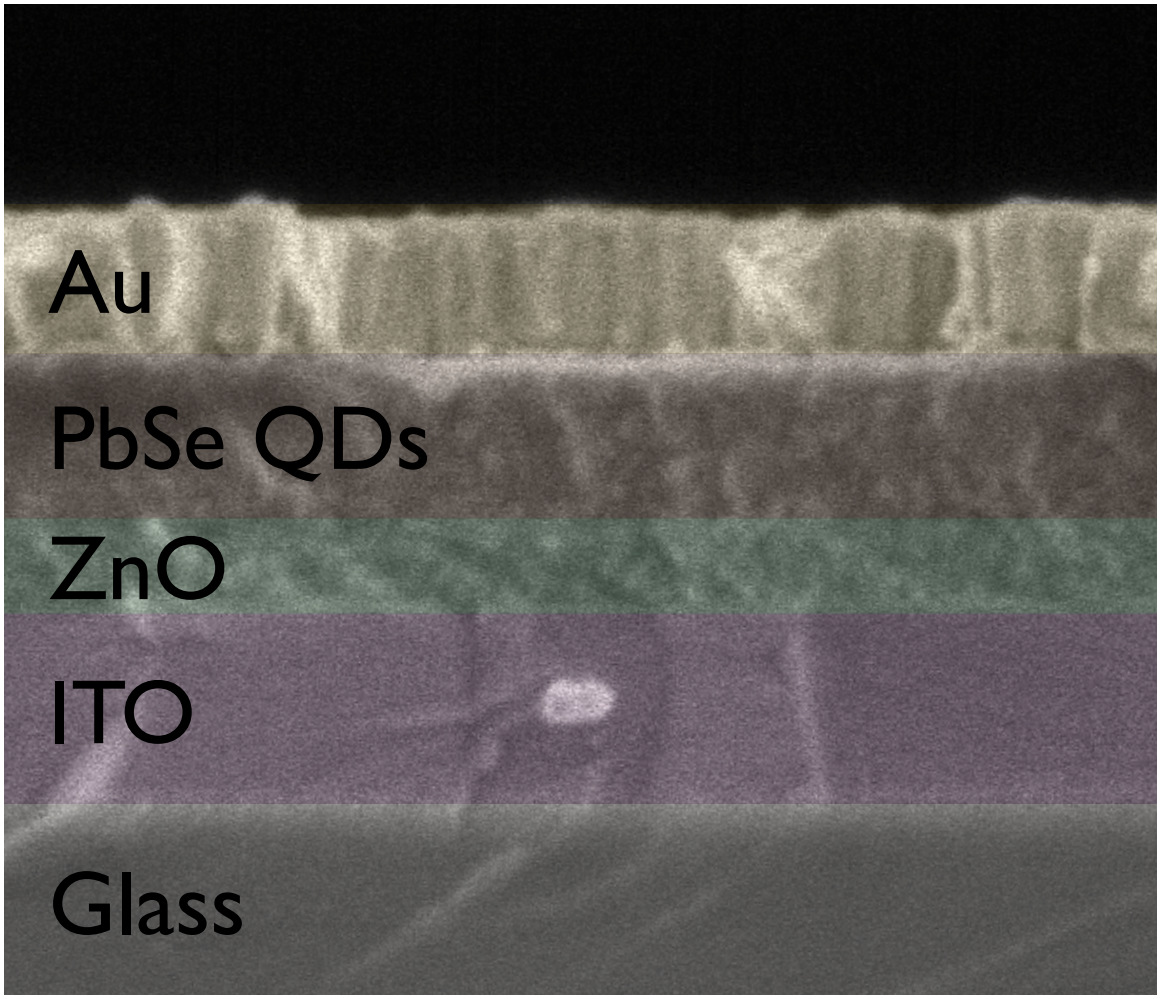

Figure 4.1: False color cross-section SEM of a typical MEG solar cell.

the reaction solution to extract the QDs via centrifugation. Hexane and ethanol are used for two additional cleaning steps. The final product is weighed and suspended in hexane at 20 mg/mL for dip-coating.

4.2.2 Substrates

Glass substrates with patterned indium tin oxide (ITO, 150 nm thick, 20 Ω/square) are purchased from Thin Film Devices in Anaheim, CA. The substrates are cleaned by ultrasonication in organic solvents and 100 nm Ag bus bars are evaporated just outside the edge of the device to lower the series resistance due to the extended ITO cathode. A 40-60 nm ZnO film is then deposited via a sol-gel process described in ref. [61]; a modified procedure developed by Beek **et al.** [11]. This recipe uses one part diluted diethylzinc (DEZ) in toluene (15% by weight, caution: diethylzinc is pyrophoric), dissolved into 1-4 parts anhydrous tetrahydrofuran (THF) prepared under N_2. I have found that relative atmospheric humidity can impact the optimal ratio of DEZ:THF – in the winter it appears that lower concentrations of DEZ (e.g. 1:2 or 1:4) produce robust films of ZnO, while in the summer a 1:1 ratio is necessary. This could either be necessary to match stoichiometry during reaction, or – more likely – to compensate for reaction of the DEZ with excess atmospheric humidity. The solution is spun-cast in air at 4000 rpm for 30 seconds, rested at room temperature for 15 minutes and then annealed at 130°C for 5 minutes.

4.2.3 Device Assembly

PbSe QD films are assembled in a helium filled glovebox using the layer-by-layer dip-coating deposition as described previously [62], with modifications for the secondary treatment with hydrazine. Normally, we perform 10-20 cycles of PbSe QDs (concentration 20 mg/mL) in hexane with 0.005M 1,2-ethanedithiol (98%) in acetonitrile (99.8%) using a NIMA Technology (Coventry, England) dip coater, followed by 5 more cycles with 1M hydrazine (98%, caution: explosive) in acetonitrile using the same PbSe solution. While

the EDT layer is 50-250 nm thick, the hydrazine layer is only 30-50 nm in thickness, as determined by surface profilometry. For this deposition we use slower withdrawal speeds (100 mm/min) and an added film soak of 5 seconds during the hydrazine cycles. We observe that this mild hydrazine treatment does not result in an n-type QD film. Gold electrodes are deposited **via** thermal evaporation of 99.999% Au at a pressure of 10^{-7} Torr and a rate of 0.2 Å/s for the first 10 nm, ramping to 2 Å/s for the final 90 nm.

4.2.4 Characterization

External quantum efficiency and current-voltage measurements are both taken in an oxygen- and water-free nitrogen glovebox with a custom-built solar simulator (Fig. 4.2) and a custom-built EQE apparatus (Fig. 4.3), both described in [67].

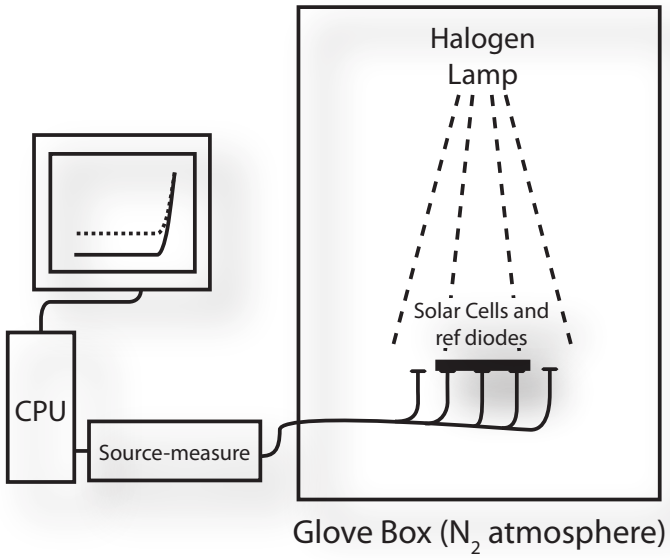

Figure 4.2: Diagram of current-voltage measurement under one-sun simulation.

The current-voltage measurement is taken under a halogen lamp, powered to closely simulate one-sum AM1.5G conditions. The test cell is place in a sample holder with multiplexed pins to allow measurement of all six devices on a chip in one sitting. There are eight pins, one contacting each of the six metal electrodes, and two on each end of the ITO

electrode. The ITO pins can be shorted together, or separated in a "three-point probe" configuration – where one of the pins sources current, while the other measures voltage. This allows us to remove the series resistance of the section of ITO **between** the ITO pins and the actual solar cell, much like how contact resistance is removed in the classical four-point probe configuration. There are also two calibrated Hamamatsu photodiodes on each side of the solar cell, permanently mounted, to measure the illumination intensity during measurement. This allows us to both control the illumination to be very close to one sun, and it also allows us to correct for any minor fluctuations or deviations from 100 mW/cm^2.

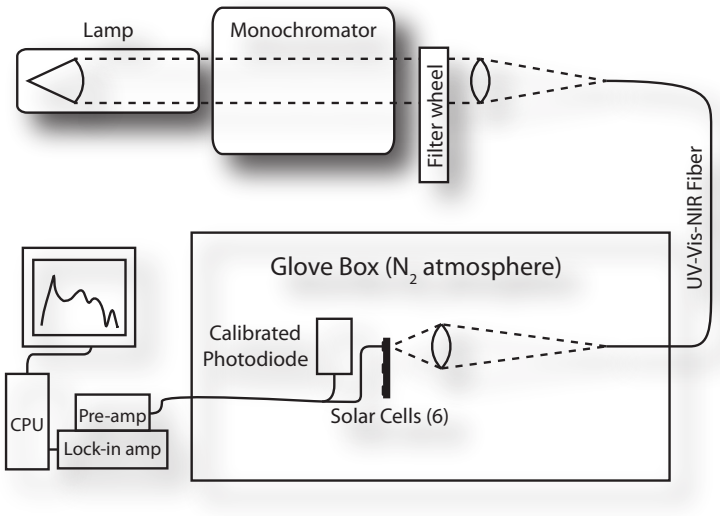

Figure 4.3: Diagram of external quantum efficiency measurement.

External quantum efficiency is measured by illuminating with monochromatic light and comparing the current generated by the test solar cell to that generated by calibrated photodiodes (which have a known EQE). The incident light comes from white light passed through a monochromator, where typically a 75W Xe arc lamp is used as the source, except for the UV-optimized arrangement, which uses a 100W Hg arc lamp. We use a Si photodiode for the 300-1060 nm range and a Ge photodiode for 1060-1750 nm. For the UV-optimized arrangement, we use a Newport UV-818-L with a calibration uncertainty of 1% (one standard deviation = 0.5%). The photodiodes all have NIST traceable calibration, and are all larger

in area than the test solar cells. Additionally, the EQE measured on our apparatus has been compared against a Thorlabs FDS-100-CAL Si calibrated photodiode (see Fig. 4.4), which is also traceable to NIST certification. The full-spectrum arrangement has more significant error (3-5%) in the UV-spectrum due to low light, so we use the UV-optimized arrangement for this region, reducing our measurement uncertainty to below 1% (see Error Analysis, below).

To verify the accuracy of our measurement apparatus, we measured the EQE of a Thorlabs FDS-100-CAL calibrated silicon photodiode, and observed excellent agreement with the commercially provided NIST-traceable calibration (Fig. 4.4). In an effort to reduce the $\sim$3% uncertainty associated with the full-spectrum EQE determination, we then optimized our apparatus for measurement in the near ultraviolet where the EQE peaks, and applied it to three sets of PbSe QDs with bandgaps near 0.72 eV (Fig 4.14A). The best device measured had a peak EQE of 107.5 $\pm$ 0.6%, which increased to 114 $\pm$ 1% with the application of a 69 nm film of MgF_2 to act as an antireflection coating on the glass. Of the 18 devices made, all achieved EQE values over 95% and 15 exhibited EQEs greater than 100%. The measurement uncertainty ranged from $\pm$0.6% to $\pm$1% at the peak. The variations result from slightly different film thicknesses, degree of ligand removal, surface passivation, and other uncontrolled variables.

We use large 1 in^2 companion films to extract the reflectance of our patterned device stacks, as in Law **et al.** [53]. The large area companion films are made alongside the patterned substrates used for devices in a dip coater arm equipped to hold multiple substrates, ensuring that the device stacks were identical. Reflectance measurements of these films were performed in air with an integrating sphere in a Shimadzu UV-Vis-NIR-3600 spectrophotometer.

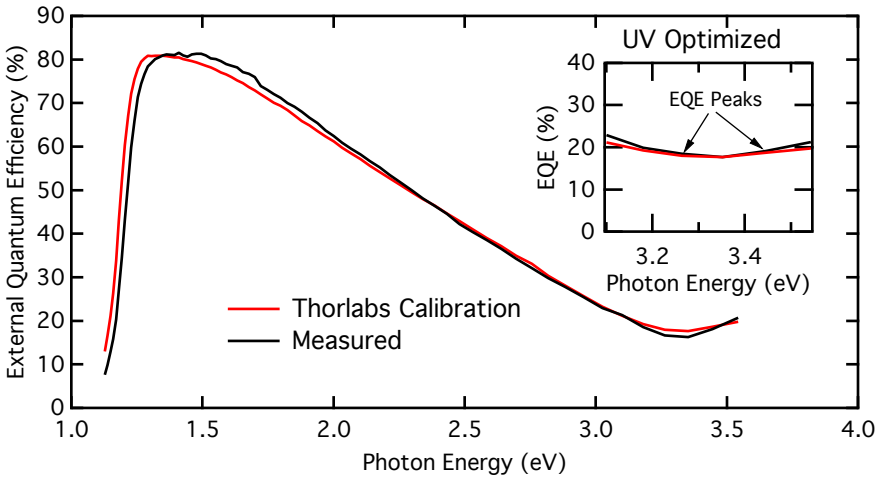

Figure 4.4: Measurement of the Thorlabs FDS-100-CAL Si photodiode (calibrated by Thorlabs Nov 24, 2010) with our EQE system in an oxygen-free nitrogen glovebox atmosphere. Here we compare the given EQE for the device with serial #10112425 against our measurement, showing excellent agreement for photon energies greater than 1.3 eV. Both the full-spectrum measurement and the UV-optimized arrangement (inset) are within 3% of the FDS-100-CAL calibration, less than the quoted calibration uncertainty of ±5%. Much of the disagreement here is likely due to the Thorlabs calibration uncertainty rather than a measurement error. Our greatest disagreement (about 5%) with the Thorlabs calibration is at a much lower photon energy than the regime in which we report an EQE > 100%. This occurs near the band edge, where we expect temperature fluctuations to affect the bandgap, and therefore the EQE. It is also possible that the spectral width of our monochromatic light could affect the EQE in this region.

4.2.5 Ellipsometry

The complex refractive index $N(h\nu) = n(h\nu) + ik(h\nu)$ spectra for the PbSe QD films, ITO, ZnO, and gold were determined by spectroscopic ellipsometry: in air for ITO, ZnO, and gold and both in air and under vacuum for the PbSe QD layers. In air, the ellipsometric data were obtained by a rotating compensator-type variable-angle spectroscopic ellipsometer (M-2000 DI model, J.A. Woollam Co., Inc.) at various incident angles ranging from 55° to 75° with an increment of 5°. Transmittance measurements were also performed in a normal-incidence configuration, whose results were combined with ellipsometric data in the modeling procedures to improve the accuracy of analysis. We note that in this configuration some oxidation of the PbSe QD layers does occur, although the complex index of refraction and the reflectance are both stable for at least several minutes, longer than the measurement time (see Fig. 4.5). Also, the effects of this oxidation on the absorption into the active layer are generally limited to the sub-1.5 eV region of the spectrum, chiefly near the lowest energy exciton.

In order to address the oxidation effects of the PbSe QD films, which can lead to problems in the optical modeling below 1 eV, we also obtain ellipsometric data under vacuum such that we can reduce air exposure effects. This approach uses a fixed-angle spectroscopic ellipsometer at 70°. The ellipsometric measurement in this mode shows less oxidation (as evidenced by improved optical modeling results), although there is some brief air-exposure during loading of the sample into the vacuum chamber.

A multilayer model was employed to analyze the ellipsometric data, which consists of glass substrate/film of interest/surface roughness/ambient. The $N(h\nu)$ of QD films was constructed by a set of oscillators such as Gaussian, Lorentzian, and Tauc-Lorentzian. The surface roughness (represented by Bruggeman effective medium approximation) and the film thickness estimated by ellipsometric measurements are in an excellent agreement with the results from surface profiling measurements. The complete ellipsometric modeling process

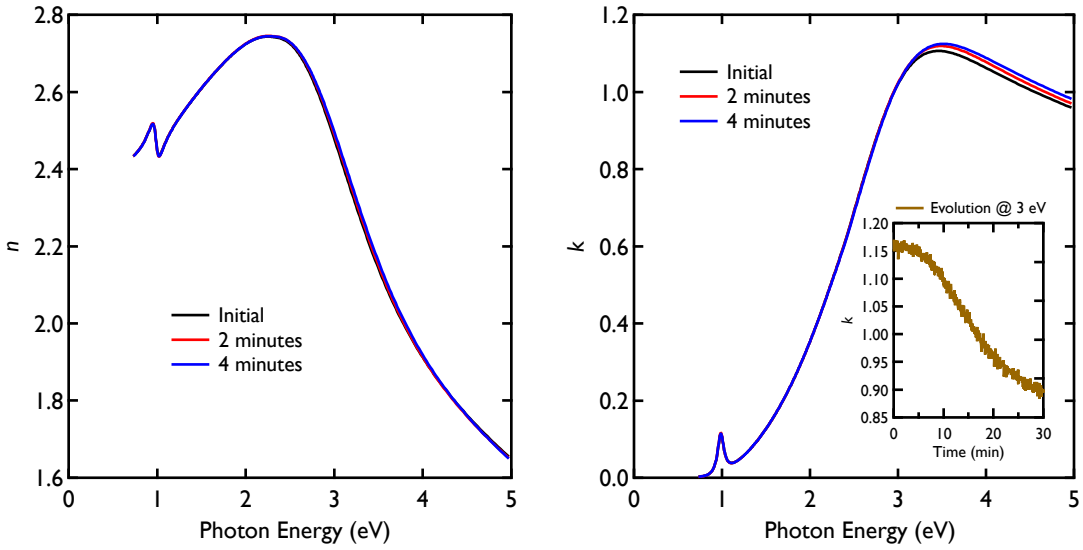

Figure 4.5: Effect of brief air exposure on the n and k of a film of 0.98 eV PbSe QDs deposited with 25 cycles of EDT and 5 cycles of hydrazine. We plot n on the left and k on the right at zero minutes (black), two minutes (red), and four minutes (blue). We also show in the inset the time evolution of k at 3 eV over a longer period of time, indicating that there is virtually no change in the first five minutes, followed by larger shifts from 10-30 minutes.

is detailed in ref. [16]. The resulting $n(h\nu)$ and $k(h\nu)$ are then used to parameterize the optical model of the device. We have plotted in Fig. 4.12 the $n(h\nu)$ and $k(h\nu)$ used for the layers modeled in fig. 4.11.

4.2.6 Optical Modeling

Both the reflectance and EQE spectra exhibit significant interference fringes indicating the buildup of optical modes within the dielectric stack. These fringes depend upon the thickness of each layer so an optical model using the ellipsometric measurements described above is employed to extract the IQE. This model is detailed in ref. [53]. The thickness of each layer was determined by cross-sectional SEM and then allowed to vary by $\sim 10\%$ in the model by a least-squares fit to the measured reflectance.

4.3 Analysis

4.3.1 Error Estimate

The quoted peak EQE values incorporate a number of sources of error, which are relatively straightforward to summarize by looking at the EQE calculation itself:

$$EQE_T = \frac{I_T}{I_R} EQE_R, \tag{4.1}$$

where I_T is the current generated by the test cell, I_R is the current generated by the reference cell, and EQE_R is the known EQE of the reference cell (calculated from the calibration in A/W). From this equation we can see that there are only three possible sources of error (I_T, I_R and EQE_R). There are fluctuations in the intensity of the lamp source, electrical noise, and drift by the chopper wheel, all of which will lead to fluctuations in the output current (I_T, I_R). We obtain an estimate of all these by measuring the output current 5-30 times and calculating a standard deviation of the mean. The third source of error, EQE_R, has a calibration uncertainty of $\pm 3\%$ for the full-spectrum EQE measurements presented in Fig.

4.11, while for the UV-optimized arrangement it is ±0.5%. Since the output current errors are typically < 0.1%, this mostly determines our uncertainty (one standard deviation):

$$\sigma_{EQE_T} = EQE_T \sqrt{\left(\frac{\sigma_{I_T}}{I_T}\right) + \left(\frac{\sigma_{I_R}}{I_R}\right) + \left(\frac{\sigma_{EQE_R}}{EQE_R}\right)}. \tag{4.2}$$

4.3.2 Multiplication Model

The fits used in Fig. 3C implement the same general function derived by Beard **et al.** [8] and is defined below. This model uses two degrees of freedom: the MEG efficiency, η_{MEG}, and s, which determines the increase in the multiplication rate with excess energy. The MEG efficiency defines the threshold energy E_{th} as

$$E_{th} = E_g + \frac{E_g}{\eta_{MEG}}, \tag{4.3}$$

where Eg is the bandgap of the QD. The model then has the functional form

$$QE = 1 + \frac{Px^s(1 + 2Pz^s)}{(1 + Px^s)(1 + Pz^s)}, \tag{4.4}$$

where P describes the competition between the multiplication and cooling rates. We relate η_{MEG} to P by $\eta_{MEG} = P/(1 + P)$, and x and z are defined as

$$x = \begin{cases} (h\nu - E_{th})/E_{th} & \text{if } h\nu \geq E_{th} \\ 0 & \text{otherwise} \end{cases}, \tag{4.5}$$

and

$$z = \begin{cases} (h\nu - 2E_{th})/E_{th} & \text{if } h\nu \geq 2E_{th} \\ 0 & \text{otherwise} \end{cases}, \tag{4.6}$$

where $h\nu$ is the photon energy. When fitted to spectroscopic data [8], this model yields $\eta_{MEG} = 0.60$ and $s = 2.2$, and the black curve in Fig. 4.14C is the calculated quantum yield from these fitting parameters. In this work we modify the model by multiplying the calculated quantum yield in eq. 4 by the mean of the peak IQE values for the two below-threshold devices, yielding the dashed black curves in Figs. 4.11A and 4.11B (they are

identical). This normalization value is 0.86, and is the same value we divide by to convert the measured peak IQE values (blue circles in Fig. 4.11b) into the normalized peak IQE values (purple circles). Finally, by allowing the normalization factor, N, to float, we apply a least-squares linear fit of eq. 4 multiplied by N to the IQE of the 0.72 eV solar cell, allowing N, η_{MEG}, and s to float, and find $N = 0.848 \pm 0.007$, $\eta_{MEG} = 0.62 \pm 0.01$, and $s = 2.8 \pm 0.3$, showing reasonable agreement with the fit to the spectroscopic data.

4.4 An MEG solar cell

4.4.1 Current-voltage characterization

Figure 4.6 compares the current-voltage characterization of typical QD solar cells prepared using the EDT/hydrazine treatment to EDT-only prepared devices. For all QD sizes tested, using hydrazine yields a dramatic improvement in all of the performance parameters (open circuit voltage, short circuit current, fill factor, series resistance and shunt resistance). We also note the elimination of the crossover between the light and dark currents in forward bias (Fig. 4.6A), indicating an ohmic anode contact [30]. Previous work [115] on ZnO/PbSe heterojunctions has shown that the valence band maximum is pinned to sub-bandgap-states in the ZnO, regardless of QD size, and that electron injection into the ZnO should be blocked for PbSe QDs with bandgaps less than approximately 0.7 eV. This finding agrees with our work — solar cells made from a batch of QDs with a smaller bandgap show a much lower V_{oc}, which limits our ability to explore smaller bandgaps. See Fig. 4.7 for a comparison of open-circuit voltage dependence on bandgap for EDT-only and EDT+hy treated solar cells.

A typical solar simulator will always have some degree of spectral mismatch to the solar spectrum. Therefore, in order to properly compare solar cell efficiencies across laboratories and over time, it is important to calibrate for this using a "spectral mismatch factor" [97]. The mismatch factor, M, is calculated by

$$M = \frac{\int_{\lambda_1}^{\lambda_2} E_{Ref}(\lambda) S_R \, d\lambda \int_{\lambda_1}^{\lambda_2} E_S(\lambda) S_T \, d\lambda}{\int_{\lambda_1}^{\lambda_2} E_{Ref}(\lambda) S_T \, d\lambda \int_{\lambda_1}^{\lambda_2} E_S(\lambda) S_R \, d\lambda} \tag{4.7}$$

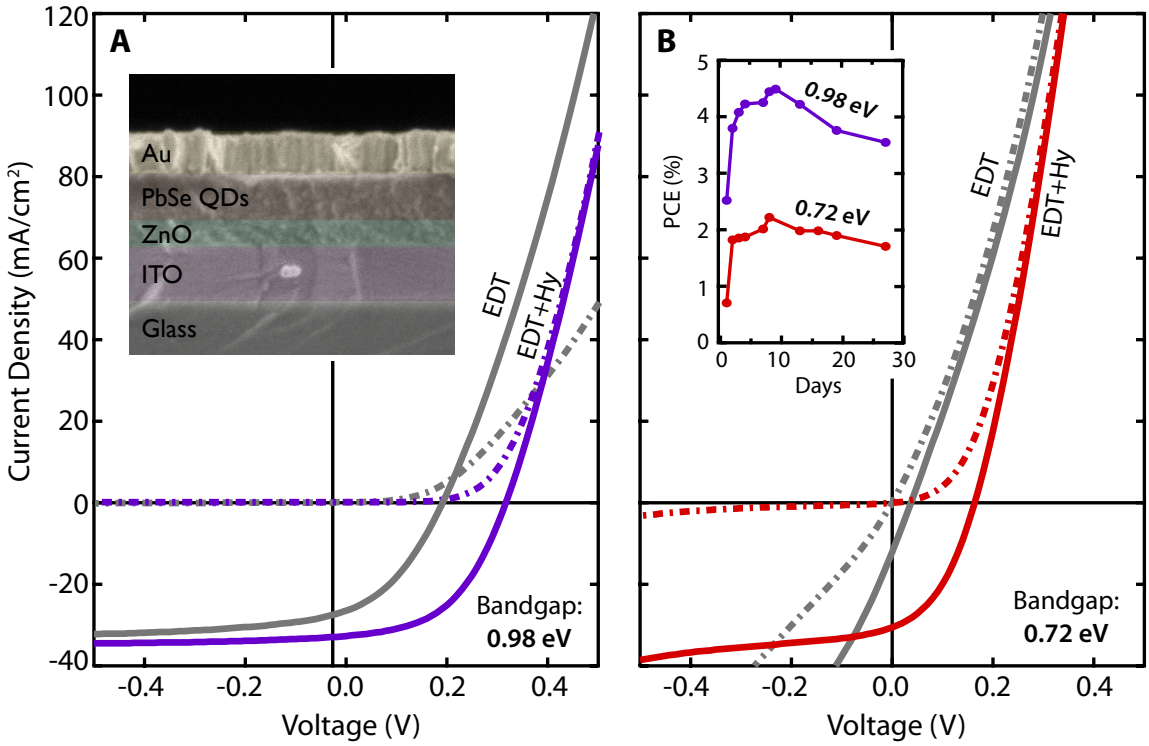

Figure 4.6: Comparison of current-voltage characteristics under simulated AM1.5G illumination of devices assembled from EDT and EDT+hydrazine treated (A) small 0.98 eV QD films and (B) large 0.72 eV QD films. Solid lines correspond to 100 mW cm^{-2} illumination, dot-dashed lines to dark conditions, purple to small QDs with EDT+hydrazine, red to large QDs with EDT+hydrazine, and grey to the respective QDs with EDT-only treatment. The upper inset to A displays a false-color cross-sectional SEM of a typical device. The inset to B shows the effect of aging (25 days under N_2) on mismatch-corrected power conversion efficiency (PCE).

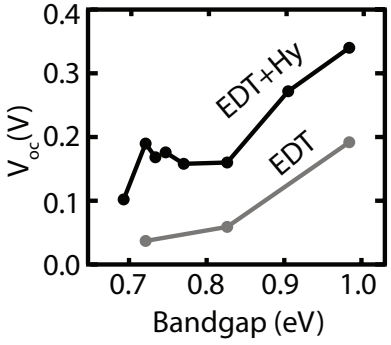

Figure 4.7: Comparison of EDT-only versus EDT+hydrazine treatment on open circuit voltage (V_{oc}) for a range of QD bandgaps.

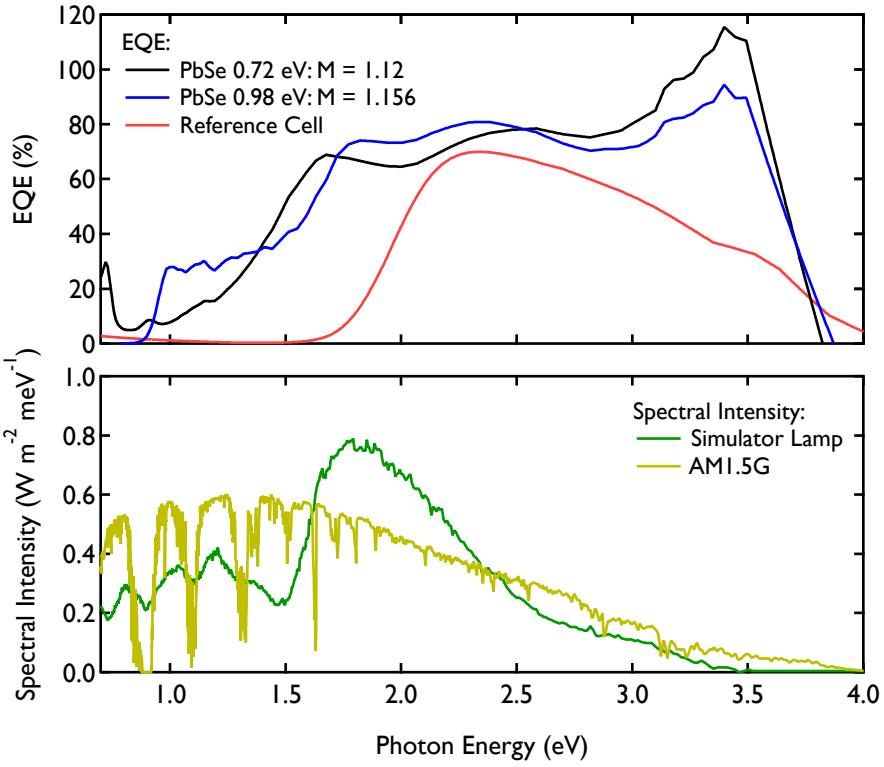

Figure 4.8: Spectral mismatch correction factor for the power conversion efficiency characterization of the two devices shown in Fig. 4.14.

where E_{Ref} is the spectral intensity of the sun, E_S is the spectral intensity of the solar simulator lamp, S_R is the spectral responsivity of the reference photodiode used to control for intensity, and S_T is the spectral responsivity of the test cell. The uncorrected power conversion efficiency ($\eta^{(0)}$) and short circuit current ($J_{sc}^{(0)}$) can be corrected to their true 1-sun values ($\eta^{(1)}$ and $J_{sc}^{(1)}$) by dividing by M:

$$\eta^{(1)} = \eta^{(0)}/M, J_{sc}^{(1)} = J_{sc}^{(0)}/M. \tag{4.8}$$

See ref. [97] for a complete discussion of mismatch factors and their calculation. The integrated photocurrents (which agree with the 1-sun J_{sc} values to within 7%) and mismatch factors for the devices are shown below in Table 4.1.

Table 4.1: Compiled mismatch calculation values.

QD Bandgap	Lamp J_{sc} (mA cm^{-2})	AM1.5G J_{sc} (mA cm^{-2})	Mismatch, M
0.72 eV	28.5	25.8	1.12
0.98 eV	30.3	26.6	1.16

We observed a beneficial aging effect on the solar cell performance under oxygen- and water-free nitrogen storage conditions, and thus our EQE data were collected after the initial rise in performance. This aging could be related to desorption of hydrazine over time reported for hydrazine-treated PbSe films [111, 120]. The inset to Fig. 4.6B shows the mismatch-corrected power conversion efficiency (PCE) as a function of the device age, with a best PCE of 4.5% for the 0.98 eV device after eight days. Previous reports for QD solar cells have reached 4.5% using larger bandgap PbSe QDs, and 6% using PbS QDs (27, 28). We have found that our hydrazine treatment technique is effective with both PbSe and PbS QDs and also works with other molecules such as formic acid, 3-mercaptopropionic acid, methylamine, and ethanol. For the MEG studies, the hydrazine-treated devices allowed for the use of larger QD sizes with smaller bandgaps facilitating the ability to study high-energy photons relative to the bandgap. Additionally, the ZnO/PbSe interface produces an $n-p$ heterojunction that

facilitates extraction of charge carriers produced from high-energy photons (those capable of undergoing MEG), which are mostly absorbed in the first 50 nm of the PbSe film (see Fig. 4.10).

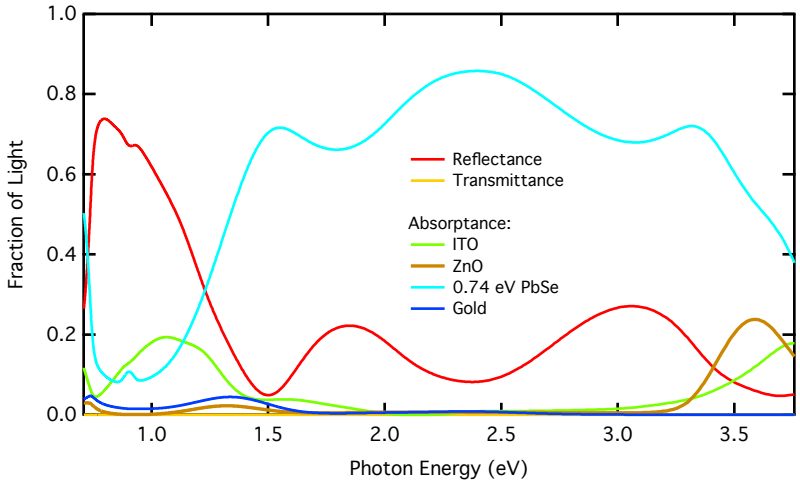

Figure 4.9: Sample output from the optical model for the 0.72 eV device from Figs. 4.11 and 4.14. Note that the ITO has significant absorption above 3 eV and below 1.5 eV (absorbing even more than the PbSe QD layer in the latter range). The complex refractive index spectra used in this modeling is shown in Fig. 4.12.

4.4.2 External and internal quantum efficiency characterization

Figure 4.11 displays full-spectrum EQE (red) and reflection (brown) profiles for three typical devices, with QD size-dependent bandgaps (E_g) of 0.98 eV (Fig. 4.11A, 4.11B), 0.83 eV (Fig. 4.11C, 4.11D) and 0.72 eV (Fig. 4.11E, 4.11F). At the lowest photon energies ($h\nu$) the first exciton absorption peak is clearly visible, and optical mode buildup is responsible for the observed oscillations at higher photon energies. Despite reflection and absorption by the glass, ITO, and ZnO layers prior to the incident light reaching the QD layer, the device with the largest sized QDs ($E_g = 0.72$ eV) exhibited an EQE of $106 \pm 3\%$ at 3.44 eV photon energy ($\lambda = 360$ nm, Fig. 4.11E). We determined the IQE from the EQE in two ways. First, because all photons not absorbed within the solar cell are reflected, to first order the IQE is equal to the EQE divided by $[1 - R(h\nu)]$, where $R(h\nu)$ (Fig. 4.11, brown) is the

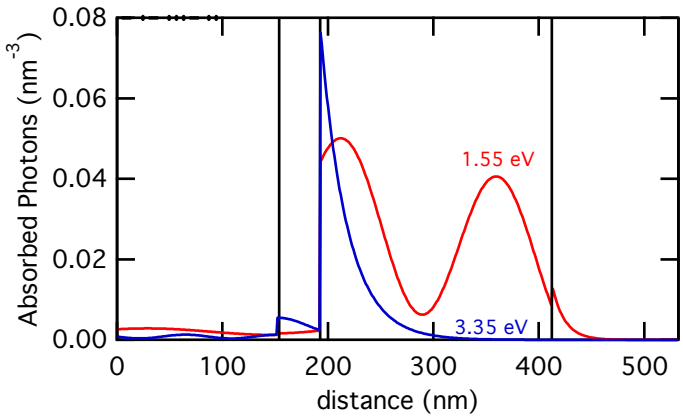

Figure 4.10: Depth-dependent optical generation profile at 3.35 eV and 1.55 eV photon energies for the same 0.72 eV device in Fig. 4.11E and 4.11F. These curves are produced by the optical model discussed above and detailed in ref. [53] – integrating along the depth (z axis) gives the total light absorbed by that section of the stack at a given wavelength, yielding the curves shown in Fig. 4.9.

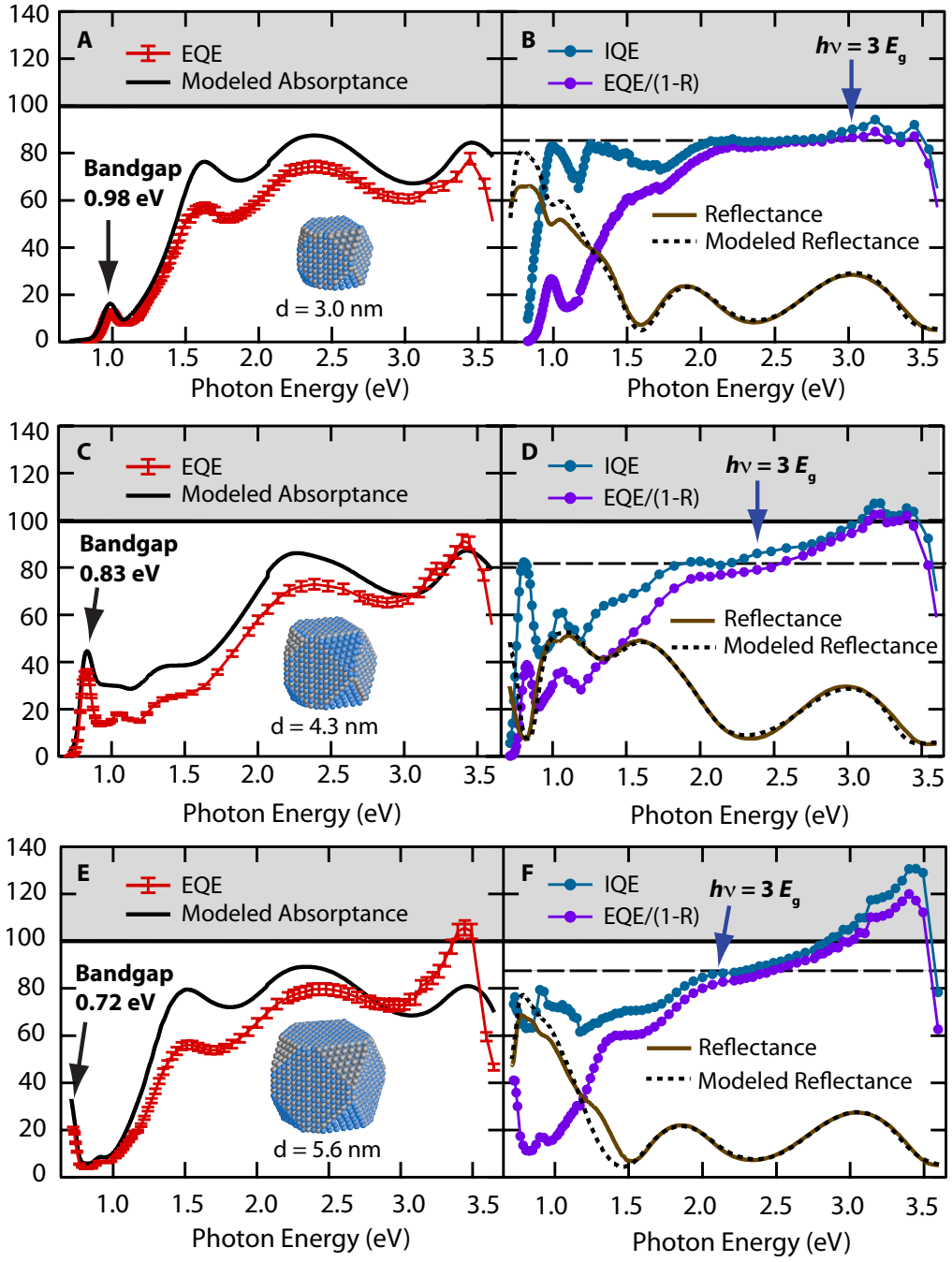

Figure 4.11: Red curves are the measured EQE for three representative quantum dot solar cells made from PbSe QDs with indicated diameters and associated bandgaps of **(A, B)** 0.98 eV, **(C, D)** 0.83 eV, and **(E, F)** 0.72 eV. We estimate the uncertainty of these EQE curves to be ∼3% (see SOM text for details). We plot the modeled absorptance of the QD plus ZnO layers (A, C, E, solid black, see Fig. 4.9 for all layers) and measured reflectance (B, D, F, brown). The IQE is determined either by $EQE/(1-R)$ (purple curves) or by EQE/A (blue curves), where A is the modeled absorptance of the PbSe plus ZnO layers. The modeled reflectance is shown as the dashed black line. For each data set the IQE begins to rise significantly at a photon energy of about 3 times the bandgap, E_g, peaking higher for decreasing E_g.

reflectance at a photon energy of $h\nu$ (measured using an integrating sphere to include diffuse reflectance). The $EQE/(1-R)$ ratio (Fig. 4.11, purple) represents the lower limit to the IQE, as it is not corrected for light absorbed by other layers that do not contribute to the photocurrent. For example, the $EQE/(1-R)$ ratio decreases for photon energies less than 2 eV because of ITO absorption in that near infrared spectral region. Therefore, to account for such losses we used a second approach. We determined the absorptance and reflectance of each layer by applying an optical model [53] with complex refractive indices ($N = n + ik$) determined by ellipsometry for each component layer (see SOM text for ellipsometry and modeling details, and Fig. 4.12 for plotted refractive indices). The thicknesses used in the optical model for the three devices in Fig. 4.11 are listed below in Table 4.2.

Table 4.2: Table of device thicknesses used for modeling shown in Fig. 4.11. The row labeled "dip cycles" indicates the number of EDT+hy layers used in the LbL QD film deposition.

	Thicknesses by E_g (nm)		
Layer	0.98 eV	0.83 eV	0.72 eV
ITO	143	135	158
ZnO	55	70	34
PbSe QDs (*dip cycles*)	236 (20+5)	116 (10+5)	228 (20+5)
Au	100	100	120

In the UV-visible spectral region of most interest, the modeled reflectance (Fig. 4.11, dashed black) and the measured reflectance (brown) agree very well and are fairly insensitive to QD and ZnO layer thicknesses because in this region the photons are all absorbed within 50 to 100 nm of the ZnO/QD interface. We show how the IQE and calculated R vary in Fig. 4.13 for different layer thicknesses. The IQE is determined by normalizing the EQE to the calculated absorptance (eq. 4.9):

$$\mathrm{IQE} = \frac{\mathrm{EQE}}{A}, \tag{4.9}$$

where we include both the absorptance of the ZnO and PbSe layers $A = A_{PbSe} + A_{ZnO}$. The IQE differs from $EQE/(1-R)$ only slightly in the UV-visible region, but more significantly

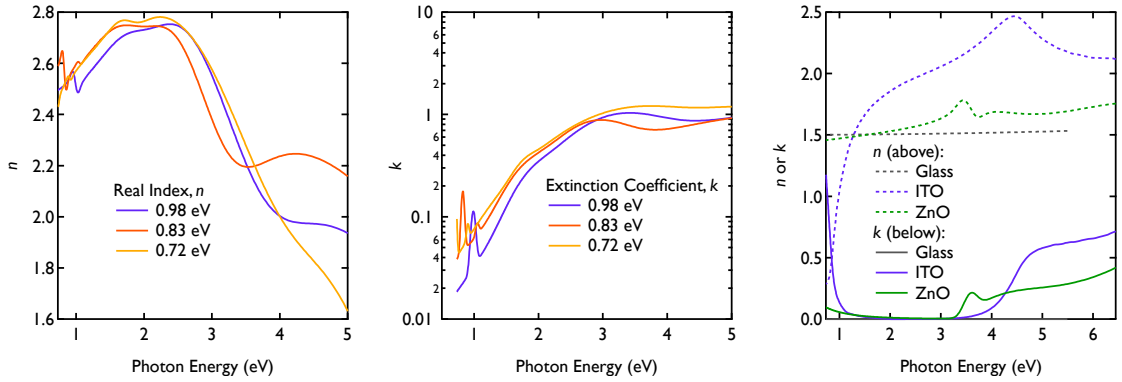

Figure 4.12: Typical complex refractive index spectra of the Glass, ITO, ZnO, PbSe QD, and Au layers measured and used in this work. The first two panels show the n and k values used for modeling of the devices in Figs. 4.11 and 4.14B.

in the longer wavelength region (where absorption by ITO does not yield photocurrent). The IQE curves exhibit short-circuit collection yields of around 85%, until the photon energy surpasses the MEG threshold, after which the IQE rises to a peak efficiency of 130% in the 0.72 eV QDs, 108% in the 0.83 eV QDs, and 98% in the 0.98 eV QDs. The glass, ITO and ZnO begin to absorb significant quantities of light at photon energies greater than 3.5 eV, and the EQE and IQE drop sharply. Enhanced interfacial of carriers at these high photon energies may also contribute to the drops in EQE and IQE, as is typical in conventional solar cells.

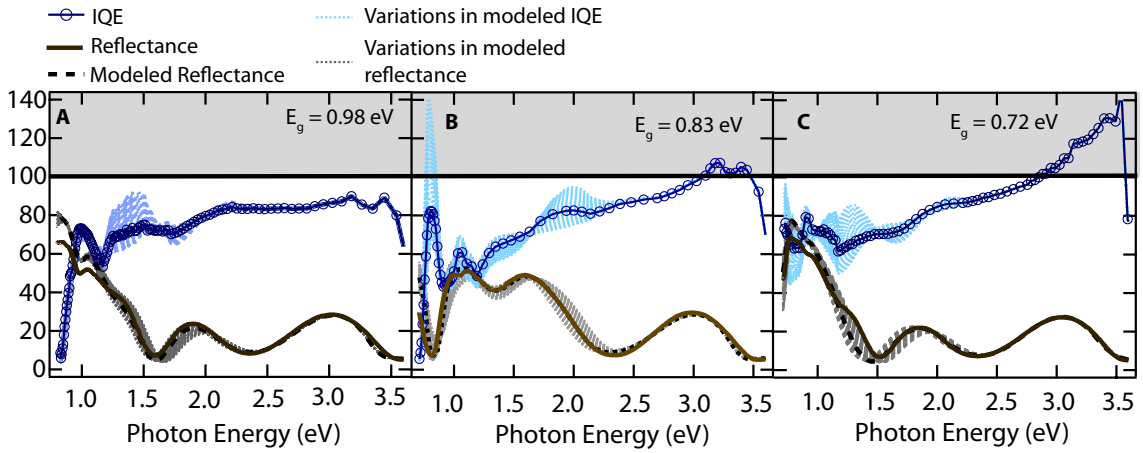

Figure 4.13: Effect of varying the thickness of the PbSe QD layer in the optical model on modeled reflectance and calculated IQE. We allow the thickness to vary in increments of 1 nm and plot the resulting IQE curves. We find that below 2 eV, and especially near the first optical transition, the variation is much greater, while above 2.5 eV there is virtually no change.

There are several reports of IQE greater than 100% and one report of an EQE greater than 100% based on impact ionization in bulk semiconductor devices. Canfield et al. [13] reported an EQE of 128% at a photon energy of 7.7 eV in a bulk silicon photodiode, corresponding to a relative photon energy of $7E_g$. For bulk silicon-based solar cells, the photon energy threshold for carrier multiplication occurs around 3.9 eV, or $3.5E_g$ [13], and at 2.8 eV, or $4.1E_g$, in germanium [125]. Here the onset for the 0.72 eV bandgap QDs is ~2 eV or ~2.8 E_g.

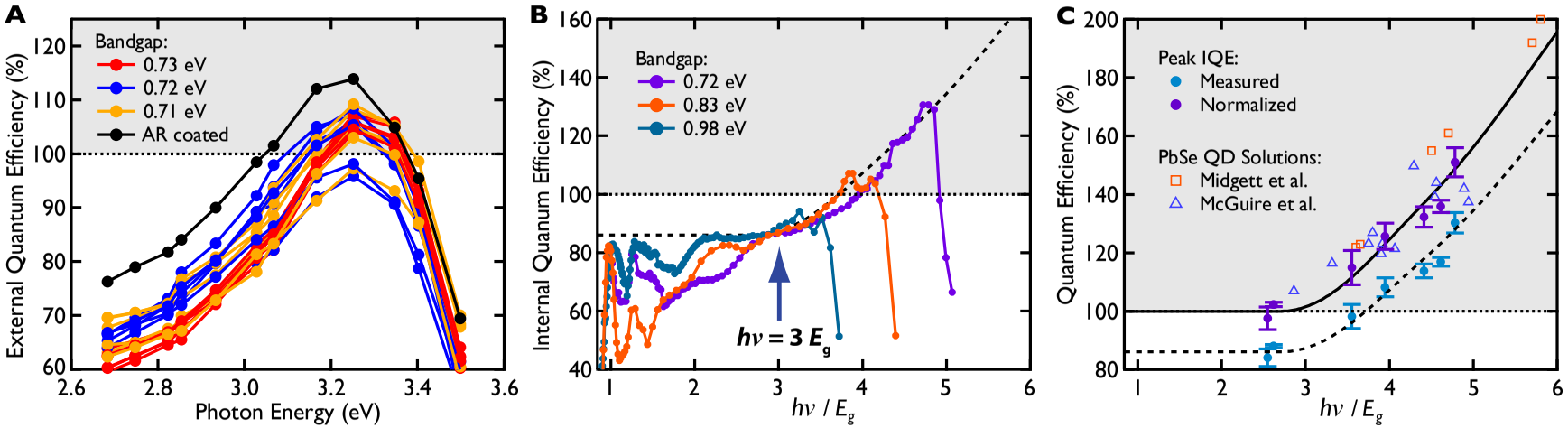

Figure 4.14: **(A)** EQE peaks for 18 independent devices made with QDs bandgaps of 0.71 eV (yellow), 0.72 eV (blue), and 0.73 eV (red); as well as a device with an antireflective coating (black). **(B)** Collected IQE curves versus the ratio of photon energy to bandgap, $h\nu/E_g$, for the three QD sizes in Fig. 4.11. The dashed curve is a previously published fit for colloidal QDs using the model described in ref. [8], where here it has been normalized for intrinsic losses in the cell due to recombination. **(C)** Peak IQE values from seven different QD sizes. We plot the peak IQE values corrected for intrinsic losses in the solar cell (estimated at ∼15%). Error bars are the propagated uncertainty of 5 to 30 measurements at the given wavelength of both the reference detector and the test solar cell. The solid black curve is the original fit to colloidal QDs from ref. [8], whereas the dashed curve is the same as in (B). The hollow triangles and squares represent ultrafast transient absorption measurements of PbSe QD solutions taken from ref. [69] and ref. [71], respectively.

To further assess the MEG efficiency, η_{MEG} [8], in Fig. 4.14B we plot the IQE curves from Fig. 4.11 versus $h\nu/E_g$ (the photon energy normalized to the bandgap of the QD). Some researchers suggest [78] that in order to assess the fundamental photophysics of the MEG process, the quantum efficiency should be plotted on an absolute photon energy basis (see Fig. 4.15 for a plot on the absolute photon energy basis). However, we argue [8] that the $h\nu/E_g$ basis is more appropriate for understanding the fundamental competition between hot-carrier cooling and the MEG relaxation channel, as well as the practical utility for solar energy conversion. The slope of such plots is also proportional to the number of additional excitons created per bandgap of photoexcitation. Regarding this issue, we find it notable that the IQE curves for different sized QDs are so similar on the $h\nu/E_g$ basis, indicating that the ability to convert high-energy photons to multiple excitons is mainly determined by the excess energy relative to the threshold energy required to create an exciton.

We compare photocurrent results to spectroscopic results reported in prior literature in Fig. 4.14C. We find a clear trend in peak IQE values (blue circles) that agrees well with spectroscopic measurements (hollow triangles and squares), despite a difference of about 15% due to intrinsic photocurrent losses. The IQE of the two devices using large bandgap QDs (1.35 eV and 1.48 eV) exhibit peak quantum efficiencies consistent with the 85% plateau for photon energies below the MEG-threshold and thus we estimate the intrinsic photocurrent losses at $\sim$15%. We attribute these losses to electron-hole recombination before carrier separation and collection as photocurrent, and therefore normalize the measured IQE to these values, yielding the purple circles in Fig. 4.14C. These values compare well with a model [8] that accounts for a competition between MEG and hot-exciton cooling (Fig. 4.14C, solid black curve, dashed curve normalized as above). Finally, we apply a least-squares linear fit of a normalized version of the same model to the IQE for the 0.72 eV solar cell in Fig. 4.14B, yielding $\eta_{MEG} = 0.62 \pm 0.1$, and an MEG onset threshold, E_{th} (eq. 4.10),

$$E_{th} = \left(1 + \frac{1}{\eta_{MEG}}\right) E_g = (2.61 \pm 0.03) E_g, \tag{4.10}$$

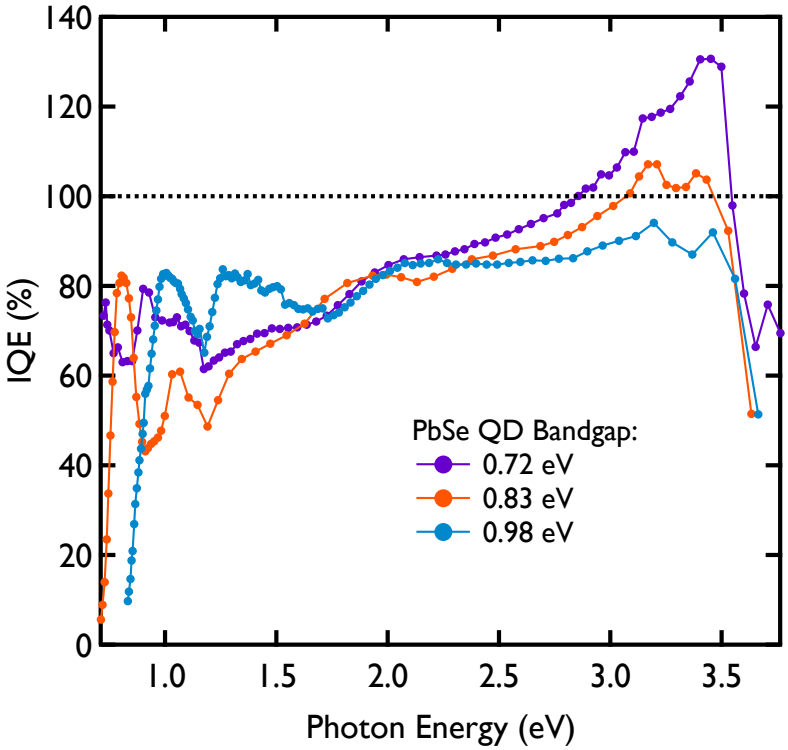

Figure 4.15: IQE plotted against photon energy, $h\nu$, for all of the devices shown in Fig. 4.14B. Note the increasing heights and red-shift of the MEG onset with decreasing bandgap.

indicating quantitative agreement with spectroscopic measurements. We believe this result constitutes incontrovertible evidence that MEG is more efficient in PbSe QDs than in bulk PbSe, which exhibits an MEG efficiency of only 0.31 and a corresponding onset of $4.22E_g$ [8, 89]. In order to estimate the impact of MEG on the PCE, we integrate the 0.72 eV device IQE in excess of the baseline 85% (Fig. 4.16, shaded region) against the AM1.5G solar spectrum. We estimate that $\sim$1 mA cm^{-2}, or $\sim$4%, of the total photocurrent arises from MEG, consistent with previous estimates based on TAS measurements of MEG in colloidal QDs [8]. Bulk Si PV cells could only benefit by <1% from impact ionization, and $Si_{1-x}Ge_x$ alloys could benefit by at most 2% [125].

4.5 Conclusions

The useful effects of our hydrazine treatment allow multiple carriers produced by MEG to be efficiently collected in a solar cell made from electronically coupled QDs. To have the largest impact on solar energy conversion efficiency, the MEG onset would have to be close to twice the bandgap, which could lead to a bonus photocurrent contribution as high as 30% [36, 8]. The challenge is to learn how to further improve the MEG-enhanced quantum efficiency and this will necessarily involve maximizing the MEG kinetics via chemical, dimensional, or architectural means, while also limiting the inelastic, phonon-mediated exciton cooling rates. Carbon nanotubes [28, 121] and PbSe nanorods [21] have shown promising results in this direction. Our findings are a promising first step towards breaking the single junction Shockley-Queisser limit [96] of present-day first and second generation solar cells, thus moving photovoltaic cells toward the third generation regime.

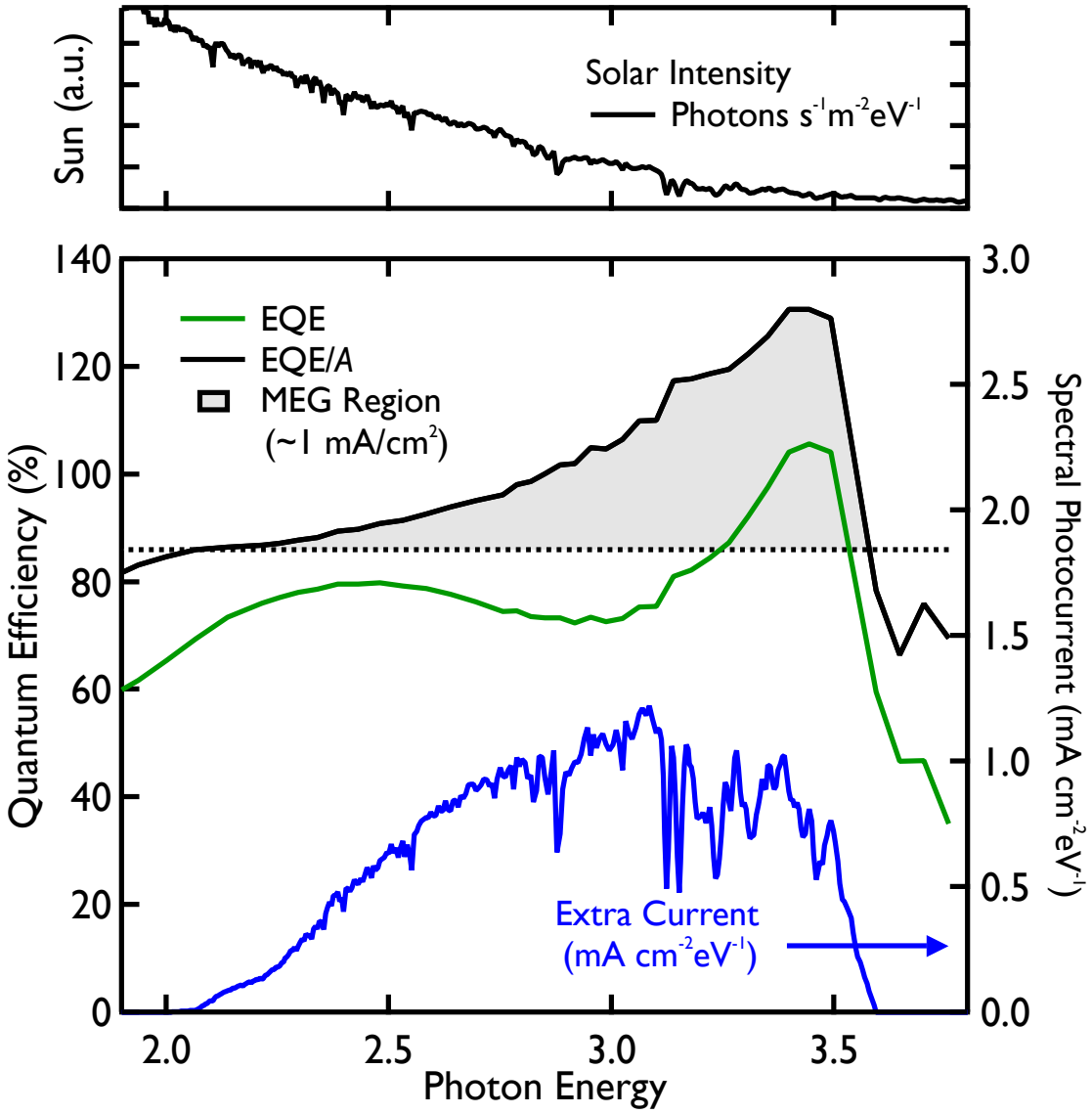

Figure 4.16: In order to make an estimate of the impact of MEG on the solar cell PCE, we multiply the IQE in excess of the baseline 85% (shaded region) by the AM1.5G solar spectrum. This gives a rough estimate of the spectral "bonus" photocurrent MEG could provide to a properly optimized solar cell (blue curve). This curve, when integrated for the smallest bandgap device, yields a bonus current of about 1 mA/cm^2, or 4%. This is a small contribution, and for larger bandgap QDs, it is even smaller, in agreement with previous estimates [8].

Chapter 5

The Secondary Treatment

A common question I am asked when presenting the MEG device from the previous chapter is, "what was the trick?" Unfortunately, no single "trick" can summarize what it took to get to this point. My work built on previous efforts, most important of which was the development of the optical model [53]. However, these only transformed a peak EQE of 60% into a peak IQE of about 80%, and no real signature of MEG. The limitations to this system have been detailed elsewhere, but simply put, the placement of the Schottky barrier at the rear of the cell, and the use of EDT-only treatment, probably limited the collection efficiency. Getting from 80% IQE to 130% IQE then was a combination of one large development, and two smaller ones.

The first small improvement was the use of a silver busbar to lower series resistance and aid collection of carriers from the cell. This probably accounted for about a 10% relative improvement. The second of the smaller factors was conversion of the device from a Schottky cell to a heterojunction cell, where the built-in field was now strongest where absorption of MEG photons was also strongest. However, this device architecture was incompatible with sub-1 eV bandgap QD PbSe [15], making it impossible to know if MEG was occurring in these films. The final, most important, development of the secondary hydrazine treatment (EDT+hy) solved that problem. EDT+hy lowered the bandgap limit to about 0.7 eV, and raised the peak EQE from 60% to over 100%. Similarly, where before an EQE of 20% at the first exciton was good, I could now easily achieve 40% EQE at the first exciton with the

EDT+hy treatment. Finally, the anti-reflection coating pushed 107% to 114% or so.

The EDT+hy treatment came about as a product of very directed, intentional experimentation, with perhaps one piece of good fortune. The basis from which I was working was films treated only with EDT. A cartoon of what we believe the film to look like after EDT-only treatment is shown in Figure 5.1. While EDT-only was known to yield decent solar cells, amine treatments [111] were known to have higher mobilities than EDT-only. Further, at the time EDT was believed to suppress MEG, while amine and alcohol treatments were believed to preserve it [9]. It has now been suggested that perhaps the transient absorption measurement used in [9] would miss the MEG signature due to reduced Auger recombination thanks to carrier mobility [1]. Regardless, because of these two results, I believed that moving to new treatments could elicit a better solar cell that would show MEG.

Therefore, I began making the ZnO heterojunction solar cell from Chapter 3, with the EDT-treatment replaced by a 1M hydrazine treatment. However, I immediately noted that these solar cells exhibited good rectification, but little-to-no current. I also noted that hydrazine could dissolve ZnO, an observation that could be seen by simple inspection of a ZnO film soaked in hydrazine. Therefore, I decided to combine the two treatments, EDT and hydrazine, such that I could protect the ZnO film, and still yield an improved solar cell. I hypothesized that if I deposited a film of QDs treated by EDT, *then* performed a LbL deposition of QDs with hydrazine, the original QD film could protect the ZnO film from the hydrazine. At the time I did not realize the hydrazine would also treat the underlying QDs, and this was a lucky break, as I will show in this chapter.

At publication in 2011, the cause of the EDT+hy improvements was not clear, and in 2012 is still somewhat in doubt. This chapter will summarize the work done to try to explain *why* the solar cells are improved with the second layer-by-layer (LbL) deposition of hydrazine-treated quantum dots. It may contain some rather speculative arguments as well.

Some of the phenomena noted in the JV curves (Fig. 4.6) suggest possible reasons for improved PV function. I will list the observations again here:

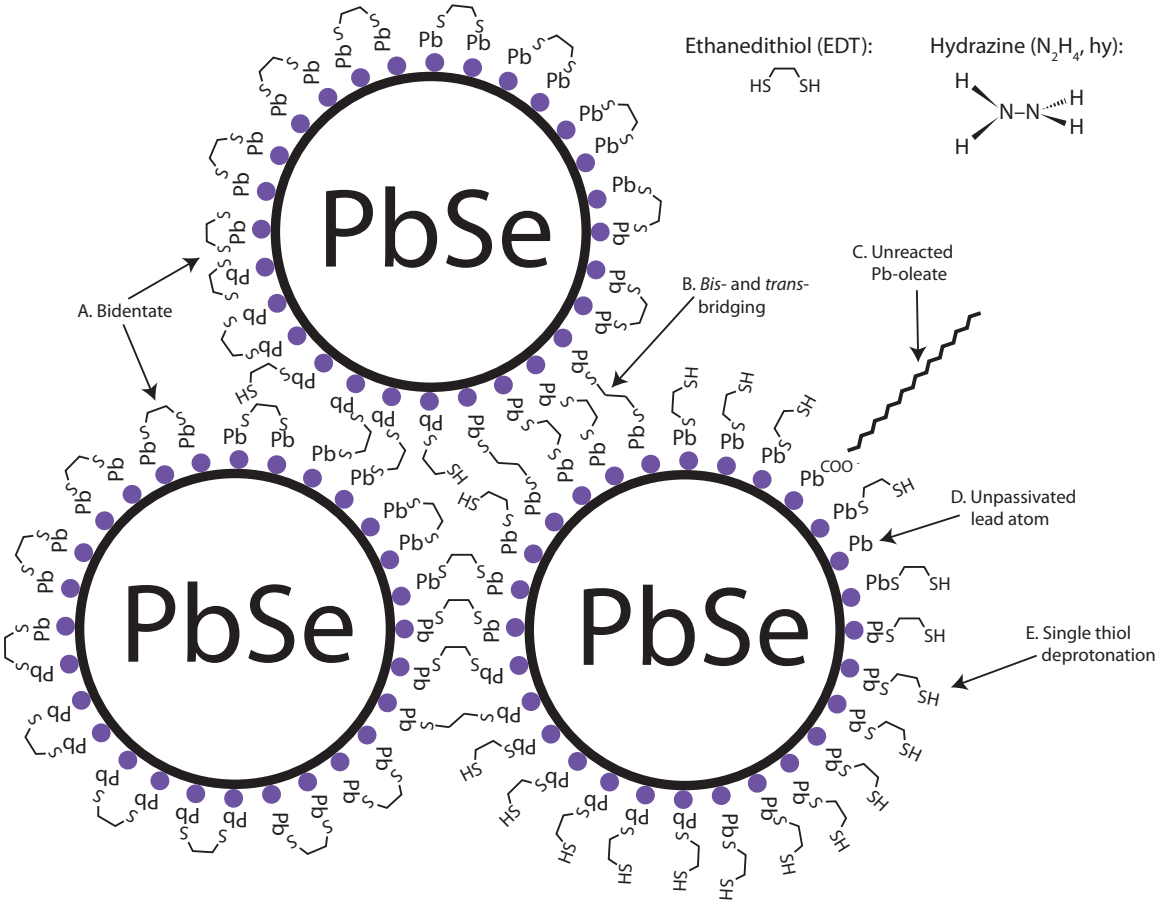

Figure 5.1: Diagram of QD film treated with EDT, including surface chemistry. Different possible surface configurations of EDT are indicated. **A.** Bidentate binding of both thiols in EDT to excess surface lead atoms. It is believed that only one negative charge (here provided by a thiol) is necessary to passivate the lead atom [73], but it is possible that both thiols (each $^{1-}$) could bind to one Pb^{2+}, as shown by the second arrow. **B.** *bis-* and *trans-* bidentate bridging is possible, where the EDT molecule spans two QDs. The thiol can have both the *bis-* and *trans-* configuration in all cases. **C.** Some of the unreacted Pb-oleate can remain after EDT-treatment (see Fig. 1.3 for a diagram of the QD before ligand exchange). **D.** Bare, unpassivated lead is also possible. In this case, the Pb is probably reduced to neutral Pb^0 metal. **E.** Single thiol deprotonation can leave the second thiol dangling and unreacted. Finally, the chemical structure of unreacted EDT and hydrazine are drawn in the upper-right corner.

(1) **Elimination of crossover**. The crossover of light and dark curves indicates that conductivity is lower in the dark at forward bias. This can be because there is a second diode opposing the primary diode in the solar cell (in this case it is a Schottky barrier at the PbSe/Au interface), which is reduced under illumination [30].

(2) **Improved fill factor and series/shunt resistance**. As discussed in Section 1.2, the fill factor is essentially defined by the shunt (R_{sh}) and series (R_s) resistances. A high R_{sh} suggests that leakage current is low, which is often thanks to lowered recombination in the QD film. Conversely, a lower series resistance indicates that the whole solar stack is more conductive, which can be due to increased mobility, more free carriers, or reduction of barriers to electrons and holes.

(3) **Increased V_{OC} and J_{SC}**. As shown in Eq. 1.29, the open circuit voltage in an ideal solar cell is highly dependent on leakage current – again, more recombination will contribute significantly to this. More directly, recombination current will also cut into the short circuit current, but typically the variation is so small as to be insignificant on the scale of J_{sc}.

(4) **Access to smaller bandgaps**. As shown in Fig. 4.6, the EDT+hy treatment allows us to make solar cells with small bandgaps, where before the EDT-only treatment would give fairly marginal results.

(5) **Access to thicker films**. In the past, solar cells were limited to less than 200 nm thick active layers [66, 53, 45, 64]. In EDT+hy devices, I have observed that the EQE can extend to 900 nm at or above 60% (see Fig. 5.2), a range still not observed in solar cells to date [44].

(6) **Robustness and stability**. This is a difficult characteristic to effectively quantify, but my intuitive experience has been that while day-to-day fluctuations in the assembly conditions of the solar cells can ruin an EDT-only device, the EDT+hy films

seem to yield many more successful devices.

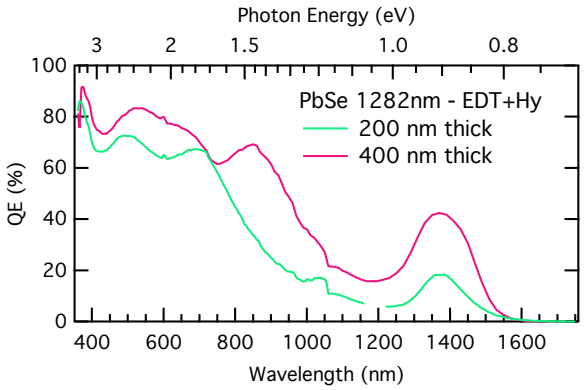

Figure 5.2: External quantum efficiency of thick PbSe QD solar cells treated with the EDT+hy prep.

All of these observations together give a fairly strong suggestion that recombination has been reduced in EDT+hy solar cells. A reduced recombination rate would account for observations 2, 3, 4, 5, and possibly 6. The mechanism of this could simply be that hydrazine is reducing undesirable oxides in the PbSe QD film, a process that would also tend to compensate for day-to-day fluctuations in water and oxygen levels in the gloveboxes (addressing observation 6). Hydrazine is known to be a very strong reducing agent. When solar cells are simply soaked in hydrazine (without concurrent LbL deposition of QDs), they show improvements from the EDT-only preparation (see Fig. 5.3. However, they are not as improved as when a LbL deposition is used with the hydrazine, suggesting additional factors are at play.

In order to look for reduction of oxides by hydrazine, we have performed x-ray photoelectron spectroscopy (XPS) and secondary ion mass spectrometry (SIMS) to look for a change in the presence of oxygen atoms with treatment by hydrazine. However, in the case of XPS, no oxygen was detected in either the control (EDT) or test (EDT+hy) cases, while SIMS was not in a glovebox coupled setup – meaning oxygen was introduced during loading of the sample. XPS can typically detect down to 0.1%, so it is possible that oxygen was

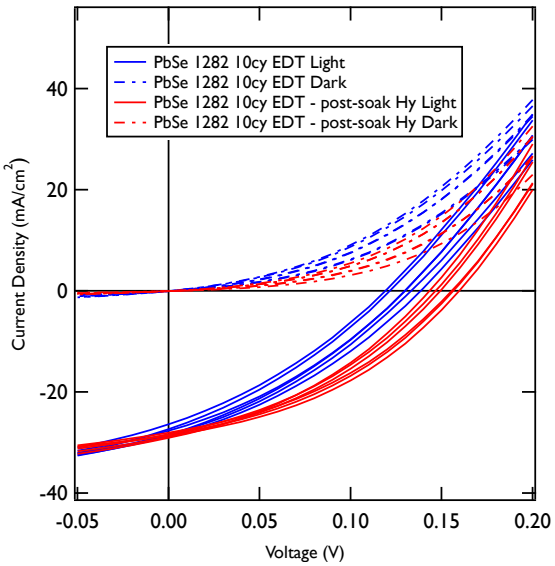

Figure 5.3: Effect of hydrazine soaking.

merely present at levels below the threshold. Our gloveboxes are typically kept at or below 1 ppm oxygen. We do however note about a 10% reduction in both the carbon and sulfur (EDT) content in films treated with hydrazine (see 5.4), suggesting that hydrazine soaking may be removing EDT ligands. This could benefit solar cells by reducing the excess anion concentration in the film, thereby reducing the doping and defect concentration in the films. We also observe an 80 meV drop in the core level binding energies, which could indicate that the Fermi level of the EDT+hy film is closer to its valence band maximum, or that the film is simply more conductive. Finally, no nitrogen was detectable in either film, suggesting that hydrazine does not bind to the surface of the QDs.

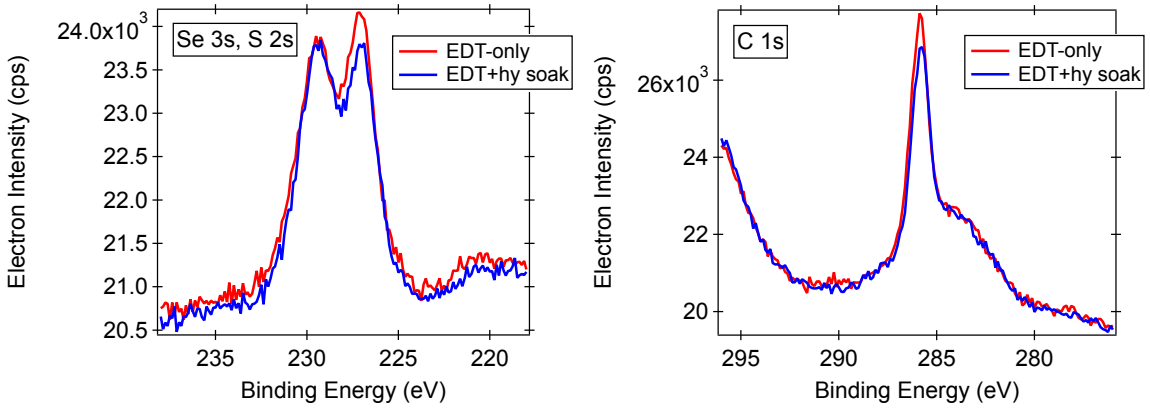

Figure 5.4: XPS of EDT-treated film followed by a 1M hydrazine soak.

The antioxidant effects of hydrazine *are* somewhat supported by ellipsometry analysis which shows that a film deposited with EDT, then soaked in hydrazine, shows a first exciton that is sharper than and red-shifted from the EDT-only first exciton (see Fig. 5.5). Oxidation has the effect of shrinking the effective QD size, and so will lead to bluer first excitons. Similarly, a narrower first exciton would suggest that while some QDs are oxidized before hydrazine, the hydrazine reduces this non-uniformity.It is unlikely that hydrazine brings the QDs closer together, because we expect that would *red*-shift and *broaden* the first exciton, contrary to Fig. 5.5. We could confirm this with some demonstrations of reproducibility and perhaps with an air-free SIMS measurement.

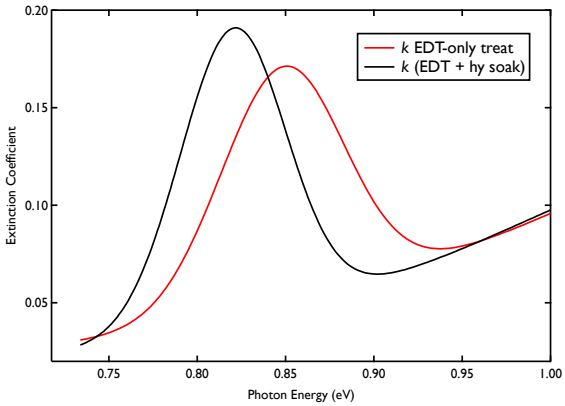

Figure 5.5: Comparison of the first exciton n and k of PbSe 1420 nm films treated with EDT-only and EDT+hy. The films were made simultaneously, with the exception than one film was soaked five times for five seconds each in 1M hydrazine.

The reduced recombination can be shown in time resolved microwave conductivity (TRMC) experiments. TRMC is a tool well-used at NREL, although it is fairly uncommon in other research labs. The measurement is like any pump-probe transient absorption experiment where pulsed lasers are used, except that the probe is absorption of microwaves. The microwave frequency and the cavity used to amplify microwaves necessarily limits the time resolution to about 1-10 nanoseconds, but I believe that the relevant time-scale is on the order 10s of ns to 10s of μs, depending on mobility. This is based on an estimate of the shortest drift transit time (τ) for a carrier moving under a built-in potential difference (ΔV) of ~ 0.5 V, thickness (t) 500 nm, and mobility (μ) between 10^{-1} and 10^{-4} cm^2/V s:

$$\tau = t/v_d = \frac{t^2}{\mu\,\Delta V}, \tag{5.1}$$

where we have used the relation for drift velocity $v_d = \mu E$. Perhaps with mobilities better than 1 cm^2/V s this assumption could be challenged, but as yet no solar cell with such a high mobility has been shown. Indeed, PbS devices typically have mobilities on the low end of my estimate, while PbSe films are now approaching 1 cm^2/V s [128, 60]. All of this analysis neglects the diffusion transit time (τ_D), which we can derive using the Einstein Relation and Fick's Law:

$$t = 2\sqrt{\mu k_B T \tau_D / q}, \tag{5.2}$$

and solving for τ_D

$$\tau_D = \frac{qt^2}{\mu k_B T}. \tag{5.3}$$

Plugging in the same range of values, we get a range for τ_D of 1 μs to 1 ms.

The absorption of microwaves is directly proportional to the product of the carrier mobility with the number of free carriers:

$$\Delta G = \sum_i \mu N_i, \tag{5.4}$$

where i can indicate both holes and electrons, as well as different types of them (e.g. carriers with lower mobility due to trapping). In the low-fluence (i.e. solar fluence) limit we expect

carrier-carrier interactions to be low, and so the lifetime of the TRMC signal will be mostly due to recombination of free carriers via trapping. Therefore, we can use TRMC to estimate the recombination rates in QD films. Some sample TRMC transients are plotted in Figure 5.6. Clearly, the EDT+hy films have a somewhat longer carrier lifetime than the EDT-only films, suggesting that recombination has indeed been reduced.

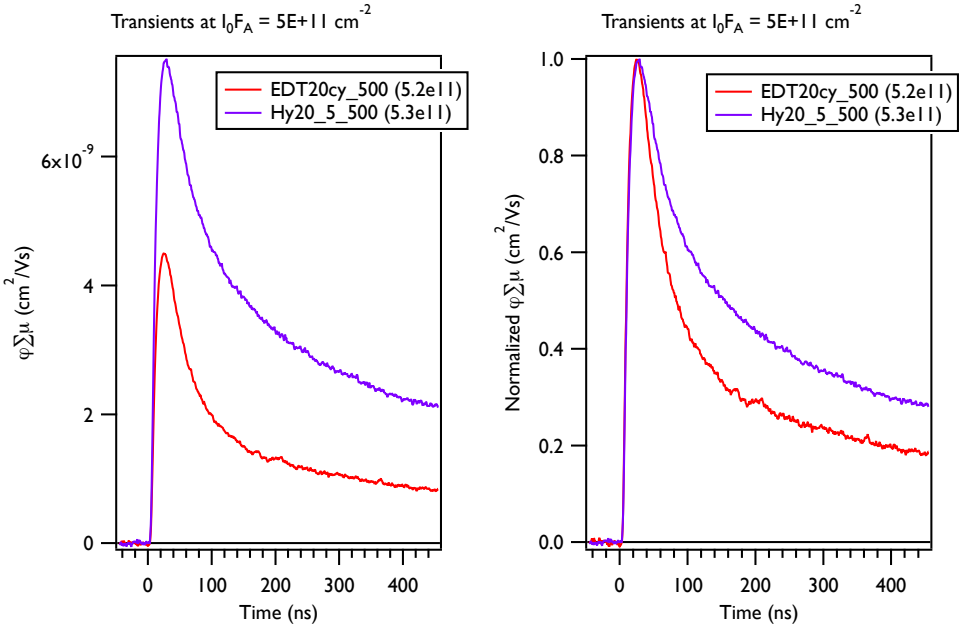

Figure 5.6: Time resolved microwave conductivity on EDT-only and EDT+hy films. **(A)** Raw signal at the second lowest pump fluence, note enhanced signal for EDT+hy. **(B)** Normalized signal to show enhanced lifetime for EDT+hy.

The fact that LbL deposition also contributes to the PV performance suggests that in addition to the hydrazine treating the underlying EDT layer, the weakly treated hydrazine layer is also important. We know that hydrazine is a weak ligand treatment from previous efforts to build hydrazine-only treated solar cells: typically a 1M hydrazine treatment would require orders of magnitude more treatment time to build films comparable to EDT-only treatments. So, we considered the possibility that simply a weakly treated QD film would help device performance, and tried simply depositing a thin layer of QDs (weakly treated) on top of an EDT-treated layer 5.7. This also showed a small improvement, possibly because the

weak treatment leaves more void and carbon-filled space between QDs, allowing thermally evaporated gold to intercalate between the QDs. This could effectively result in a highly doped film, narrowing the Schottky barrier and acting as a tunnel junction. This would explain observation 1, and part of the improved R_s from observation 2.

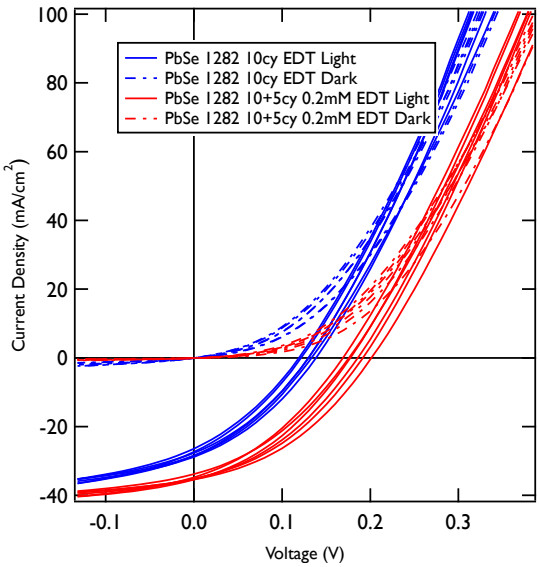

Figure 5.7: Effect of lightly-treated QD "buffer layer." Films were formed with 10 cycles of 5 mM EDT, then 5 cycles of 0.2 mM EDT to emulate the slow treatment of hydrazine. The concentration of 0.2 mM is supported as a "weak treatment" regime by reference [62].

In this picture, the populations of the **A**, **B**, and **E** configurations from Fig. 5.1 are slightly reduced in favor of configuration **D**. The hydrazine can reduce up to four Pb^+ atoms to metallic Pb^0, and provide the same number of protons to form the SH group in unreacted EDT:

$$N_2H_4 + 4Pb^+ + 4HSC_2H_4S^- \longrightarrow N_2 + 4Pb^0 + 4HSC_4H_2SH. \tag{5.5}$$

Chapter 6

Outlook and Future Directions for MEG

6.1 MEG

In the world of energy conversion strategies, photovoltaics rank fairly poorly relative to more mechanical approaches. Power plants harvesting electrical energy from from fossil fuels and nuclear fission are all in the range of 30-60% efficient, and hydroelectric dams are over 90% efficient. Solar panels, meanwhile, are languishing down below 20%. To be fair, steam engines and water wheels have hundreds if not thousands of years of use and experimentation behind them, while solar cells have only been in existence for a little over 100 years and actively developed for less than 60 years [79].

This suggests that maybe there should still be room for solar cells to improve. Measuring the collection of photocurrent benefiting from MEG is a useful step towards tackling some of the assumptions made for the fundamental limits of solar cells. Of course, the η_{MEG} in PbS and PbSe QDs is not efficient enough to have a measurable impact on PCE, as shown in Fig. 4.16. The finding that MEG is preserved in QD solar cells is perhaps the most important aspect of this work then, and the natural question now is how far can this go. If the competition between cooling rates and multiplication rates can be optimized such that η_{MEG} approaches unity, this could prove one promising avenue to approach the thermodynamic limit. We can repeat the detailed balance estimate of PCE for a solar cell with varying η_{MEG}, to give an idea of how close we are to an interesting regime.

Using the detailed balance limit of PCE from Chapter 3, and the MEG model in Beard

et al. [8], I have recalculated the maximum PCE as a function of η_{MEG}. This calculation requires plotting Fig. 1.13 with varying η_{MEG}, and picking the peak value as the bandgap shifts. The result is plotted in Fig. 6.1, along with the known ranges for bulk semiconductors, and values for PbSe QDs and nanorods (NRs). The η_{MEG} values come from fits I have extracted from data published by others previously [98, 114, 17, 125, 89, 8, 21].

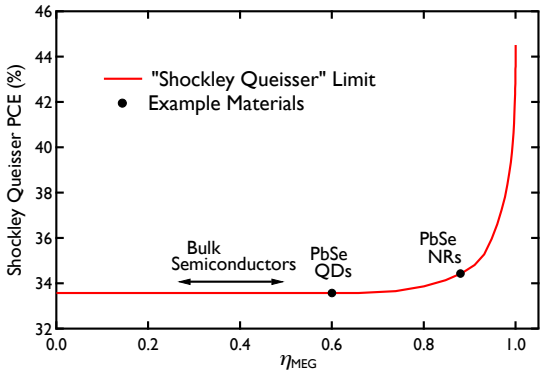

Figure 6.1: Detailed balance limit for PCE with increasing MEG efficiency. Data points are taken from η_{MEG} fits to data from refs [8, 21], and bulk ranges are based on [98, 114, 17, 125, 89]. I should point out that bulk semiconductors do not generally have tunable bandgaps, but this reflects the range of η_{MEG} for most bulk materials of a range of bandgaps.

Although we should have no illusions that the progress from $\eta_{MEG} = 0.88$ to $\eta_{MEG} = 1$ will be as easy as the progress from $\eta_{MEG} = 0.6$ to $\eta_{MEG} = 0.88$, we can see that we are entering the regime where MEG could have a truly meaningful impact on solar cell efficiencies. Already, there are measurements suggesting that Si QDs have a better η_{MEG} than PbSe NRs [7], and going to a 1D silicon structure should further improve this efficiency. It still remains to be seen whether moving from 1D to 2D structures will also improve η_{MEG}, like moving from 0D to 1D has, but syntheses for "nano-platelets" exist [43] and are currently being explored as energy conversion materials. Further, materials with lower dielectric constants (and therefore greater coulombic interactions), such as carbon nanotubes, appear to also have enhanced η_{MEG} [28, 121]. It remains to be seen what will become of this field, but working with structures on these scales certainly gives the motivated researcher

many more knobs to turn.

6.2 QD Solar Cells

Even without MEG, quantum dot solar cells remain a promising technology for inexpensive, scalable, and efficient solar cells. Thanks to their size- and surface-tunability, it should be possible to make efficient devices from quantum dot inks. However, even an MEG solar cell will never be economical if the platform upon which it is based cannot break at least 10% PCE. This means that in addition to searching for ways to maximize η_{MEG}, an equivalent effort focusing on eliminating non-radiative recombination and increasing carrier mobility is of paramount importance. Current voltages and current densities are low relative to the bandgaps we are using. This is because parasitic losses are too much to allow for a thick solar cell with a high voltage. An elegant way to see this is by estimating the "external radiative efficiency" (ERE) of our QD solar cells [33]. The ERE is an estimate of how many carriers absorbed by a solar cell are re-emitted at open circuit, where any losses are due to parasitic non-radiative recombination. At open circuit, in the ideal case, all emission should ideally be due to radiative recombination. ERE can be incorporated into the detailed balance calculation, and it universally reduces the maximum PCE for all bandgaps, although small bandgaps are hurt more than large ones. ERE can be calculated from readily available data:

$$\text{ERE} = \frac{2\pi q}{h^3 c^2} \frac{e^{qV_{OC}/k_B T}}{J_{SC}} \int \frac{EQE\, E^2\, dE}{e^{E/k_B T} - 1}, \tag{6.1}$$

where E is integrated for all photon energies. The integrand is limited by the response of the EQE, but generally peaks just above the bandgap of the solar cell. For the champion 4.5% solar cell presented in Chapter 4, I find an ERE of 3×10^{-5}%, comparable to more modern emerging technologies such as amorphous silicon (5×10^{-6}%) and CdTe (10^{-4}%). Crystalline silicon cells reach as high as 0.6%, while the best GaAs is made by Alta Devices, and records an ERE of 23% [33].

Bibliography

[1] Michiel Aerts, C. S. Suchand Sandeep, Yunan Gao, Tom J Savenije, Juleon M Schins, Arjan J Houtepen, Sachin Kinge, and Laurens D. A Siebbeles. Free charges produced by carrier multiplication in strongly coupled pbse quantum dot films. Nano Lett., 11(10):4485–4489, Jan 2011.

[2] A Paul Alivisatos, Weiwei Gu, and Carolyn Larabell. Quantum Dots as Cellular Probes. Annu. Rev. Biomed. Eng., 7:55–76, January 2005.

[3] J. M. An, A. Franceschetti, and A. Zunger. The Excitonic Exchange Splitting and Radiative Lifetime in PbSe Quantum Dots. Nano Lett., 7(7):2129–2135, July 2007.

[4] Ladislaus Bányai and Stephan W. Koch. Semiconductor Quantum Dots. World Scientific Publishing, Singapore, 1993.

[5] Morgan Baziliana, I Onyeji, M Liebreich, I MacGill, J Chase, J Shah, D Gielen, D Arent, D Landfear, and S Zhengrong. Re-considering the economics of photovoltaic power. Bloomberg New Energy Finance, pages 1–19, May 2012.

[6] Matthew C Beard. Multiple exciton generation in semiconductor quantum dots. J. Phys. Chem. Lett., 2(11):1282–1288, Jun 2011.

[7] Matthew C Beard, Kelly P Knutsen, Pingrong Yu, Joseph M Luther, Qing Song, Wyatt K Metzger, Randy J Ellingson, and Arthur J Nozik. Multiple exciton generation in colloidal silicon nanocrystals. Nano Lett., 7(8):2506–2512, Aug 2007.

[8] Matthew C Beard, Aaron G Midgett, Mark C Hanna, Joseph M Luther, Barbara K Hughes, and Arthur J Nozik. Comparing multiple exciton generation in quantum dots to impact ionization in bulk semiconductors: Implications for enhancement of solar energy conversion. Nano Lett., 10(8):3019–3027, Jan 2010.

[9] Matthew C Beard, Aaron G Midgett, Matt Law, Octavi E Semonin, Randy J Ellingson, and Arthur J Nozik. Variations in the quantum efficiency of multiple exciton generation for a series of chemically treated PbSe nanocrystal films. Nano Lett., 9(2):836–845, Jan 2009.

[10] A Beattie. Quantum efficiency in insb. Journal of Physics and Chemistry of Solids, 23(8):1049–1056, Aug 1962.

[11] W. J. E Beek, L. H Slooff, M. M Wienk, J. M Kroon, and R. A. J Janssen. Hybrid solar cells using a zinc oxide precursor and a conjugated polymer. Adv. Funct. Mater., 15(10):1703–1707, Oct 2005.

[12] M. Brumer, A. Kigel, L. Amirav, A. Sashchiuk, O. Solomesch, N. Tessler, and E. Lifshitz. PbSe/PbS and PbSe/$PbSe_xS_{1-x}$ Core/Shell Nanocrystals. Adv. Funct. Mater., 15(7):1111–1116, July 2005.

[13] L Canfield, R Vest, R Korde, H Schmidtke, and R Desor. Absolute silicon photodiodes for 160 nm to 254 nm photons. Metrologia, 35:329, Aug 1998.

[14] Joshua J Choi, Yee-Fun Lim, Mitk'El B Santiago-Berrios, Matthew Oh, Byung-Ryool Hyun, Liangfeng Sung, Adam C Bartnik, Augusta Goedhart, George G Malliaras, Hector D Abruna, Frank W Wise, and Tobias Hanrath. Pbse nanocrystal excitonic solar cells. Nano Lett., 9(11):3749–3755, Jan 2009.

[15] Joshua J Choi, Yee-Fun Lim, Mitk'El B Santiago-Berrios, Matthew Oh, Byung-Ryool Hyun, Liangfeng Sung, Adam C Bartnik, Augusta Goedhart, George G Malliaras, Hector D Abruna, Frank W Wise, and Tobias Hanrath. Pbse nanocrystal excitonic solar cells. Nano Lett., 9(11):3749–3755, Jan 2009.

[16] S. G Choi, M Van Schilfgaarde, D. E Aspnes, A. G Norman, J. M Olson, T. J Peshek, and D. H Levi. Above-band-gap dielectric functions of zngeas2: Ellipsometric measurements and quasiparticle self-consistent gw calculations. Phys. Rev. B, 83(23):235210, Jan 2011.

[17] Ove Christensen. Quantum efficiency of the internal photoelectric effect in silicon and germanium. J. Appl. Phys., 47(2):689, Jan 1976.

[18] Ryan Cooney, Samuel Sewall, Eva Dias, D. Sagar, Kevin Anderson, and Patanjali Kambhampati. Unified Picture of Electron and Hole Relaxation Pathways in Semiconductor Quantum Dots. Phys. Rev. B, 75(24):1–14, June 2007.

[19] A Cravino, P Schilinsky, and C.J Brabec. Characterization of organic solar cells: the importance of device layout. Adv. Funct. Mater., 17(18):3906–3910, Dec 2007.

[20] Glenn A. Crosby and James N. Demas. Measurement of Photoluminescence Quantum Yields. A Review. J. Phys. Chem., 75(8):991–1024, April 1971.

[21] Paul D Cunningham, Janice E Boercker, Edward E Foos, Matthew P Lumb, Anthony R Smith, Joseph G Tischler, and Joseph S Melinger. Enhanced multiple exciton generation in quasi-one-dimensional semiconductors. Nano Lett., 11(8):3476–3481, Jan 2011. What's dielectric screening?

[22] Quanqin Dai, Yingnan Wang, Xinbi Li, Yu Zhang, Donald J Pellegrino, Muxun Zhao, Bo Zou, Jaetae Seo, Yiding Wang, and William W Yu. Size-dependent composition and molar extinction coefficient of pbse semiconductor nanocrystals. ACS nano, 3(6):1518–1524, Jun 2009.

[23] Christophe Delerue, Guy Allan, J. J. H Pijpers, and M Bonn. Carrier multiplication in bulk and nanocrystalline semiconductors: Mechanism, efficiency, and interest for solar cells. Phys. Rev. B, 81(12):125306, Jan 2010.

[24] E.a. Dias, S.L. Sewall, and P. Kambhampati. Light Harvesting and Carrier Transport in Core/Barrier/Shell Semiconductor Nanocrystals. J. Phys. Chem. C, 111(2):708–713, January 2007.

[25] Christopher M Evans, Li Guo, Jeffrey J Peterson, Sara Maccagnano-Zacher, and Todd D Krauss. Ultrabright pbse magic-sized clusters. Nano Lett., 8(9):2896–2899, Jan 2008.

[26] A Franceschetti. Structural and electronic properties of pbse nanocrystals from first principles. Phys. Rev. B, 78(7):075418, Aug 2008.

[27] Huaxiang Fu and Alex Zunger. InP Quantum Dots: Electronic Structure, Surface Effects, and the Redshifted Emission. Phys. Rev. B, 56(3):1496–1508, July 1997.

[28] N. M Gabor, Z Zhong, K Bosnick, J Park, and P. L Mceuen. Extremely efficient multiple electron-hole pair generation in carbon nanotube photodiodes. Science, 325(5946):1367–1371, Sep 2009.

[29] Yanqin Gai, Haowei Peng, and Jingbo Li. Electronic properties of nonstoichiometric pbse quantum dots from first principles. J. Phys. Chem. C, 113(52):21506–21511, Dec 2009.

[30] Jianbo Gao, Joseph M Luther, Octavi E Semonin, Randy J Ellingson, Arthur J Nozik, and Matthew C Beard. Quantum dot size dependent J-V characteristics in heterojunction ZnO/PbS quantum dot solar cells. Nano Lett., 11(3):1002–1008, Jan 2011.

[31] Jianbo Gao, Craig L Perkins, Joseph M Luther, Mark C Hanna, Hsiang-Yu Chen, Octavi E Semonin, Arthur J Nozik, Randy J Ellingson, and Matthew C Beard. n-type transition metal oxide as a hole extraction layer in PbS quantum dot solar cells. Nano Lett., 11(8):3263–3266, Jan 2011.

[32] M Green, K Emery, Y Hishikawa, Wilhelm Warta, and Ewan D Dunlop. Solar cell efficiency tables (version 39). Progress in Photovoltaics: Research and Applications, 20(1):12–20, Jan 2012.

[33] M.A Green. Radiative efficiency of stateoftheart photovoltaic cells. Progress in Photovoltaics: Research and Applications, 20:472, 2012.

[34] I Gur, N.A Fromer, M.L Geier, and A.P Alivisatos. Air-stable all-inorganic nanocrystal solar cells processed from solution. Science, 310(5747):462, 2005.

[35] Philippe Guyot-Sionnest, Brian L. Wehrenberg, and Dong Yu. Intraband Relaxation in CdSe Nanocrystals and the Strong Influence of the Surface Ligands. J. Chem. Phys., 123(7):074709, August 2005.

[36] MC Hanna and AJ Nozik. Solar conversion efficiency of photovoltaic and photoelectrolysis cells with carrier multiplication absorbers. J. Appl. Phys., 100:074510, 2006.

[37] W. M. Haynes and David R. Lide, editors. CRC Handbook of Chemistry and Physics. Taylor & Francis, Oxford, 92nd edition, 2012.

[38] Robert C. Hilborn. Einstein Coefficients, Cross Sections, F Values, Dipole Moments, and All That. Am. J. Phys., 50(11):982–986, November 1982.

[39] M.A Hines and G.D Scholes. Colloidal pbs nanocrystals with size-tunable near-infrared emission: Observation of post-synthesis self-narrowing of the particle size distribution. Adv. Mater., 15(21):1844–1849, Nov 2003.

[40] B Hughes, D Ruddy, J Blackburn, and D Smith.... Control of pbse quantum dot surface chemistry and photophysics using an alkylselenide ligand. ACS nano, Jan 2012.

[41] Barbara K Hughes, Joseph M Luther, and Matthew C Beard. The subtle chemistry of colloidal, quantum-confined semiconductor nanostructures. ACS nano, page 120615094724008, Jun 2012.

[42] Byung-Ryool Hyun, Yu-Wu Zhong, Adam C Bartnik, Liangfeng Sun, Hector D Abruna, Frank W Wise, Jason D Goodreau, James R Matthews, Thomas M Leslie, and Nicholas F Borrelli. Electron injection from colloidal pbs quantum dots into titanium dioxide nanoparticles. ACS nano, 2(11):2206–2212, Jan 2008.

[43] S Ithurria, M. D Tessier, B Mahler, R. P. S. M Lobo, B Dubertret, and Al. L Efros. Colloidal nanoplatelets with two-dimensional electronic structure. Nat Mater, 10(12):936–941, Oct 2011.

[44] Kwang S Jeong, Jiang Tang, Huan Liu, Jihye Kim, Andrew W Schaefer, Kyle Kemp, Larissa Levina, Xihua Wang, Sjoerd Hoogland, Ratan Debnath, Lukasz Brzozowski, Edward H Sargent, and John B Asbury. Enhanced mobility-lifetime products in pbs colloidal quantum dot photovoltaics. ACS nano, 6(1):89–99, Jan 2012.

[45] Keith W Johnston, Andras G Pattantyus-Abraham, Jason P Clifford, Stefan H Myrskog, Sjoerd Hoogland, Harnik Shukla, Ethan J. D Klem, Larissa Levina, and Edward H Sargent. Efficient schottky-quantum-dot photovoltaics: The roles of depletion, drift, and diffusion. Appl. Phys. Lett., 92(12):122111, Jan 2008.

[46] Ethan J D Klem, Dean D Macneil, Paul W Cyr, Larissa Levina, and Edward H Sargent. Efficient solution-processed infrared photovoltaic cells: Planarized all-inorganic bulk heterojunction devices via inter-quantum-dot bridging during growth from solution. Appl. Phys. Lett., 90(18):183113, Mar 2007.

[47] Ghada I Koleilat, Larissa Levina, Harnik Shukla, Stefan H Myrskog, Sean Hinds, Andras G Pattantyus-Abraham, and Edward H Sargent. Efficient, stable infrared photovoltaics based on solution-cast colloidal quantum dots. ACS nano, 2(5):833–840, Jan 2008.

[48] G Konstantatos, I Howard, A Fischer, S Hoogland, J Clifford, E Klem, L Levina, and EH Sargent. Ultrasensitive solution-cast quantum dot photodetectors. Nature, 442(7099):180–183, Jan 2006.

[49] B. Kopainsky, P. Qiu, W. Kaiser, B. Sens, and K. H. Drexhage. Lifetime, Photostability, and Chemical Structure of IR Heptamethine Cyanine Dyes Absorbing Beyond 1 μm. Appl. Phys. B, 29(1):15–18, September 1982.

[50] MaksymV Kovalenko, DmitriV Talapin, MariaAntonietta Loi, Fabrizio Cordella, Günter Hesser, MarynaI Bodnarchuk, and Wolfgang Heiss. Quasi-seeded growth of ligand-tailored pbse nanocrystals through cation-exchange-mediated nucleation. Angew. Chem. Int. Ed., 47(16):3029–3033, Apr 2008.

[51] Peter T. Landsberg. Recombination in Semiconductors. Cambridge University Press, 2003.

[52] M Law, JM Luther, Q Song, BK Hughes, CL Perkins, and AJ Nozik. Structural, optical, and electrical properties of pbse nanocrystal solids treated thermally or with simple amines. J. Am. Chem. Soc., 130(18):5974–5985, 2008.

[53] Matt Law, Matthew C Beard, Sukgeun Choi, Joseph M Luther, Mark C Hanna, and Arthur J Nozik. Determining the internal quantum efficiency of pbse nanocrystal solar cells with the aid of an optical model. Nano Lett., 8(11):3904–3910, Jan 2008.

[54] C. A. Leatherdale, W.-K. Woo, F. V. Mikulec, and M. G. Bawendi. On the Absorption Cross Section of CdSe Nanocrystal Quantum Dots. J. Phys. Chem. B, 106(31):7619–7622, August 2002.

[55] K Lee, JY Kim, SH Park, SH Kim, S Cho, and AJ Heeger. Airstable polymer electronic devices. Adv. Mater., 19(18):2445–2449, 2007.

[56] Kurtis S Leschkies, Timothy J Beatty, Moon Sung Kang, David J Norris, and Eray S Aydil. Solar cells based on junctions between colloidal pbse nanocrystals and thin zno films. ACS nano, 3(11):3638–3648, Nov 2009.

[57] Kurtis S Leschkies, Alan G Jacobs, David J Norris, and Eray S Aydil. Nanowire-quantum-dot solar cells and the influence of nanowire length on the charge collection efficiency. Appl. Phys. Lett., 95(19):193103, Nov 2009.

[58] Nathan S Lewis. Powering the planet. MRS bulletin, 32, 2007.

[59] Heng Liu and Philippe Guyot-Sionnest. Photoluminescence lifetime of lead selenide colloidal quantum dots. J Phys Chem C, 114(35):14860–14863, Jan 2010.

[60] Yao Liu, Markelle Gibbs, Craig L Perkins, Jason Tolentino, Mohammad H Zarghami, Jorge Bustamante, and Matt Law. Robust, functional nanocrystal solids by infilling with atomic layer deposition. Nano Lett., 11(12):5349–5355, Dec 2011.

[61] Matthew T Lloyd, Craig H Peters, Andres Garcia, Isaac V Kauvar, Joseph J Berry, Matthew O Reese, Michael D Mcgehee, David S Ginley, and Dana C Olson. Influence of the hole-transport layer on the initial behavior and lifetime of inverted organic photovoltaics. Sol. Energ. Mat. Sol. C., 95(5):1382–1388, May 2011.

[62] JM Luther, M Law, Q Song, CL Perkins, MC Beard, and AJ Nozik. Structural, optical, and electrical properties of self-assembled films of pbse nanocrystals treated with 1, 2-ethanedithiol. ACS nano, 2(2):271–280, 2008.

[63] Joseph M Luther, Matthew C Beard, Qing Song, Matt Law, Randy J Ellingson, and Arthur J Nozik. Multiple exciton generation in films of electronically coupled pbse quantum dots. Nano Lett., 7(6):1779–1784, Jan 2007.

[64] Joseph M Luther, Jianbo Gao, Matthew T Lloyd, Octavi E Semonin, Matthew C Beard, and Arthur J Nozik. Stability assessment on a 3% bilayer PbS/ZnO quantum dot heterojunction solar cell. Adv. Mater., 22(33):3704, Jan 2010.

[65] Joseph M Luther, Matt Law, Matthew C Beard, Qing Song, Matthew O Reese, Randy J Ellingson, and Arthur J Nozik. Schottky Solar Cells Based on Colloidal Nanocrystal Films. Nano Lett., 8(10):3488–3492, October 2008.

[66] Joseph M Luther, Matt Law, Matthew C Beard, Qing Song, Matthew O Reese, Randy J Ellingson, and Arthur J Nozik. Schottky solar cells based on colloidal nanocrystal films. Nano Lett., 8(10):3488–3492, Jan 2008.

[67] Joseph M Luther, Matt Law, Matthew C Beard, Qing Song, Matthew O Reese, Randy J Ellingson, and Arthur J Nozik. Schottky solar cells based on colloidal nanocrystal films. Nano Lett., 8(10):3488–3492, Oct 2008.

[68] Wanli Ma, Joseph M Luther, Haimei Zheng, Yue Wu, and A. Paul Alivisatos. Photovoltaic devices employing ternary pbs xse 1 -xnanocrystals. Nano Lett., 9(4):1699–1703, Apr 2009.

[69] John A Mcguire, Jin Joo, Jeffrey M Pietryga, Richard D Schaller, and Victor I Klimov. New aspects of carrier multiplication in semiconductor nanocrystals. Accounts Chem Res, 41(12):1810–1819, Jan 2008.

[70] John A Mcguire, Milan Sykora, Jin Joo, Jeffrey M Pietryga, and Victor I Klimov. Apparent versus true carrier multiplication yields in semiconductor nanocrystals. Nano Lett., 10(6):2049–2057, Jan 2010.

[71] Aaron G Midgett, Hugh W Hillhouse, Barbara K Huges, Arthur J Nozik, and Matthew C Beard. Flowing versus static conditions for measuring multiple exciton generation in pbse quantum dots. J Phys Chem C, 114(41):17486–17500, Jan 2010.

[72] I Moreels, Y Justo, B De Geyter, K Haustraete, J.C Martins, and Z Hens. Size-tunable, bright, and stable pbs quantum dots: A surface chemistry study. ACS nano, 2011.

[73] Iwan Moreels, Bernd Fritzinger, José C Martins, and Zeger Hens. Surface chemistry of colloidal pbse nanocrystals. Journal of the American ..., 130(45):15081, Jan 2008.

[74] Iwan Moreels, Karel Lambert, David De Muynck, Frank Vanhaecke, Dirk Poelman, José C. Martins, Guy Allan, and Zeger Hens. Composition and Size-Dependent Extinction Coefficient of Colloidal PbSe Quantum Dots. Chem. Mater., 19(25):6101–6106, December 2007.

[75] Iwan Moreels, Karel Lambert, David De Muynck, Frank Vanhaecke, Dirk Poelman, Jose C Martins, Guy Allan, and Zeger Hens. Composition and size-dependent extinction coefficient of colloidal pbse quantum dots. Chem Mater, 19(25):6101–6106, Jan 2007.

[76] James E Murphy, Matthew C Beard, Andrew G Norman, S Phillip Ahrenkiel, Justin C Johnson, Pingrong Yu, Olga I Mićić, Randy J Ellingson, and Arthur J Nozik. PbTe Colloidal Nanocrystals: Synthesis, Characterization, and Multiple Exciton Generation. J. Am. Chem. Soc., 128(10):3241–3247, March 2006.

[77] JE Murphy, MC Beard, AG Norman, SP Ahrenkiel, JC Johnson, PR Yu, OI Micic, RJ Ellingson, and AJ Nozik. Pbte colloidal nanocrystals: Synthesis, characterization, and multiple exciton generation. J. Am. Chem. Soc., 128(10):3241–3247, Jan 2006.

[78] G Nair, L.Y Chang, S.M Geyer, and M.G Bawendi. Perspective on the prospects of a carrier multiplication nanocrystal solar cell. Nano Lett., 11(5):2145–2151, 2011.

[79] J. Nelson. The Physics of Solar Cells. Imperial College Press, London, 2003.

[80] M. Nirmal, B. O. Dabbousi, M. G. Bawendi, J. J. Macklin, J. K. Trautman, T. D. Harris, and L. E. Brus. Fluorescence Intermittency in Single Cadmium Selenide Nanocrystals. Nature, 383(6603):802–804, October 1996.

[81] David J. Norris. Electronic structure in semiconductor nanocrystals. In Victor Klimov, editor, Semiconductor and Metal Nanocrystals, pages 65–102. Marcel Dekker, Inc., 2004.

[82] AJ Nozik. Quantum dot solar cells. Physica E, 14(1-2):115–120, Dec 2002.

[83] A Pandey and P Guyot-Sionnest. Slow electron cooling in colloidal quantum dots. Science, 322(5903):929, 2008.

[84] A Penzkofer, O Lammel, and T Tsuboi. Emission Spectroscopic Characterisation of F_2 Colour Centres in a LiF Crystal. Opt. Commun., 214(1-6):305–313, December 2002.

[85] Jeffrey J Peterson and Todd D Krauss. Fluorescence Spectroscopy of Single Lead Sulfide Quantum Dots. Nano Lett., 6(3):510–514, March 2006.

[86] Jeffrey M Pietryga, Richard D Schaller, Donald Werder, Michael H Stewart, Victor I Klimov, and Jennifer A Hollingsworth. Pushing the Band Gap Envelope: Mid-infrared Emitting Colloidal Pbse Quantum Dots. J. Am. Chem. Soc., 126(38):11752–11753, September 2004.

[87] Jeffrey M Pietryga, Donald J Werder, Darrick J Williams, Joanna L Casson, Richard D Schaller, Victor I Klimov, and Jennifer A Hollingsworth. Utilizing the Lability of Lead Selenide to Produce Heterostructured Nanocrystals with Bright, Stable Infrared Emission. J. Am. Chem. Soc., 130(14):4879–4885, April 2008.

[88] JM Pietryga, RD Schaller, D Werder, MH Stewart, VI Klimov, and JA Hollingsworth. Pushing the band gap envelope: Mid-infrared emitting colloidal pbse quantum dots. J. Am. Chem. Soc., 126(38):11752–11753, Jan 2004.

[89] J. J. H Pijpers, R Ulbricht, K. J Tielrooij, A Osherov, Y Golan, C Delerue, G Allan, and M Bonn. Assessment of carrier-multiplication efficiency in bulk pbse and pbs. Nature Physics, 5(11):811–814, Jan 2009.

[90] Brian K. Ridley. Quantum Processes in Semiconductors. Oxford University Press, New York, 4th edition, 2000.

[91] Garry Rumbles, Donald C Selmarten, Randy J Ellingson, Jeffrey L Blackburn, Pingrong Yu, Barton B Smith, Olga I Mićić, and Arthur J Nozik. Anomalies in the Linear Absorption, Transient Absorption, Photoluminescence and Photoluminescence Excitation Spectroscopies of Colloidal InP Quantum Dots. J. Photochem. Photobiol. A Chem., 142:187–195, September 2001.

[92] Justin B Sambur, Thomas Novet, and B. A Parkinson. Multiple exciton collection in a sensitized photovoltaic system. Science, 330(6000):63–66, Jan 2010.

[93] Octavi E Semonin, Justin C Johnson, Joseph M Luther, Aaron G Midgett, Arthur J Nozik, and Matthew C Beard. Absolute photoluminescence quantum yields of IR-26 dye, PbS, and PbSe quantum dots. J. Phys. Chem. Lett., 1(16):2445–2450, Aug 2010.

[94] Octavi E Semonin, Joseph M Luther, Sukgeun Choi, Hsiang-Yu Chen, Jianbo Gao, Arthur J Nozik, and Matthew C Beard. Peak external photocurrent quantum efficiency exceeding 100% via MEG in a quantum dot solar cell. Science, 334(6062):1530–1533, Jan 2011.

[95] Samuel L Sewall, Ryan R Cooney, Kevin E H Anderson, Eva A Dias, D M Sagar, and Patanjali Kambhampati. State-resolved studies of biexcitons and surface trapping dynamics in semiconductor quantum dots. J. Chem. Phys., 129(8):084701, August 2008.

[96] William Shockley and Hans J Queisser. Detailed balance limit of efficiency of p-n junction solar cells. J. Appl. Phys., 32(3):510, Jan 1961.

[97] Vishal Shrotriya, Gang Li, Yan Yao, Tom Moriarty, Keith Emery, and Yang Yang. Accurate measurement and characterization of organic solar cells. Adv. Funct. Mater., 16(15):2016–2023, Jan 2006.

[98] A Smith and D Dutton. Behavior of lead sulfide photocells in the ultraviolet. J. Opt. Soc. Am., 48(12):1007–1009, 1958.

[99] A Smith and D Dutton. Photoconductivity and the external photoelectric effect in pbs. Journal of Physics and Chemistry of Solids, 22:351–363, Dec 1961.

[100] Danielle K Smith, Joseph M Luther, Octavi E Semonin, Arthur J Nozik, and Matthew C Beard. Tuning the synthesis of ternary lead chalcogenide quantum dots by balancing precursor reactivity. ACS nano, 5(1):183–190, Jan 2011.

[101] GeoModel Solar. Solar gis, 2012.

[102] J.S. Steckel, S. Coe-Sullivan, V. Bulović, and M.G. Bawendi. 1.3 μm to 1.55 μm Tunable Electroluminescence from PbSe Quantum Dots Embedded within an Organic Device. Adv. Mater., 15(21):1862–1866, November 2003.

[103] Walter S. Struve. Anoxygenic Photosynthetic Bacteria. Kluwer Academic Publishers, Dordrecht, 1995.

[104] V Sukhovatkin, S Hinds, L Brzozowski, and E. H Sargent. Colloidal quantum-dot photodetectors exploiting multiexciton generation. Science, 324(5934):1542–1544, Jun 2009.

[105] Baoquan Sun, Alp T Findikoglu, Milan Sykora, Donald J Werder, and Victor I Klimov. Hybrid photovoltaics based on semiconductor nanocrystals and amorphous silicon. Nano Lett., 9(3):1235–1241, Mar 2009.

[106] M Sykora, AY Koposov, JA McGuire, RK Schulze, O Tretiak, JM Pietryga, and VI Klimov. Effect of air exposure on surface properties, electronic structure, and carrier relaxation in pbse nanocrystals. ACS nano, 4(4):2021–2034, 2010.

[107] Milan Sykora, Alexey Y Koposov, John A McGuire, Roland K Schulze, Olexandr Tretiak, Jeffrey M Pietryga, and Victor I Klimov. Effect of Air Exposure on Surface Properties, Electronic Structure, and Carrier Relaxation in PbSe Nanocrystals. ACS Nano, 4(4):2021–2034, April 2010.

[108] S. M. Sze and N. G. Kwok. Physics of Semiconductors. John-Wiley & Sons, New York, 3rd edition, 2007.

[109] Dmitri V Talapin, Jong-Soo Lee, Maksym V Kovalenko, and Elena V Shevchenko. Prospects of Colloidal Nanocrystals for Electronic and Optoelectronic Applications. Chem. Rev., 110(1):389–458, January 2010.

[110] Dmitri V Talapin, Jong-Soo Lee, Maksym V Kovalenko, and Elena V Shevchenko. Prospects of colloidal nanocrystals for electronic and optoelectronic applications. Chem Rev, 110(1):389–458, Jan 2010.

[111] DV Talapin and CB Murray. Pbse nanocrystal solids for n- and p-channel thin film field-effect transistors. Science, 310(5745):86–89, Jan 2005.

[112] Jiang Tang, Lukasz Brzozowski, D. Aaron R Barkhouse, Xihua Wang, Ratan Debnath, Remigiusz Wolowiec, Elenita Palmiano, Larissa Levina, Andras G Pattantyus-Abraham, Damir Jamakosmanovic, and Edward H Sargent. Quantum dot photovoltaics in the extreme quantum confinement regime: The surface-chemical origins of exceptional air- and light-stability. ACS nano, 4(2):869–878, Jan 2010.

[113] Jiang Tang, Xihua Wang, Lukasz Brzozowski, D. Aaron R Barkhouse, Ratan Debnath, Larissa Levina, and Edward H Sargent. Schottky quantum dot solar cells stable in air under solar illumination. Adv. Mater., 22(12):1398–1402, Jan 2010.

[114] J Tauc. Electron impact ionization in semiconductors. Journal of Physics and Chemistry of Solids, 8:219–223, 1959.

[115] Brooke A Timp and X Y Zhu. Electronic energy alignment at the pbse quantum dots/zno(1010) interface. Surf. Sci., 604(17-18):1335–1341, Feb 2010.

[116] John S. Townsend. A Modern Approach to Quantum Mechanics. University Science Books, Sausalito, California, 2000.

[117] S. W Tsang, H Fu, R Wang, J Lu, K Yu, and Y Tao. Highly efficient cross-linked pbs nanocrystal/c60 hybrid heterojunction photovoltaic cells. Appl. Phys. Lett., 95(18):183505, Jan 2009.

[118] V.S Vavilov. On photo-ionization by fast electrons in germanium and silicon. Journal of Physics and Chemistry of Solids, 8:223–226, 1959.

[119] C Wadia, AP Alivisatos, and DM Kammen. Materials availability expands the opportunity for large-scale photovoltaics deployment. Environ. Sci. Technol, 43(6):2072–2077, 2009.

[120] Robert Y Wang, Joseph P Feser, Jong-Soo Lee, Dmitri V Talapin, Rachel Segalman, and Arun Majumdar. Enhanced thermopower in pbse nanocrystal quantum dot superlattices. Nano Lett., 8(8):2283–2288, Jan 2008.

[121] Shujing Wang, Marat Khafizov, Xiaomin Tu, Ming Zheng, and Todd D Krauss. Multiple exciton generation in single-walled carbon nanotubes. Nano Lett., 10(7):2381–2386, Jul 2010.

[122] Brian L. Wehrenberg, Congjun Wang, and Philippe Guyot-Sionnest. Interband and Intraband Optical Studies of PbSe Colloidal Quantum Dots. J. Phys. Chem. B, 106(41):10634–10640, October 2002.

[123] M S White, D C Olson, S E Shaheen, N Kopidakis, and D S Ginley. Inverted bulk-heterojunction organic photovoltaic device using a solution-derived zno underlayer. Appl. Phys. Lett., 89(14):143517, Oct 2006.

[124] Frank W Wise. Lead salt quantum dots: the limit of strong quantum confinement. Acc. Chem. Res., 33(11):773–780, Nov 2000.

[125] M Wolf, R Brendel, J H Werner, and H J Queisser. Solar cell efficiency and carrier multiplication in si1xgex alloys. J. Appl. Phys., 83(8):4213, 1998.

[126] P Yu, MC Beard, RJ Ellingson, S Ferrere, C Curtis, J Drexler, F Luiszer, and AJ Nozik. Absorption cross-section and related optical properties of colloidal inas quantum dots. J. Phys. Chem. B, 109(15):7084–7087, 2005.

[127] Pingrong Yu, Matthew C Beard, Randy J Ellingson, Suzanne Ferrere, Calvin Curtis, John Drexler, Fred Luiszer, and Arthur J Nozik. Absorption Cross-section and Related Optical Properties of Colloidal InAs Quantum Dots. J. Phys. Chem. B, 109(15):7084–7087, April 2005.

[128] Mohammad H Zarghami, Yao Liu, Markelle Gibbs, Eminet Gebremichael, Christopher Webster, and Matt Law. p-type pbse and pbs quantum dot solids prepared with short-chain acids and diacids. ACS nano, 4(4):2475–2485, Jan 2010.

[129] Luyuan Zhang, Longwei Yin, Chengxiang Wang, Ning Lun, Yongxin Qi, and Dong Xiang. Origin of Visible Photoluminescence of ZnO Quantum Dots: Defect-Dependent and Size-Dependent. J. Phys. Chem. C, 114(21):9651–9658, June 2010.

[130] B Zimmermann, U Würfel, and M Niggemann. Longterm stability of efficient inverted p3ht:pcbm solar cells. Solar Energy Materials and Solar Cells, 93(4):491, 2009.

Appendix A

Impact ionization threshold in bulk semiconductors

This Appendix is a calculation of the impact ionization (II) threshold, E_{th}, above which II can occur in a single macro-semiconductor crystal. We assume the material has symmetric parabolic bands, a direct bandgap, with effective mass m_e for both electrons and holes. We conserve crystal momentum and energy, and assume a transition of an excited electron relaxing towards the conduction band edge, while promoting another electron in the valence band across the bandgap, as in Fig. A.1.

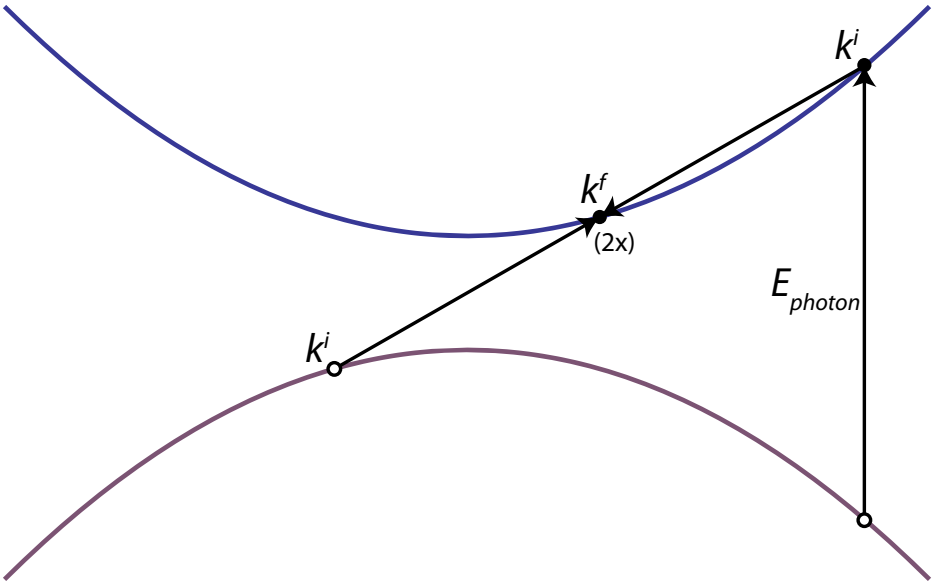

Figure A.1: Diagram of impact ionization in a parabolic band semiconductor

We start with the conservation of momentum

$$\Delta k_v = \Delta k_c, \tag{A.1}$$

where the subscript v is for the electron starting in the valence band, and c is for the excited electron in the conduction band. We can define initial (superscript i) and final (superscript f) momenta,

$$k_v^f - k_v^i = k_c^i - k_c^f, \tag{A.2}$$

where the sign reversal indicates the electrons come from opposite sides of the parabola. We now conserve energy,

$$\Delta E_v = \Delta E_c, \tag{A.3}$$

and input the energies of these states,

$$E_g + \frac{\hbar^2}{2m_e}\left[(k_v^i)^2 + (k_v^f)^2\right] = \frac{\hbar^2}{2m_e}\left[(k_c^i)^2 - (k_c^f)^2\right], \tag{A.4}$$

where E_g is the direct bandgap. We solve Eq. A.2 for k_v^i in order to eliminate it from Eq. A.4. When we substitute this into Eq. A.4, we conveniently note that only linear terms in k_c^i remain, and so we can solve for,

$$k_c^i(k_c^f, k_v^f) = \frac{2m_e E_g/\hbar^2 + 2(k_c^f)^2 + 2(k_v^f)^2 + 2k_c^f k_v^f}{2(k_c^f + k_v^f)}. \tag{A.5}$$

This function has a local minimum for

$$\frac{\hbar^2(k_c^f)^2}{2m_e} = \frac{\hbar^2(k_v^f)^2}{2m_e} = \frac{1}{6}E_g \rightarrow \frac{\hbar^2(k_c^i)^2}{2m_e} = \frac{3}{2}E_g. \tag{A.6}$$

The we plug in k_c^i to find the threshold photon energy

$$E_{th} = E_g + \frac{\hbar^2(k_c^i)^2}{m_e} = 4E_g. \tag{A.7}$$

A threshold of $4E_g$ is roughly consistent with known quantum yields for bulk semiconductors. For example, in Ge the threshold is $4.1E_g$, and in Si it is $3.5E_g$ [125, 13].

Appendix B

A personal reflection on making solar cells, with data

At NREL I have run JV curves almost 2,000 times. This does not mean that I've made that many devices, but that of the many hundreds I have made, I have measured the JV curve of a device quite a few times. After filtering down to 1,499 measurements, I have extracted a couple interesting things. The first, most natural, thing to try is to simply plot every PCE I have measured (Fig. B.1. When we do this, we can see that while some progress occurred in my first two years, the only significant achievement in PCE occurred in the beginning of my third year at NREL (I started at NREL around January 2008). This milestone indicates when I found the secondary hydrazine treatment. We can also see that this finding was accompanied by me making quite a few measurements (almost 100/month).

The only other observation I'd like to share are some thoughts on what day of the week seemed to be most productive for me. I should point out that I organize my data by folders named with the date that the device was *made* not when it was measured. This allows me to see when it is best to make the device. The results seem to pretty unambiguously suggest that weekends are the best days to work, not that I seem to have taken full advantage of this in my dissertation. As we can see from the top histogram in Fig. B.2, Tuesday, Wednesday, and Thursday are by far my favorite days to make solar cells, with more than 70% of my devices made mid-week.

They are also days that yield very good solar cells, with several records set on TuWeTh (see middle panel of Fig. B.2). However, simply because I make a lot of solar cells, we would

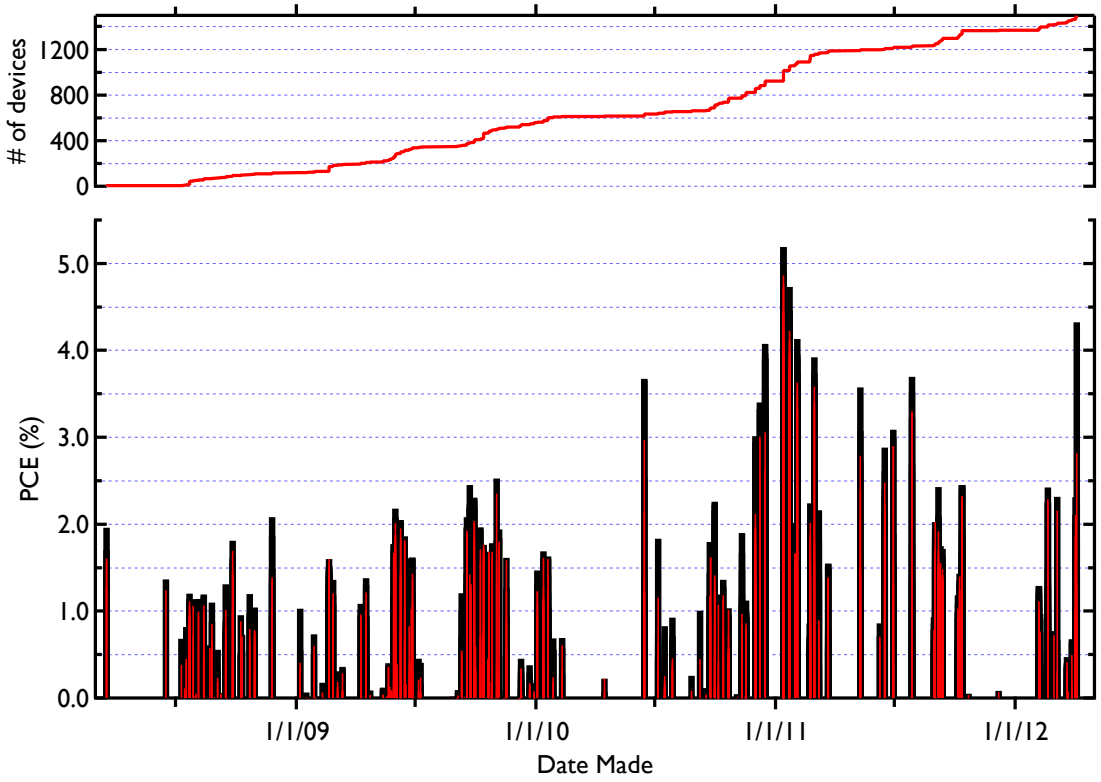

Figure B.1: Best and mean PCE, chronologically. For each day a device was made, the best device from that day is plotted (both the champion pixel and the average chip PCE).

expect those days to have more champion devices. A better measure of when to make a solar cell is the fraction of solar cells made on a given day are "successful." I have somewhat arbitrarily set that bar at 1%, and here we see an opposite trend: while I was quite prolific mid-week, I would have been better off working on Saturdays. This could be due to a couple things: **(a)** I save my most exciting or important experiments for the weekends, when I am most motivated to come in on a weekend. **(b)** Since there are few other people around on Saturdays, there are fewer disturbances in my working conditions to send experiments awry. Further experimentation will be necessary to sort this one out.

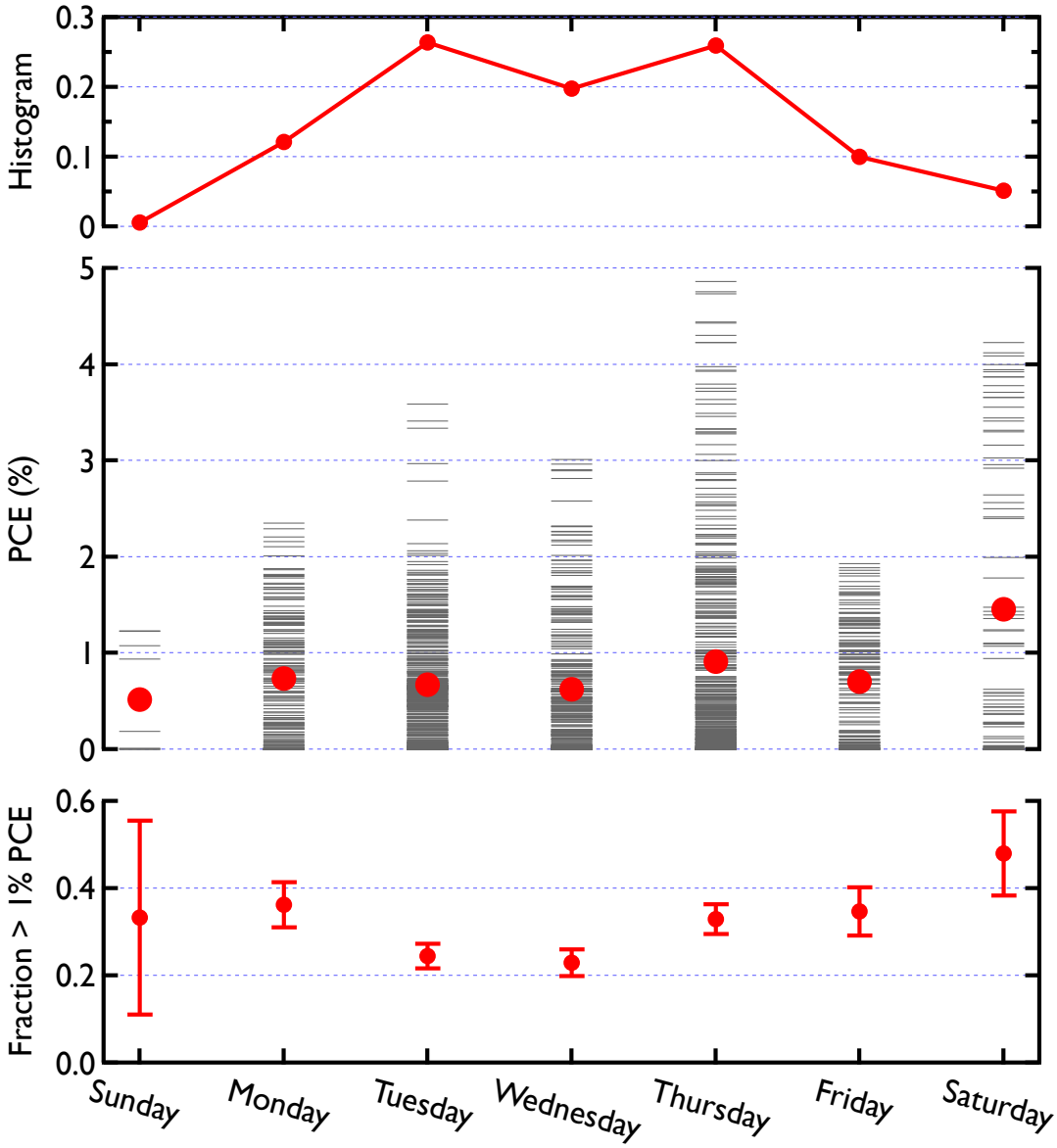

Figure B.2: Best days to make a solar cell. Histogram of number of devices made by day (top), power conversion efficiency by day (middle), and success rate (fraction of devices with PCE $> 1\%$, bottom). In the middle panel, the horizontal lines represent every device tested, while the red dots are the mean PCE.

Appendix C

Tips on how to do little things in the lab

C.1 How to correct for reflectance of the integrating sphere mirror

When you measure a reflectance in an integrating sphere (such as our UV-Vis-NIR Shimadzu setup), you may sometimes use a mirror as the specular reflectance standard. This mirror has a nonuniform and nonunity reflectance, so you will want to correct for this. If you use the barium sulfate (or other diffuse white scattering reference), the reflectance is likely flat and 99% across the spectrum. There is a correction factor, which is simply the reflectance of the mirror, that you will **multiply** by the measured reflectance. The reason for this can be shown by thinking carefully about *how* the measured reflectance ($R_{measured}$) and true reflectance (R_{sample}) are calculated:

$$R_{sample} = \frac{S_{sample}}{S_{baseline}/R_{mirror}} = \frac{S_{sample}}{S_{baseline}} \cdot R_{mirror} = R_{measured} \cdot R_{mirror}, \tag{C.1}$$

where S_{sample} and $S_{baseline}$ are the signals measured by the Shimadzu during the reflectance measurement. Incidentally, the measured transmittance on an integrating sphere will be correct **as is** because both the denominator and numerator are multiplied by R_{mirror}:

$$T_{sample} = \frac{(S_{baseline} - S_{sample})R_{mirror}}{S_{baseline}\, R_{mirror}} = T_{measured}, \tag{C.2}$$

where similar naming conventions are used. The curve R_{mirror} was extracted in exactly the same way as above, except we measured the reference standard mirror against a better, calibrated Ocean Optics mirror with a known reflectance. Also, note that although the

Shimadzu actually performs a two-beam measurement, the arithmetic involved is essentially the same.

C.2 How to Fix the Glovebox

A regeneration of a brand new catalyst should bring O_2 levels down to 0.0 ppm. If they come down but then come up within a day or so, then you probably have a pretty serious leak. In that case, pressurize to 14ppm, open the valves on top of the catalyst (to bring every element of the GB to positive pressure), and try searching with the He sniffer. Last time I did this, the He signal was 10^{-1} directly on the leak (I could hear it hissing), and 10^{-2} within a couple inches of it. I imagine anything $> 10^{-4}$ is a significant enough leak to cause trouble.

C.3 How to fix the monochromator

Open the NI Measurement & Automation Explorer, scan for instruments under the GPIB tab, and write down the GPIB address for the unidentified instrument. Set the new GPIB address in both of the following Labview files:

- Program Files:National Instruments:LabVIEW 7.0:Instruments:270m:ISA_USER:Start Up.vi $\rightarrow$ ISA Util (488)
- ISA Spectrometer Setup V1.1